U.PORTO
FEUP FACULDADE DE ENGENHARIA
UNIVERSIDADE DO PORTO

Simulation of cold rolling process of steel profiles for shelter applications

Ângela Sofia da Silva Martins

Dissertation submitted to

Faculdade de Engenharia da Universidade do Porto

for the degree of

Mestre em Engenharia Mecânica

Supervisors:

Prof. Abílio de Jesus

Prof. Abel Santos

Prof. António A. Fernandes

Departamento de Engenharia Mecânica
Faculdade de Engenharia da Universidade do Porto

Porto, 2018

The work presented in this dissertation was performed at the
Department of Mechanical Engineering
Faculty of Engineering
University of Porto
Porto, Portugal.

Ângela Sofia da Silva Martins

E-mail: up201303013 @fe.up.pt

Faculdade de Engenharia da Universidade do Porto

Departamento de Engenharia Mecânica

Rua Dr. Roberto Frias s/n

4200-465 Porto

Portugal

Abstract

Cold roll forming is a complex sheet metal bending process used for mass production. Racking systems used today in logistic industries are normally made of thin-walled cold formed steel members. Cold roll forming processes introduce residual stresses in steel components and when combined with service loading stresses (e.g. due to the passage of shuttles in racking systems). These stresses may change the resulting stress range or average, affecting fatigue life of these components. Due to the lack of fatigue design rules at a European level for cold rolled formed steel members, this dissertation aims at analysing the stresses induced by roll forming and the influence of external cyclic loads on fatigue life of these profiles.

A parametric study of a U-channel profile with nine simulations was conducted to determine and analyse the influence of several parameters on the final shape of cold rolled formed steel profiles, which includes developing/designing the model simulation (specification of machine parameters, rolls design, flower patter, mesh definition, etc.) and extracting and analysing data and results obtained from COPRA® FEA RF finite element software. More importantly, an evaluation of residual stresses distribution across the thickness and along the surface of the strip width was performed. Afterwards, a local stress-based approach was used to estimate fatigue life of these components when subjected to cyclic loading. The stress range calculated incorporated the stresses after the roll forming process and the stresses induced by external loading. A similar fatigue analysis was conducted for a Z-section (rail section) profile, used in racking systems. Furthermore, a roll forming numerical simulation was also performed for this last profile, in order to analyse the three-dimensional effects of this manufacturing process.

Numerical results of this study show that residual stresses across the thickness displayed some differences in stress distribution from the theoretical solution of press-braked profiles, due to the existence of three-dimensional effects that cannot be neglected (the bending occurs gradually, which can lead to defects such as edge waviness, bow and twist, depending on the design of the process and rolls). Regarding fatigue analysis of these components, results of the present dissertation reveal that bending regions represent the critical areas where fatigue cracks tend to nucleate. Moreover, results show that an isotropic hardening rule might not be adequate to simulate roll forming profiles subjected to cyclic loading, since the Bauschinger effect is not reproduced. Instead, a kinematic hardening rule is more suitable.

Keywords: Thin-walled cold formed steel profiles, Cold roll forming, Bending, Residual stresses, Three-dimensional defects, Fatigue analysis, External mechanical cyclic loads, Rail profiles.

Resumo

Perfilagem a frio é um processo complexo de conformação plástica de chapas usado para produção em massa. Os armazéns automáticos frequentemente usados na indústria logística são usualmente constituídos por estruturas de espessura fina e conformadas a frio por perfilagem. Este processo de fabrico introduz tensões residuais nos perfis que, quando combinadas com as tensões de serviço, devido à passagem dos carris nos armazéns, podem conduzir a alterações nas amplitudes das tensões, influenciando a vida à fadiga dos componentes. Ao nível Europeu existe uma falta de normas relativas ao projeto à fadiga destas estruturas. Desta forma, a presente dissertação tem como intuito a análise da influência das tensões residuais introduzidas por perfilagem e pela aplicação de cargas cíclicas externas na vida à fadiga destes perfis.

Inicialmente, foi realizado um estudo paramétrico constituído por nove simulações de um perfil em U, de forma a analisar a influência de vários parâmetros na geometria final do perfil conformado. A fase inicial do estudo envolve o desenvolvimento do modelo das simulações (estabelecimento dos parâmetros das máquinas, design dos rolos, *flower*, geração da malha, etc.), assim como a extração e análise dos resultados adquiridos através do COPRA® FEA RF. Especial atenção foi dada às tensões residuais através da espessura e ao longo da largura da chapa. Seguidamente, foi usada uma abordagem que tem por base tensões locais, para estimar o número de ciclos de fadiga até à rutura da estrutura (devido à aplicação de cargas externas cíclicas). A amplitude das tensões geradas incorpora quer as tensões provenientes da perfilagem, quer as tensões geradas devido às cargas externas. Para o perfil em Z (usado nos armazéns de logística) foi realizada uma análise similar à executada para o perfil em U. Finalmente, foi concretizada uma simulação numérica do processo de perfilagem para o perfil em Z de forma a serem avaliados defeitos tridimensionais.

Os resultados numéricos revelam que as tensões residuais através da espessura apresentam uma distribuição semelhante à distribuição teórica de tensões para o *press-braking* (quinagem), embora alguns desvios são visíveis devido aos efeitos tridimensionais da perfilagem. No que diz respeito à análise à fadiga, conclui-se que os raios do perfil constituem as zonas críticas, onde se podem formar fendas de fadiga. Por fim, os resultados revelam que deveria ser usado um modelo de endurecimento cinemático em vez de isotrópico, devido à existência do efeito de Bauschinger aquando da aplicação de cargas cíclicas.

Palavras-Chave: Perfis de espessura fina conformados a frio, Perfilagem a frio, Flexão, Tensões residuais, Defeitos tridimensionais, Análise à fadiga, Cargas cíclicas externas, *Rail profiles*.

To my friends and family…

“What is not started will never get finished”

Johann Wolfgang von Goethe

Acknowledgements

I would like to express my gratitude to Professor Abílio de Jesus, Professor Abel Santos and Professor Augusto Fernandes for the opportunity to be a part of this project. I would like to emphasize my gratitude to Professor Abílio de Jesus for the knowledge and availability to discuss the directions of this dissertation as well as to clarify every doubts emerged during this semester. I am truly grateful for his constant readiness and encouragement both throughout this dissertation and my academic journey.

I wish to express a deep gratitude to the incredible colleagues at data M, Miguel Pereira and Pedro Ferreira for their endless patience demonstrated throughout the entire semester. Every doubt or question about the software, roll design, flower pattern, roll forming process among many others was answered with extreme attention. I also would like to acknowledge Sara Miranda for her availability to clarify some doubts about the software.

To all my friends and colleagues at Design Studio, namely Pedro Campos, Vitor Godinho, Cecília Peixoto and Carla Monteiro, for all the tips and clarifications and also for all the support provided in times of struggle.

A special thank you to my boyfriend, João Marafona, for his unlimited support throughout my time at FEUP. I am grateful for his patience, for his comfort words in times of need and for his encouragement.

Last and most importantly, I would like to express my deep gratitude to my parents and sister for their support and their sacrifice in order to provide me an academic education. Their invaluable care and teachings made all of this possible.

The European Commission, through the Research Fund for Coal & Steel is acknowledged and in particular the project FASTCOLD (grant number 745982), that funded a research fellowship.

Finally, the development of the present work would not have been possible without data M for providing the software used in this dissertation.

Contents

List of Figures

Appendix 1

Appendix 8

Appendix 9

Appendix 10

List of Tables

Appendix 7

Appendix 11

Nomenclature

a	Constant that determines the maximum value of the applied load
A_0	Initial area of a specimen´s cross section
b	Fatigue strength exponent
c	Fatigue ductility exponent
C_f	Constant that provides a relationship between stress range and life cycles
da/dN	Fatigue crack growth rate
E	Young´s modulus
F	Applied load
$F(t)$	Cyclic load
F_{SR}	Effective stress range
K	Strength coefficient
K'	Strain hardening coefficient
l	Current length of the specimen´s gauge
l_0	Initial length of the specimen´s gauge
m	Slope of fatigue strength curve
n	Strain hardening exponent
n'	Strain hardening exponent
N	Number of full stress cycles
N_c	Number of cycles until failure
N_f	Number of reversals to failure
N_R	Number of cycles until failure related to a constant stress range

R	Ratio between minimum and maximum stress
R_ε	Strain ratio
s	Approximate standard deviation of fatigue data
S_m	Mean stress
$\Delta\varepsilon$	Total strain range
$\Delta\varepsilon^E$	Elastic strain range
$\Delta\varepsilon^P$	Plastic strain range
$\Delta\sigma$	Stress amplitude or range
$\Delta\sigma_C$	Reference value of the fatigue strength at N_c= 2 million cycles
$\Delta\sigma_R^m$	Amplitude of nominal stress ranges
ε_0	Material parameters for Swift's hardening law
ε_e	Elastic strain
ε_{eng}	Engineering strain
ε_f'	Fatigue ductility coefficient
ε_i	Strain at a given point of the stress-strain curve
ε_{true}	True strain
ε_p	Plastic strain
ε_t	Total strain
θ	Fold angle of the theoretical flow of material
μ	Friction coefficient
σ	True stress
σ_a	Stress amplitude
σ_{eng}	Engineering stress;
σ_f'	Fatigue strength coefficient
σ_i	Stress at a given point of the stress-strain curve
σ_m	Mean stress
σ_{max}	Maximum stress
σ_{min}	Minimum stress
σ_r	Stress range

σ_{true}	True stress
σ_{Y0}^{C}	Compressive yield stress
σ_{Y0}^{T}	Tensile yield stress

Acronyms

CPU	Central Processing Unit
ERW	Electric Resistance Welded
FE	Finite Element
FEA	Finite Element Analysis
FEM	Finite Element Method
HSS	High Strength Steels
R&D	Research and Development
R&S	Racking and Shelving Systems
S/R	Storage / Retrieval
S-N	Stress amplitude vs number of cycles to fatigue failure
ε – N	Strain amplitude vs number of cycles to fatigue failure

Chapter 1

Introduction

1.1. Background

Cold roll forming is a continuous process aiming a progressive bending of metals using stations with rotating rolls without changing material thickness. Rolling at room temperature took its first steps in the fourteenth century for gold and silver applications. The first record of the existence of rolling mills was in 1480, designed by Leonardo da Vinci. The late eighteenth century marked the beginning of cold rolling of steel, nonetheless this process became widely used in the nineteenth century. In the late nineteenth century and in the twentieth century, a massive variety of metals, such as aluminium, copper, titanium and specially alloys were being cold formed and made commercially available (Halmos 2013).

In the early stages of this process, much of the attention was not paid to the behaviour of the material during the design process and typically, the design of the rolls and the process were based on the experience of the designers. Since the early part of the twentieth century, cold roll forming had become an established industrial process (Senanayake, Cole, and Thiruvarudchelvan 1994). After the Second World War, roll forming represented a significant percentage of the fabrication of sheet metal products, replacing press braking and other forming processes (Halmos 2013).

Roll forming was effectively implemented in the sheet metal industry for the manufacturing of products for roofing, siding, farm buildings, silos, shelving, storage racks, electrical products, power plants, doors, windows, furniture, airplanes, spacecraft, and many more. In the 1950s and 1960s, other operations were being incorporated into the roll forming lines, such as the applications of pneumatic presses, in-line welding and the use of prepunching and prepainting metals. In the late 1970s and early 1980s, computer-aided roll design systems were introduced and in the 1990s programmable controllers and computers were being used to control the lines (Halmos 2013).

Over the years, material tolerances have become tighter and the demand for higher flexibility increased. Competitiveness forced the reduction of the number of operators and led to an increase of product quality and production rate at the lowest possible cost (Halmos 2013). These challenges can be overcame or eliminated by enhancing product design, improving materials, using better and more efficient equipment, improving tooling and using better educated and motivated work force (Future Market Insights 2014).

There are several CAD programs suitable for the design of roll formed processes, including the forming rolls, the roll pass sequences and the flower design. Nonetheless, numerical techniques represent an advance in technology since it allows a reduction of the lead time necessary to design the process so that the new product can be introduced in the competitive market sooner. There are, nowadays, many commercially available FEM packages to simulate the roll forming process. Finite element analysis can be used to predict and avoid defects as well as to reduce strains (Heislitz et al. 1996).

An important application of cold roll forming products is in racking and shelving (R&S) systems for the logistic industry. The racking systems installed in warehouses are almost exclusively made of thin-walled cold-formed sections, due to the possibility of manufacturing tailor-made sections, reducing material consumption and, at the same time to produce light-weight and high quality profiles. The logistic industry has been suffering major evolutions, due to the high demand for individual logistic concepts to create adapted storage equipment for a particular client. Also, new warehouse management systems have been created along with the development of storage and retrieval systems, such as "Storage / Retrieval (S/R) Machines". Additionally, the recent trend in the logistic industry is the adoption of storage systems with multi-level cranes (Figure 1), meaning that the rack structure has to support the S/R machines as well (FASTCOLD project internal documents).

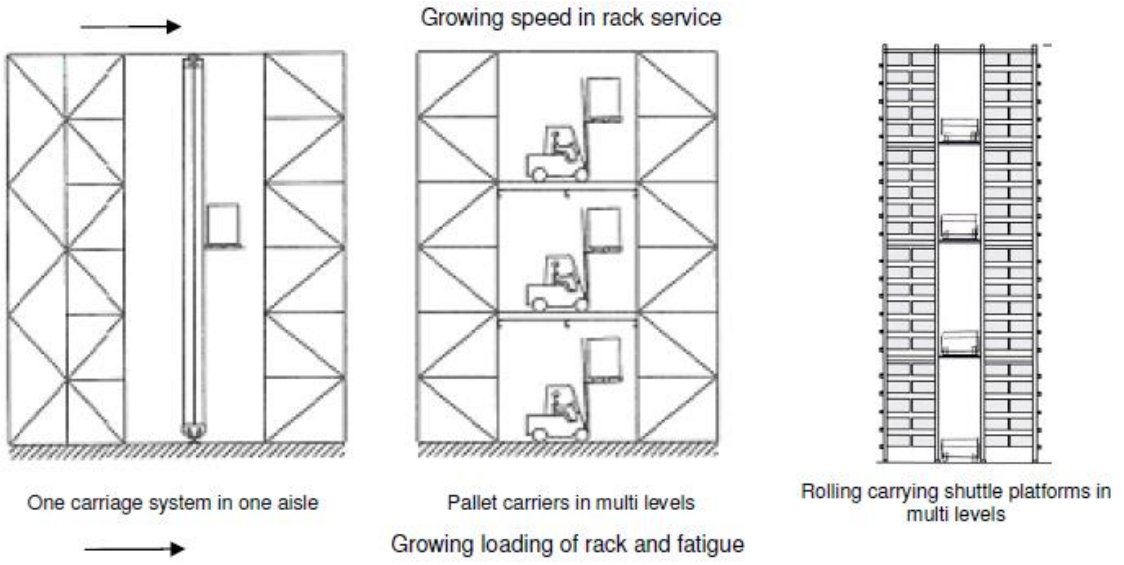

Figure 1 – Modern trend in storage system design.

An important part of the European economy relays on the logistic industry that includes warehousing, transshipment and transport. In 2011, the annual turnover for intra-logistic systems was estimated to a total of € 2759 million to € 3250 million. The market of the involved European steel and racking industry can be specified to approximately € 300 - € 400 million per year. However, this industry has a problem with fatigue and crack propagation in steel rack structures. The reported economical loss due to these problems is approximately € 15 Million – € 20 Million. On one hand, this fatigue failure of the product results from the cyclic loading applied to the racking and shelving systems due to the new Storage and Retrieval (S/R) machines which are capable of higher speed and accelerations, resulting in higher dynamic actions. On the other hand, residual stresses from the roll forming manufacturing process also play an important role in fatigue failure of the product. Usually, roll-formed members present higher residual stresses than

those produced by press-braking. Bending residual stresses are much higher at the corners of the cross section (FASTCOLD project internal documents). The influence of residual stresses of cold rolled profiles on their fatigue behaviour is a hot topic not properly investigated or covered by existing design rules.

1.2. European project FASTCOLD (FAtigue STrength of COLD-formed structural steel details)

The racking systems that exist today in the industry are normally made of thin-walled cold formed sections. Since the logistic industry adopted the storage systems with multi-level cranes, the effects of cyclic loading cannot be neglected anymore. FASTCOLD project purpose is to develop fatigue design rules for cold form steel members. Design rules already exist for hot-rolled steel details in EN 1993-1-9. However for cold formed steel sections they are missing on a European level (EN1993-1-9: Design of steel structures - Part 1-9: Fatigue does not present fatigue design rules or classification of cold-formed thin-walled details) (EN 1993-1-9 2005).

To summarize, FASTCOLD project aims to provide scientific knowledge and practical design of steel rack structures by introducing the knowledge of fatigue behaviour of cold formed structural steel details and the fatigue design concepts for these racking systems. The details and steel components considered in the European project are both of general use in steel structures and specific for racking and shelving systems applications. These racking systems are present in logistic warehouses (cold formed steel members under cyclic loading are widely used in these industrial applications). For this reason, FASTCOLD can provide support and guarantee a competitive market for the European logistic and racking industry mainly due to the cost-effective designs and the ability to ensure safe and durable racking systems and components, avoiding fatigue crack propagation and its adjacent cost to repair the structures (FASTCOLD project internal documents).

1.3. Objectives of the dissertation

The main purpose of the present work is to study the influence of the roll forming process in fatigue resistance of cold formed profiles. In order to achieve this goal, several other objectives must be fulfilled:

- Understand the fundamental principles of cold roll forming as a manufacturing process, which means understanding the influence of geometrical and process parameters and material properties on residual stresses and on three-dimensional effects, through a parametric study of a U-channel profile;
- Evaluate the distribution and magnitude of residual stresses for both profiles (U-channel and Z-section), especially in corner regions, since these areas tend to present the highest values of residual stresses;
- Identify the critical areas (as far as residual stresses are concerned), as well as evaluate the development of three-dimensional defects and springback for investigated profiles (U-channel and Z-Section);
- Implement mechanical cyclic loads in the simulation models (U-channel and Z-Section) in order to study the influence of existing residual stresses (due to the roll forming process) combined with cyclic load on the fatigue resistance of the profiles.

To achieve these goals, several numerical simulations were performed. In the early stages of a project, a numerical analysis brings numerous advantages, since it allows a safe simulation of potential failures of the structure, without investing in experimental procedures. For instance, an experimental parametric study would be an impossible investment in terms of cost and time requirements. However, numerical simulations allow a visual representation of a wide variety of physical parameters at a relatively low investment and rapid calculation time.

1.4. Planning and methodology

Faculdade de Engenharia da Universidade do Porto (FEUP) as a partner of FASTCOLD project is responsible for the numerical analysis of local stresses induced by cold-forming. This dissertation, integrated in a research fellowship, aims to contribute to FASTCOLD project by performing numerical work on simulation of the roll forming process of steel profiles that will be investigated in the project (Z-section profile). A number of parameters, such as the number of stations, the radius-thickness ratio, the material properties, the number of elements through the thickness of the profile, the friction coefficient and the distance between stations will be studied in order to understand their influence in three-dimensional effects and residual stresses and consequently in fatigue resistance. The numerical analysis of cold-formed steel profiles was performed using available commercial finite element software, provided by data M, specifically COPRA® FEA RF.

The research plan was divided in six tasks:

- Task 1: State of art review;
- Task 2: Selection of sections and materials within FASTCOLD project;
- Task 3: Software learning;
- Task 4: Numerical simulation including parametric studies;
- Task 5: Fatigue strength considerations and implementations in COPRA® FEA RF;
- Task 6: Reports (FASTCOLD reports contributions, MSc dissertation writing and presentations preparations).

This dissertation and the scientific investigation were conducted at FEUP - Mechanical Engineering Department. The timeline for this research fellowship is presented in Table 1.

Table 1 – Timeline for completion of tasks.

	February	**March**	**April**	**May**	**June**
Task 1					
Task 2					
Task 3					
Task 4					
Task 5					
Task 6					

1.5. Layout of the dissertation

This dissertation is divided into 5 chapters. The order in which this document is organized does not necessarily reflect the real order of events.

Chapter 2 – Literature review is dedicated to the presentation of concepts. This chapter provides an introduction to the roll forming process, including typical three-dimensional defects as well as the presence of residual stresses and strains in the final product, the cold rolled profiles. Furthermore, it presents basic rules for fatigue design of steel members. Finally, a clarification of the importance of numerical simulation is provided, particularly in cold roll forming and a description of the software used in the numerical analysis and simulations is presented.

Chapter 3 – Numerical simulation of a U-channel profile provides a parametric study in order to determine the influence of different parameters in cold roll forming processes. Moreover, a study of the influence of process residual stresses combined with external mechanical cyclic loads is presented, in order to estimate the number of cycles before failure of the component by fatigue.

Chapter 4 – Numerical simulation of a Z-Section profile analyses the influence of the cold roll forming process on the material, such as the formation of defects, stresses and strains. Also, this chapter gives a description of the experimental work performed to determine the stress-strain curve of the material. Finally and similarly to Chapter 3, a study of the influence of a fatigue loads in life predictions is also presented.

Chapter 5 – Conclusion is divided in two parts. Firstly, relevant and important conclusions of this investigation are exhibited. Secondly, this chapter proposes future recommendations to improve or to complete the work developed so far.

Chapter 2

Literature Review

This chapter analyses the available literature with regard to roll forming processes and fatigue analysis of cold formed steels and is divided into three main sub sections as follows:

- The roll forming process. An introduction to the roll forming process is presented in order to facilitate the understanding of the effects of manufacturing process parameters on the material, including deformation modes, defects and residual stresses;
- Fatigue analysis of the cold formed profiles to study the behaviour of profiles when subjected to cyclic loads;
- Finite element method analysis aiming the understanding of the advantages of numerical simulations as well as the clarification of software capabilities used in this investigation.

2.1. The roll forming process

Metal forming can be divided in three main categories, depending on the working temperature (Güner 2007):

- Cold forming, in which the forming occurs below the recrystallization temperature. Normally for steels, this process takes place at room temperature;
- Warm forming, in which the forming occurs near the recrystallization temperature;
- Hot forming, in which the forming occurs above the recrystallization temperature.

Cold forming brings various advantages such as high strength of the final product, better dimensional precision and surface finish as well as less waste of material. However, it needs high forming loads and the ductility and formability of the material at low temperatures is limited (Güner 2007).

Cold roll forming is a process where an undeformed strip is gradually bent in several forming steps in order to produce the final profile (Figure 2) (Lindgren 2007b). The required shape needs to be formed with the least amount of "incremental steps". Fewer steps will distort the product, since the stresses generated in the metal reach an unacceptable level, but too many steps will make the tooling and the process too expensive (Figure 3) (Halmos 2013).

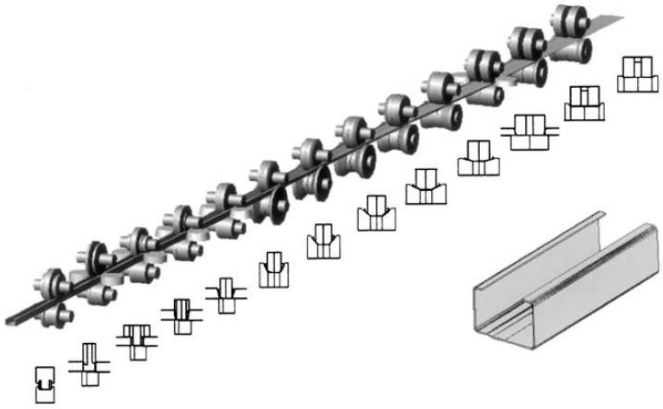

Figure 2 – Strip gradually formed into the finished section (Halmos 2013).

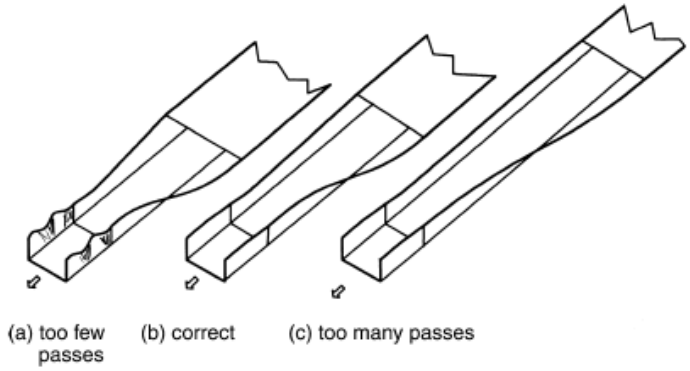

Figure 3 – Influence of the number of incremental steps in roll formed section (Halmos 2013).

This process brings a variety of advantages to the sheet metal industry, such as (Güner 2007):

- High speed of production of profiles;
- High strength/weight ratios than with hot roll formed profiles;
- Surface finish of the material without damage;
- Possibility to combine with other auxiliary operations such as piercing, notching, welding and perforation.

If a material can be bent, it can be roll formed. Moreover, the material can be pre-painted or pre-coated before being submitted to this process. The thickness of the material depends on the size of the available machinery (some literature suggests thickness between 0.1 and 19 mm). The product length is also limited by the facilities in which the process takes place (Güner 2007). The speed of production can vary between 15 m/min and 185 m/min. Speed of production depends on the tolerance of the cross-section, the material and the speed of the machine when feeding the raw material, among others factors (Lindgren 2009).

2.1.1. Behaviour of metal strip during roll forming – deformation modes

Metal strips experience various types of deformations during roll forming processes, such as:

- Transversal bending: This type of deformation is indispensable to transform metal strips into products with the required cross-sections. The final cross-section is achieved gradually (Figure 4) by using a series of contoured rolls.

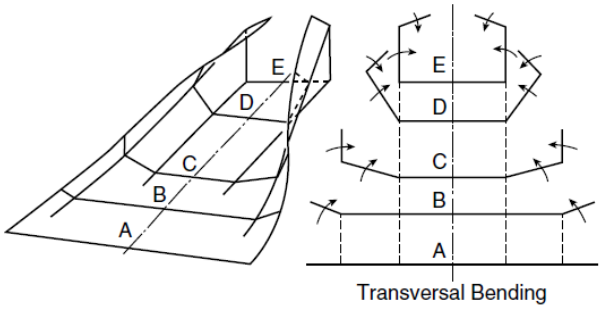

Figure 4 –Transversal bending of metal strip during roll forming (Halmos 2013).

- Redundant deformations: Metal strips enter the roll forming mills either in precut or coil form and the contoured rolls deform the strips gradually in order to produce the final product with the required cross-section. This process is responsible for additive redundant deformations (Figure 5), such as longitudinal bending and bending back, longitudinal elongation and/or shrinkage, transversal elongation and/or shrinkage, shear in the metal's plane, shear in the direction of the metal's thickness and various combinations of the deformations described above (Halmos 2013).

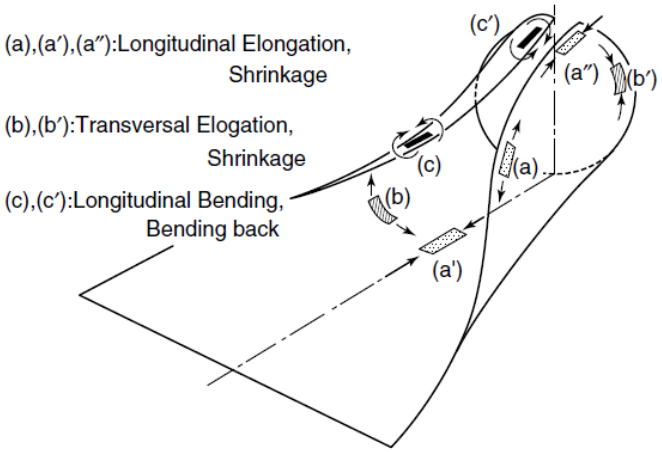

Figure 5 – Additive redundant deformations of metal strip during roll forming (Halmos 2013).

2.1.2. Longitudinal edge strain

One of the main deformations types in roll forming are the longitudinal stretching and bending, which are responsible for most manufacturing defects such as longitudinal bow, twist, edge wave and partially springback.

Figure 6 is a schematic representation of the theoretical flow of material when a strip is formed into an angle, θ. While the bending line travels along a straight line (from A to B), the edge travels along a helical path (from C to D) (Abeyrathna 2014).

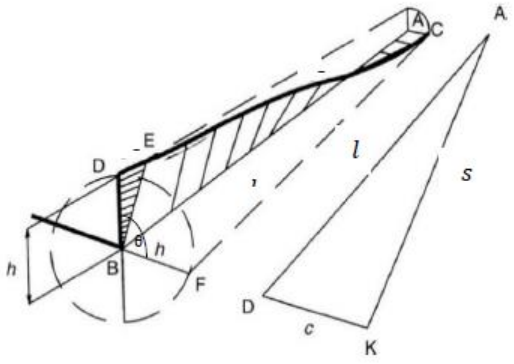

Figure 6 – Schematic representation of the movement of the edge when roll forming a flat strip (Halmos 2013).

The highest edge strain normally appears at the flange edge when it passes the rollers, within the deformation length (Figure 7). The deformation length is an important parameter to take into account when determining the peak longitudinal strain as well as the minimum distance between stations (Abeyrathna 2014).

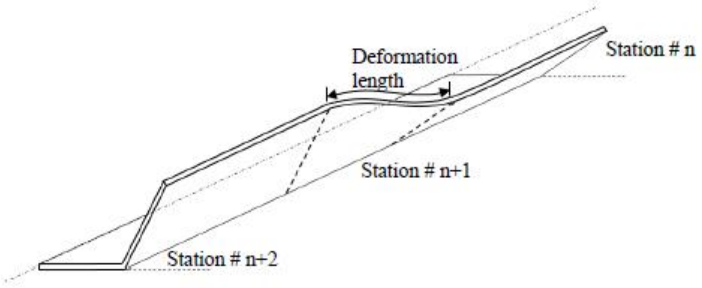

Figure 7 – Flange edge longitudinal deformation and deformation length (Abeyrathna 2014).

One of the main goals of process designers is to maintain the peak longitudinal edge strain under the elastic limit of the material (in order to reduce geometrical defects and residual stresses). Material properties, geometric parameters and process/machine parameters are three factors that have influence on peak longitudinal edge strain. Some studies (Han et al. 2005, 2001) show an increase in peak longitudinal strain when increasing the yield strength of the material while others Lindgren (2007a, 2007b) conclude the opposite trend. With regard to geometric parameters, material thickness, forming angle, width of the web and flange length are the most important parameters that have an effect on peak longitudinal edge strains. Furthermore, increasing the

forming angle leads to more stress introduced at the flange edge, leading to an increase in peak longitudinal edge strain for higher bending angles (Abeyrathna 2014). Some studies reveal the influence of forming angle on peak longitudinal edge strain for three different materials, DP600, DP1000 and MS900 (MS900 has the highest yield strength of all three materials while DP600 has the lowest) and two different thickness and conclude the same trend (Figure 8) (Abeyrathna, Rolfe, and Weiss 2017).

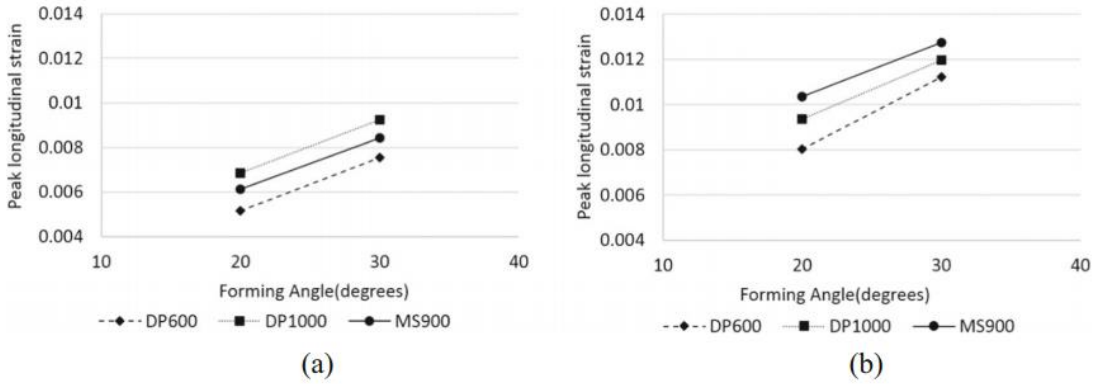

Figure 8 – Influence of forming angle on peak longitudinal edge strain for (a) 1.5 mm and (b) 2 mm of thickness (Abeyrathna, Rolfe, and Weiss 2017).

Additionally, peak longitudinal strain decreases when the distance between stations increases, because higher distance between stations allows a more progressive deformation. However, Abeyrathna, Rolfe, and Weiss (2017) investigation revealed no obvious effect of station distance on peak longitudinal strain for either material thickness (Figure 9).

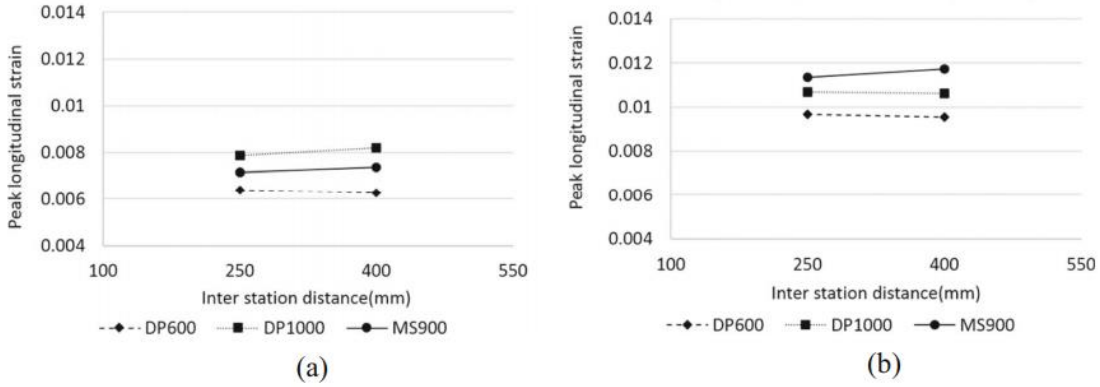

Figure 9 – Influence of inter station distance on peak longitudinal edge strain for (a) 1.5 mm and (b) 2 mm of thickness (Abeyrathna, Rolfe, and Weiss 2017).

Lindgren (2007b) studied the change in the longitudinal peak membrane strain at the flange edge and the deformation length of a U-channel profile while increasing the yield strength of the material. The number of forming steps and the distance between them are influenced by this parameter. The number of steps is directly related with the cost of the process and, in order to reduce the number of steps, the shape of the cross section, tolerance, thickness and the material properties must be considered. Lindgren (2007a) showed that the total strain (plastic and elastic)

decreases when the virgin yield strength increases and for materials with higher virgin yield strength the strains become purely elastic. In addition, the longitudinal peak membrane strain decreases, the deformation length increases, when the material has higher yield strength. Increasing longitudinal membrane strain induces residual stresses in the flange of the profile, which can cause several problems, such as wavy edges, longitudinal curvature, end flare, among others. Materials with higher yield strength offer the possibility of using fewer forming steps. Nonetheless, high strength steels (HSS) exhibit larger springback.

2.1.3. Product defects in roll forming

Redundant deformations, in spite of influencing the transversal bending of the strip that is required to form the desirable cross-section of the product, also cause a variety of defects in products. These deformations affect stresses and strains induced in the metal strip as well as springback deformations after forming and the distribution of residual stresses (Halmos 2013). Some of the product defects caused by redundant deformations are described in the following paragraphs.

- **Longitudinal bow and twist**

Longitudinal bow and twist are caused by nonuniform transversal distribution of the longitudinal membrane strain and are the most common defects in narrow roll formed products (Figure 10). The longitudinal bow and twist can be reduced if an appropriate number of passes are being used. When the number of passes is too small, the transversal deformation in each pass is too high. Furthermore, the roll design and the roll positions also influence the longitudinal membrane strain because if the flow of each portion of the strip is not smooth, the magnitude and nonuniformity of longitudinal strains tend to increase. Finally, another measure to reduce the longitudinal membrane strain is to use entry guides and intermediate guides (Halmos 2013).

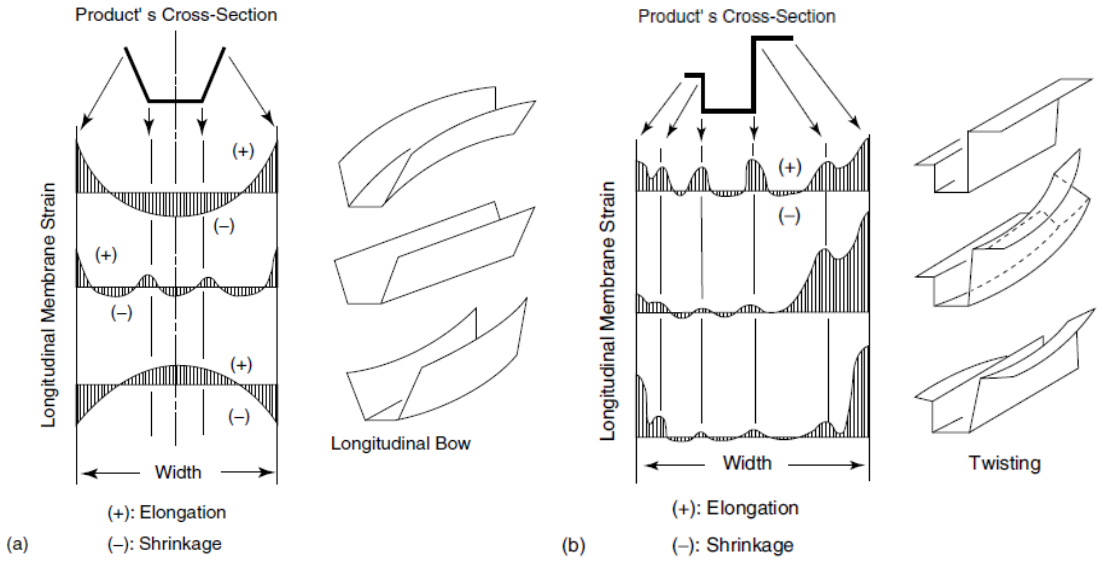

Figure 10 – Transversal distribution of longitudinal membrane strain; (a) longitudinal bow; (b) longitudinal twist (Halmos 2013).

Abeyrathna, Rolfe, and Weiss (2017) also concluded that longitudinal bow increases with the forming angle for all materials that were studied in their research (Figure 11). Furthermore, longitudinal bow decreases when increasing inter-station distance for both thicknesses (Figure 12). Increasing distance between stations leads to a smoother bending progression, resulting in lower residual stresses through the cross section of the profile.

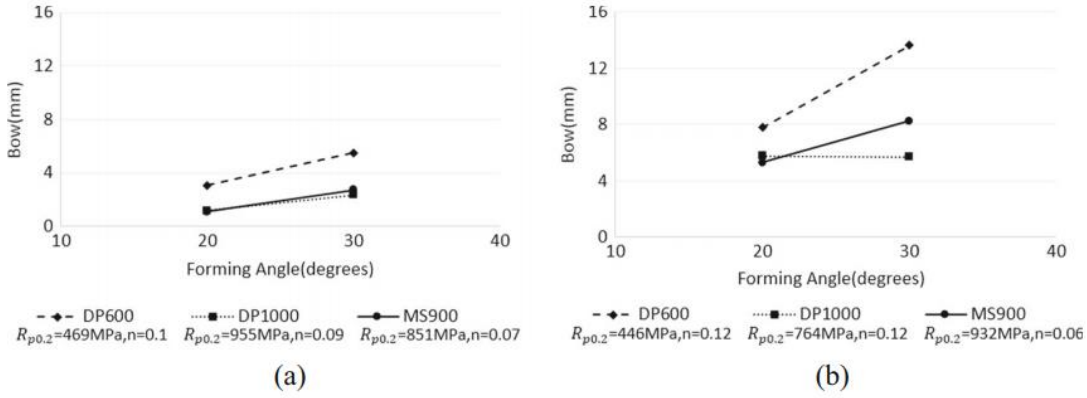

Figure 11 – Influence of forming angle on longitudinal bow for (a) 1.5 mm and (b) 2 mm of thicknesses (Abeyrathna, Rolfe, and Weiss 2017).

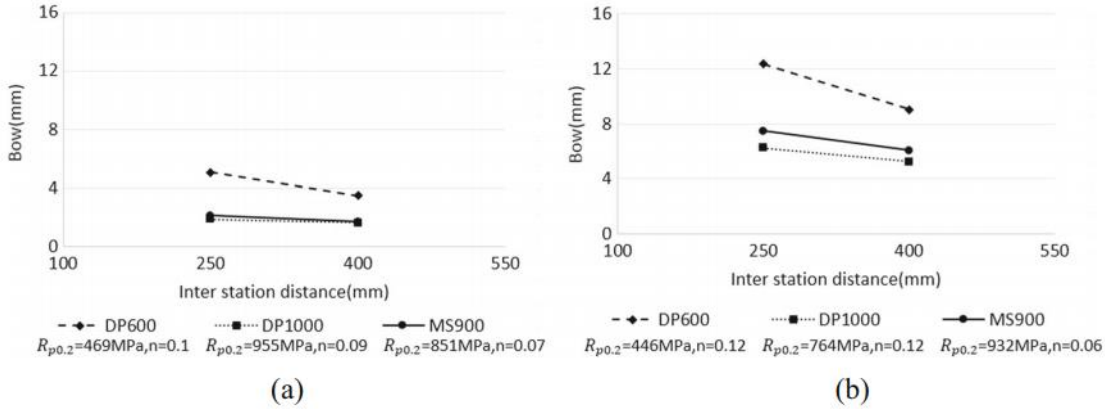

Figure 12 – Influence of inter station distance on longitudinal bow for (a) 1.5 mm and (b) 2 mm of thicknesses (Abeyrathna, Rolfe, and Weiss 2017).

- **Edge wave (waviness)**

Edge wave (Figure 13) is one of the most common defects that appears in finished products as well as in semiformed metal sheets moving from one pass to the next. This defect is caused by elastoplastic buckling. In the first stages of forming, the longitudinal elongation occurs in the edge portion of the strip (since the edge portion has to move both in the vertical and transversal directions). Elongation continues to take place when the edge portion enters the roll gap. Nonetheless, elongated edge portion must shrink again when it exits the roll gap in order to guarantee that each portion of the semiformed strip remains equal (so that the product stays straight). In some cases, when exiting the roll gap, the stress in the edge portion exceeds the

critical value, making it very difficult for the elongated edge portion to shrink smoothly, causing edge waviness (Halmos 2013).

In order to avoid this defect, the longitudinal elongation of the edge portion should be reduced below the critical value by using a sufficient number of rolls, suitable roll designs and positions and guides (Halmos 2013).

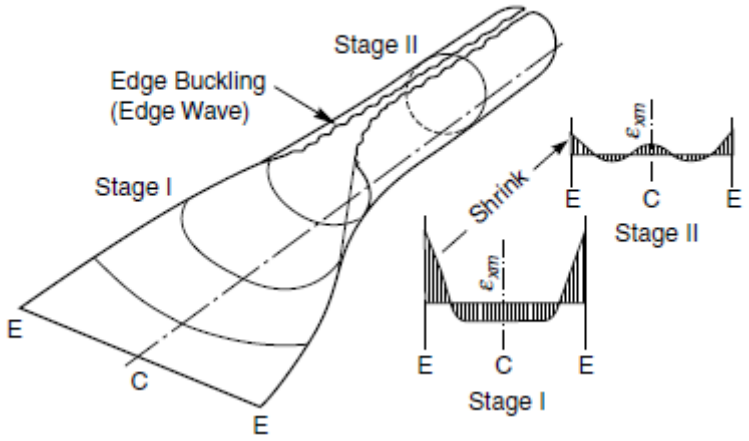

Figure 13 – Edge buckling or edge waviness taking place during roll forming of ERW pipes (Halmos 2013).

Moreover, as far as buckling (waviness) is concerned, during roll forming, the longitudinal fibres in the flange zone are stretched during deformation and the maximum stretching occurs at the flange edge. In order to maintain the longitudinal equilibrium, some parts of the strip are under compression. For a channel section, normally, the web and the bend zones are under compression (Tehrani et al. 2006). Bhattacharya and Smith (1984) experimental work showed that both tension in the flange and compression in the web and bend zones are beyond the yield strength of the material. These length variations of the longitudinal fibres depend on the fold angle, θ and lead to a product that can curve down (non-straight profile). When critical values of the fold angle are exceeded, local edge buckling may occur. Since the strip tend to curve down and it is common industrial practice for each roll station to be at the same horizontal level, the second station exerts a vertical force preventing the tendency of the strip to curve down. This force can cause the flange to be longitudinally compressed, which can originate local edge buckling (Tehrani et al. 2006). Summarizing, Tehrani et al. (2006) studied the potential occurrence of buckling as a result of deformation between two roll stations and showed that:

- ✓ The strain in the flange is tensile while the web strain is predominately compressive;
- ✓ Peak strain and residual strain increase as the fold angle increases.

- **End flare**

The roll formed product can acquire changes in the cross section geometry at the ends and they can be toward or away from the centreline of the section. Normally, on one hand, for profiles of lower strength materials with shallow sections and pre-cut strips, the front end is flared-in and the tail end is flared-out. On the other end, flare-out frequently occurs for deep sections or high

strength material. A roll formed profile that has been cut off usually exhibits these defects, (Figure 14) (Abvabi 2014).

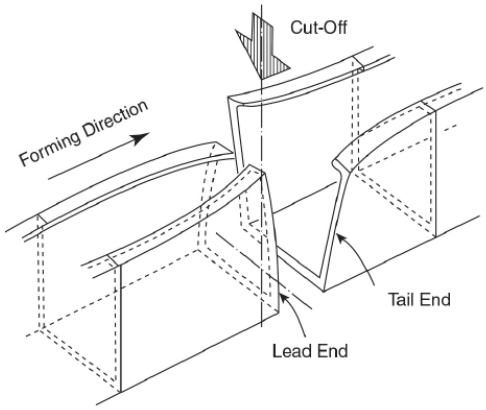

Figure 14 – Flare of cut-off ends (Halmos 2013).

Saffe, Takuo, and Hiroshi (2014) investigated the appearance of cut end deformation of a roll formed hat channel and concluded that the profile will flair in at front end and flair out at tail when cut off due to the residual shear stress in the longitudinal direction and residual twisting moments.

- **Springback**

Springback represents the elastic recovery of the material when the forming force is released from the strip leading to cross sectional deviation in the finished product. Springback is a common defect in roll forming processes (Figure 15) (Abeyrathna 2014).

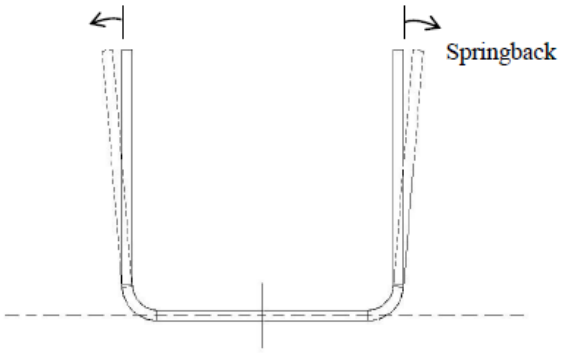

Figure 15 – Springback in a U-channel profile (Abeyrathna 2014).

In most available literature about springback, prevails studies about springback in die bending and folding. However, pure bending theory cannot be applied to roll forming process, since the last one is a progressive/continuous process. In roll forming, longitudinal stretching and compression have a strong impact in springback (Abeyrathna 2014). In other words, cold press braking and cold roll forming, in spite of being two bending operations, produce different deformation histories (Figure 16). The first process leads to a uniform deformation along the

length of the workpiece. In cold roll forming, the deformation is constantly changing as the material moves through the process (Panton, Duncan, and Zhu 1996).

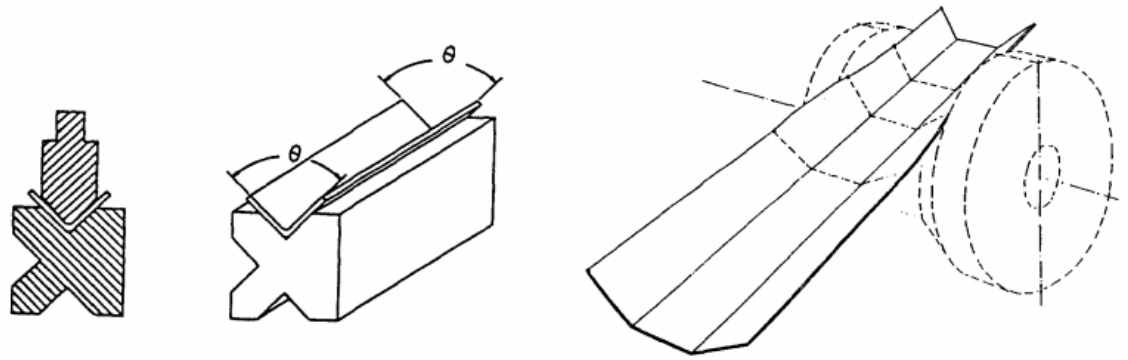

Figure 16 –Press braking (left); Cold roll forming (right) (Panton, Duncan, and Zhu 1996).

Groche, Beiter, and Henkelmann (2008) stated that bended part's geometry is affected by various parameters such as bending radius, sheet thickness, yield strength, Young's modulus and material's strain hardening coefficient. Also, springback is influenced by the design of the flower pattern.

Abeyrathna (2014) stated that increasing the yield strength and tensile strength of the material leads to higher springback (since the elastic limit of the material increases – Figure 17). Moreover, increasing bending radius/thickness ratio also leads to higher springback.

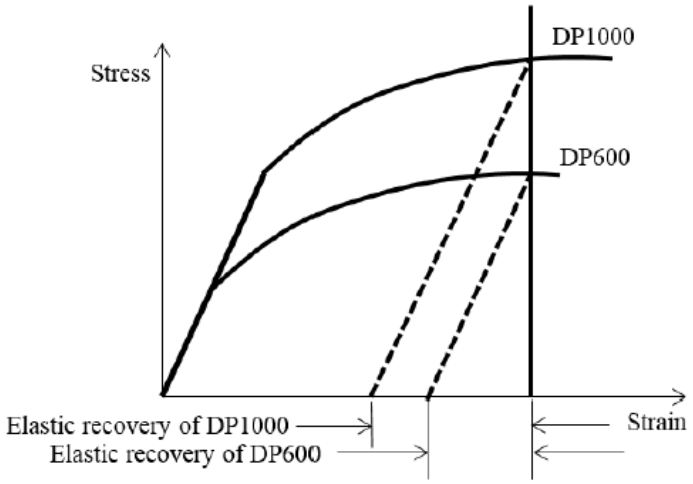

Figure 17 – Schematic relation between yield strength of material and material hardening on springback (Abeyrathna 2014).

2.1.4. Residual stresses in roll forming

The *Handbook of Residual Stresses and Deformation Steel* (Lohe, Lang, and Vohringer 2002) defines residual stresses as:

"…the stress that remains in mechanical parts that are not subjected to any outside stresses".

Residual stresses can be divided into three groups (Abvabi 2014):

- Macro residual stresses (type I): stresses on a scale larger than the grain size of the material;
- Micro residual stresses (type II): stresses that vary on the scale of an individual grain;
- Micro residual stresses (type III): stresses that exist within a grain.

All manufacturing processes introduce residual stresses into mechanical parts. External loads are not the only stresses responsible for the failure of a structure, since residual stresses influence fatigue behaviour, fracture strength and even corrosion resistance of mechanical parts. The new state of residual stresses introduced by manufacturing processes can have a positive effect on fatigue behaviour, for example increasing the fatigue limit in the case of surface compressive stress, or it can have a negative effect, for instance, decreasing the stress corrosion behaviour of a material in case of tensile residual stress (Lohe, Lang, and Vohringer 2002).

On one hand, profiles or components might fail during service due to the exceeding of allowable plastic deformation, crack initiation, unstable crack propagation or other instabilities such as buckling. On the other hand, residual stresses might be one of the most crucial parameters influencing service behaviour, especially for high strength material states (Lohe, Lang, and Vohringer 2002).

Residual stresses can be divided in two different parts: flexural and membrane (Figure 18). For cold formed profiles, residual stresses across the thickness are dominated by the flexural part. Membrane residual stresses are more prevalent in roll formed profiles than in press-braked. Theses membrane residual stresses exist essentially in corner regions. However, to counteract their effect, the yield stress is elevated in corner regions due to the significant cold work of forming (Schafer and Peköz 1998).

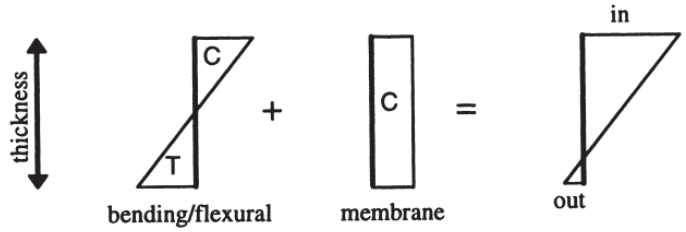

Figure 18 – Flexural and Membrane Residual Stresses (Schafer and Peköz 1998).

Cold roll forming processes originate residual stresses and strains across the sheet thickness, which influence the load-displacement response and ultimate strength of cold formed steel members. Figure 19 illustrates the nonlinear through the thickness residual stress distribution (in

the direction of bending) caused by the plastic bending followed by elastic springback (Moen, Igusa, and Schafer 2008).

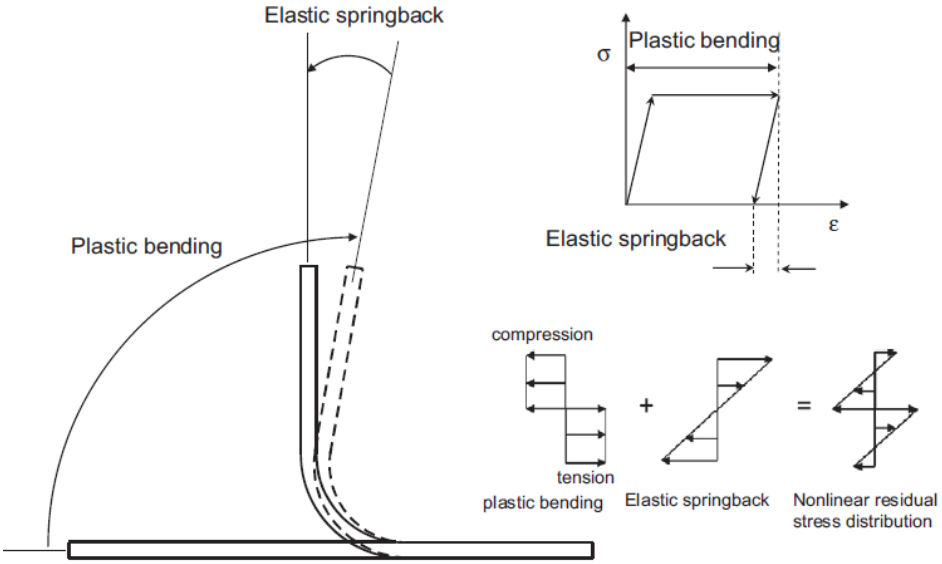

Figure 19 – Nonlinear through the thickness residual stress distribution of thin sheets (Moen, Igusa, and Schafer 2008)

Moen, Igusa, and Schafer (2008) provided a prediction method to determine the initial residual stresses and effective plastic strains in cold formed steel members. The authors assumed that two manufacturing processes contribute to through the thickness residual stresses: (i) sheet coiling, uncoiling and flattening and (ii) cross section roll forming. For the present dissertation, only the stresses induced by roll forming will be considered.

Moen, Igusa, and Schafer (2008) proposed a set of algebraic equations to predict the transverse and longitudinal residual stresses originated when roll forming a cross section (in this case, a U-channel profile). Residual stresses were only assumed to exist at the location of formed corners, between the roller die reactions (Figure 20).

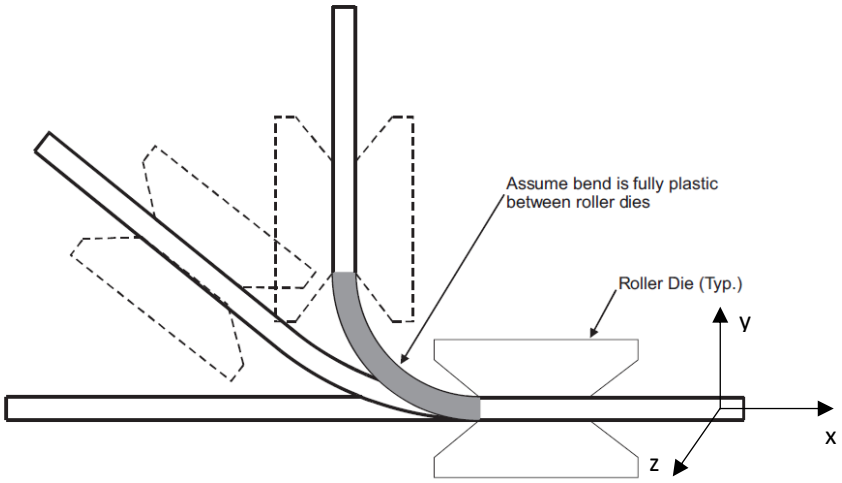

Figure 20 – Cold forming of a steel sheet (Moen, Igusa, and Schafer 2008).

During the roll forming process, the steel sheet yields through its thickness during the process, for small bend radii common in the cold forming industry. The sheet will reach the fully plastic stress state as the corner approaches its final radius (Figure 20). After the sheet becomes fully plastic across its thickness, the engineering strain continues to increase as the radius decreases. Afterwards, an elastic springback occurs, provided that the final bend radius is reached and the imposed radial displacement is removed. This elastic rebound promotes a change in through the thickness stress (Figure 21) (Moen, Igusa, and Schafer 2008).

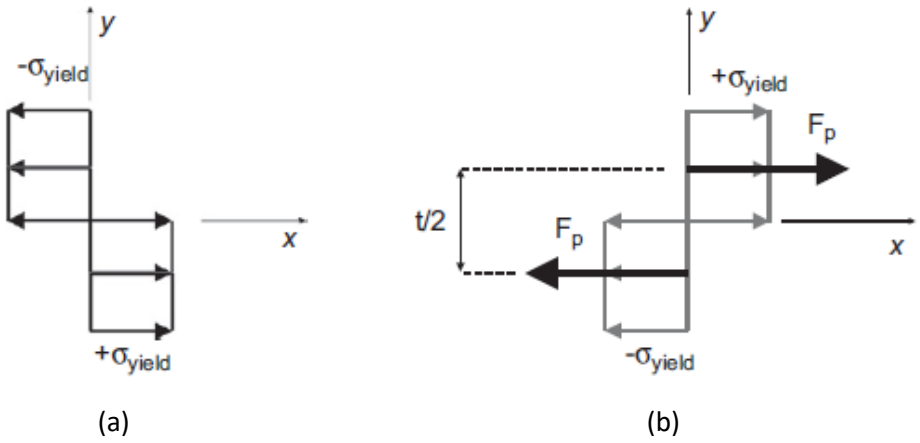

Figure 21 – (a) Fully plastic transverse stress state from cold-forming; (b) Force couple applied to simulate the elastic springback of the steel sheet after the imposed radial deformation is removed (Moen, Igusa, and Schafer 2008).

The final transverse stress state results in the sum of the fully plastic stress distribution through the thickness and the unloading stress from the elastic springback of the corner (Figure 22) (Moen, Igusa, and Schafer 2008).

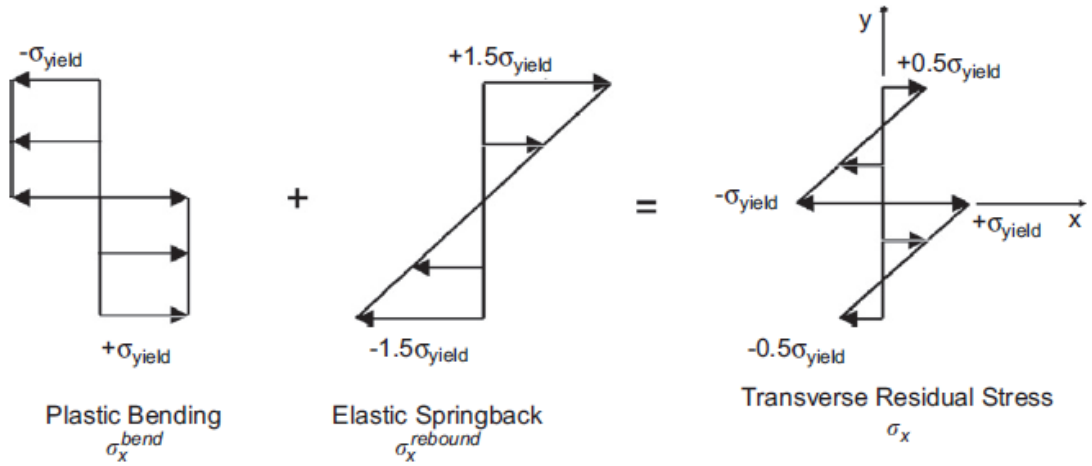

Figure 22 – Self-equilibrating transverse residual stress (Moen, Igusa, and Schafer 2008).

As shown, the stress is nonlinear through the thickness and is also self-equilibrating. Nonlinear distributions present in Figure 22 are typical for press braked profiles and for roll formed profiles some deviations from these distributions may occur due to three-dimensional effects.

As previously stated, residual stress field of a component may play an important role in fatigue crack nucleation. This influence of residual stresses is an imperative aspect in mechanical design and life assessment. Normally, a compressive residual stress field improves the fatigue life. With this purpose, many mechanical and heat treatments are conducted in components (De Giorgi 2011).

Typically, after the cyclic load application, the residual stresses in a mechanical component tend to decrease their magnitude (De Giorgi 2011). Dattoma, De Giorgi, and Nobile (2004) studied the relaxation process of the residual stresses of a welded component, due to the application of a cyclic external load and the authors' results showed that the initial residual stress level decreased significantly, even after the first load cycle (Dattoma, De Giorgi and Nobile 2004). Zhuang and Halford (2001) also concluded that the residual stresses present in a component that is under a service loading will undergo varying degrees of relaxation. Also, the relaxation resulting from cyclic loading depends on:

- ✓ The initial magnitude and gradient of the residual stress field and degree of cold working;
- ✓ Fatigue stress amplitude, mean stress ratio and number of cycles;
- ✓ Material cyclic stress-strain response.

In summary, in spite of compressive residual stresses being eminently beneficial to fatigue resistance, cyclic relaxation of residual stresses may decrease this benefit (Zhuang and Halford 2001b). Nonetheless, few studies showed that after load application, residual stresses are higher than the initial ones, and in some particular cases, compressive residual stresses convert to tensile stresses (De Giorgi 2011). De Giorgi (2011) through an experimental work studied the influence of the material yield strength fluctuation on the residual stress field of a component subjected to a fatigue load. The presence of a yield gradient affects the relaxation process since this process is a consequence of yielding at a microscopic scale. Moreover, the component suffered a significant yield stress gradient through the thickness and after applying a bending fatigue load, the residual stresses increased (which caused superficial hardening).

2.1.5. Flexible roll forming

Flexible roll forming is a manufacturing process that allows products to be formed in a continuous process and "…enables not only the flexibility in realization of different products by adjusting the cutting length, but also a variance in the cross section shape along the profile length" (Berner, Storbeck, and Groche 2011). Figure 23 illustrates some examples of profiles obtained by flexible roll forming.

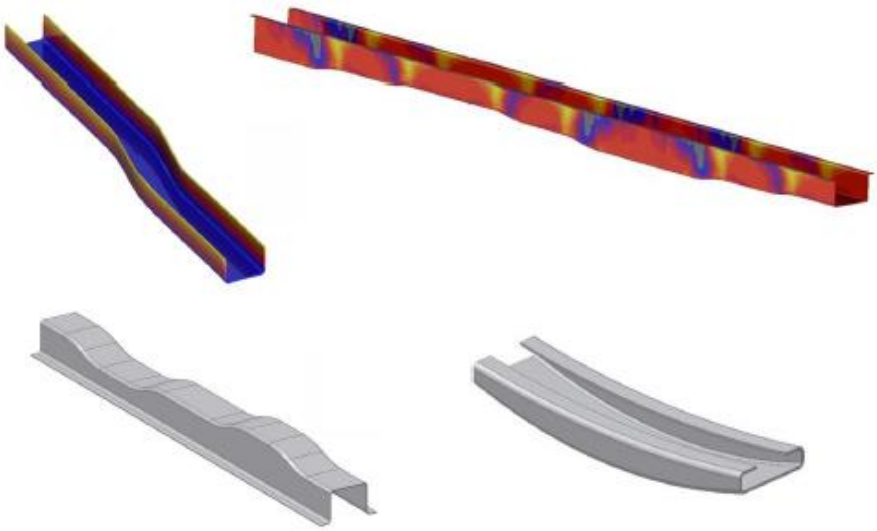

Figure 23 – Profiles obtained by flexible roll forming (Ferreira 2016).

In order to obtain a variable cross-section, normally, the rolls are moved and/or rotated. If both rolls rotate in the same direction, the stand moves forward or back, and if they rotate in opposite direction, the stand rotates (Ferreira 2016). Figure 24 shows a schematic representation of two rolls that are split symmetrically and move and/or rotate to obtain the final profile.

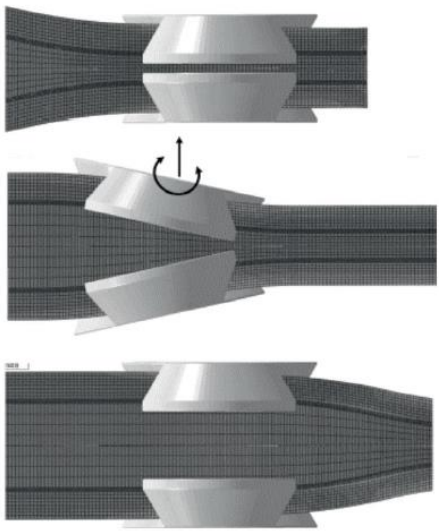

Figure 24 – Concept behind the flexible 3D roll forming process: the rolls are split symmetrically and rotate or move according to the desired contour (Ferreira 2016).

Lindgren and Ingmarsson (2009) develop a new tooling concept to roll form hat-profiles, made of ultra-high strength steel, with variable cross-section in depth and width, with tolerances similar to the ones find in straight profiles. The 3D roll-forming machine used has two translational and two rotational degrees of freedom per axis and a simple cylindrical shape which makes it possible to roll-form different thicknesses of the material with only software changes.

2.2. Fatigue analysis

Fatigue is a progressive, localized and permanent structural change, which causes failure or damage of a component subjected to repeated loading. The repeated fluctuating strains and stresses that cause fatigue failure usually have maximum values less than the tensile strength of the material. In other words, a certain structure may fail at a stress level less than the required to cause failure under static conditions (Boardman 1990; Hassan, Polyzois, and Morris 1994). Cyclic tensile stresses combined with plastic strains can cause fatigue damage. Regarding compressive stresses, these do not cause fatigue damage, although compressive loads may result in local tensile stresses. Fatigue strength of steels are not proportional to hardness and tensile strength of the material, since processing, fabrication, heat treatments surface treatments and service environment also influence the behaviour of the metal exposed to cyclic stressing. Manufacturing processes, such as cold forming also affect the resistance of metal structural members. Together with material properties and loads, the type of load (uniaxial, bending or torsional) must be considered, as well as the loading pattern (periodic loading at a constant or variable amplitude or random loading), magnitude of peak stresses, operation temperature and environment, among others (Boardman 1990).

For most fatigue tests, the stress cycle oscillates between a maximum and a minimum tensile stress or between a maximum tensile stress and a compressive stress (minimum stress). The mean stress, σ_m, is given by Eq. (2.1):

$$\sigma_m = \frac{\sigma_{max} + \sigma_{min}}{2} \tag{2.1}$$

The stress range, σ_r is the difference between the maximum stress and the minimum stress of one cycle:

$$\sigma_r = \sigma_{max} - \sigma_{min} \tag{2.2}$$

The stress amplitude, σ_a is half of the stress range:

$$\sigma_a = \sigma_r/2 \tag{2.3}$$

Normally, tensile stresses are denoted with a positive sign while a negative sign denotes a compressive stress. If $\sigma_m = \sigma_a$, the minimum stress of the cycle is zero. Stress ratio represents the ratio between two specified stress values in a stress cycle, being common to define R as the ratio between minimum and maximum stress:

$$R = \sigma_{min}/\sigma_{max} \tag{2.4}$$

The results of fatigue tests are usually represented in S-N curves diagrams (stress amplitude vs number of cycles to failure) (Boardman 1990).

As mentioned, during the forming processes of cold formed steel profiles, residual stresses are developed and these stresses can be beneficial or detrimental (depending on the magnitude, sign and distribution) for the profile when subjected to fatigue loads.

As far as fatigue design is concerned, two major design approaches can be considered: the first one tries to establish a “safe life” for the structure under a cyclic loading and the second one is

based on a "fail-safe" or "damage tolerant" approach. "Safe-life" approach assumes that the prediction of fatigue life of a component is possible, and the structure can be repaired or replaced before its failure while the "fail-safe" approach implies that a failed component could be temporary tolerated by providing alternate load carrying members and sizing them to reasonable sustained load levels (Hassan, Polyzois, and Morris 1994).

There are three main strategies in fatigue damage modelling or evaluation (Stephens et al. 2001):

- Nominal stress-life (S-N curves) method or Wöhler method – this method uses nominal stresses and relates them with fatigue strength for notched and unnotched members;
- Local strain-life (ε – N) method or Coffin-Manson method – this method uses directly the local strains at a notch and relates them with smooth specimen strain-controlled fatigue behaviour;
- Fatigue crack growth (da/dN) or Paris method – this method is based on Fracture Mechanics and it uses fatigue crack growth rate equations to obtain the number of cycles required to grow a crack.

EN 1993-1-9 (2005) provides methods for the assessment of fatigue resistance of members, connections and joints subjected to fatigue loading. This method is applicable to all types of structural steels, stainless steels, and unprotected weathering steels (with a few exceptions). The method for fatigue assessment is based on S-N curves.

EN 1993-1-9 (2005) refers that nominal or geometric/hot spot structural stresses should be calculated at the site of potential fatigue crack initiation and that for constant amplitude nominal stress ranges, the fatigue strength can be obtained using Eq. (2.5).

$$\Delta\sigma_R^m \, N_R = \Delta\sigma_C^m \, 2 * 10^6 \tag{2.5}$$

N_R is the design life time expressed as a number of cycles related to a constant stress range, m is the slope of fatigue strength curve and $\Delta\sigma_C$ is the reference value of the fatigue strength at N_c= 2 million cycles. Eq. (2.5) is valid for a maximum of 5 million cycles and $m = 3$. Figure 25 shows the fatigue strength curves (EC3) for direct stress ranges and various fatigue strength classes.

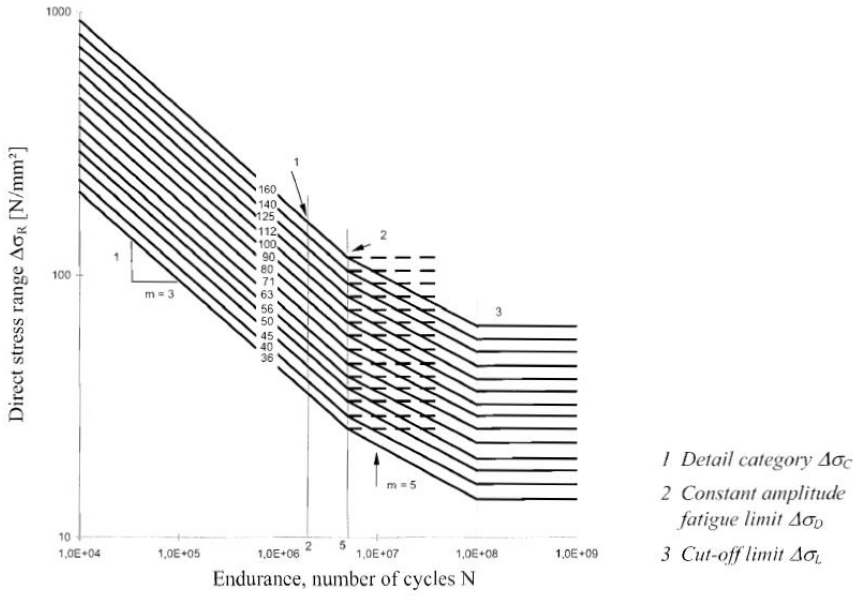

Figure 25 – Fatigue strength curves for direct stress ranges as proposed in Eurocode 3 (EN 1993-1-9 2005).

Each fatigue curve represents a "… quantitative relationship between the stress range and the number of stress cycles to fatigue failure, used for the fatigue assessment of a particular category of structural detail" (EN 1993-1-9 2005). Detail category 160 represents plain members that had been rolled or extruded and characterizes the curve with the highest fatigue strength, which means that no detail can reach a better fatigue strength at any number of cycles.

To sum up, the basis of current design approaches, such as Eurocode 3: Part 1-9, is the S-N approach, which relates the stress range applied to the structure with the fatigue life.

As an alternative to this S-N global approach, as referred before, there are some local approaches to fatigue and Fracture Mechanics, as long as the basic fatigue properties of the material are known or established. "The local approaches, recognizing the localized nature of the fatigue damage, propose the correlation of a local damage parameter (e.g. strain, energy) with the number of cycles required to initiate a macroscopic crack" (Jesus et al. 2012). Basquin (1910) (Eq. (2.6)), Coffin (1954) and Manson (1954) (Eq. (2.7)), and Morrow (1965) (Eq. (2.8)), established some equations that relates these two parameters, respectively:

$$\frac{\Delta\sigma}{2} = \sigma_f' * (2N_f)^b \tag{2.6}$$

$$\frac{\Delta\varepsilon^P}{2} = \varepsilon_f' * (2N_f)^c \tag{2.7}$$

$$\frac{\Delta\varepsilon}{2} = \frac{\Delta\varepsilon^E}{2} + \frac{\Delta\varepsilon^P}{2} = \frac{\sigma_f'}{E} * \left(2N_f\right)^b + \varepsilon_f' * (2N_f)^c \tag{2.8}$$

σ_f' is the fatigue strength coefficient and b is the fatigue strength exponent, ε_f' is the fatigue ductility coefficient and c is the fatigue ductility exponent, $2N_f$ is the number of reversals to failure, $\Delta\varepsilon$, $\Delta\varepsilon^E$ and $\Delta\varepsilon^P$ are the total, elastic and plastic strain ranges, respectively, $\Delta\sigma$ is the stress range and, finally, E is the Young´s modulus (Basquin 1910; Coffin 1954; Manson 1954; Morrow 1965). In order to determine these constants, fatigue tests of smooth specimens under strain-controlled conditions were necessary to be performed. Moreover, these tests can be used to create the curve of the material that relates the stress amplitude with the strain amplitude.

In Eq. (2.3), the mean stress effects are not taken into consideration, although mean stresses may exist in a component because of the presence of residual stresses or non-symmetric external loading. Mean stresses are found in many applications such as pressure vessels, gear teeth and springs. Morrow developed an expression (Eq. (2.9)) to take this parameter into consideration (Wehner and Fatemi 1991):

$$\frac{\Delta\sigma}{2} = (\sigma_f' - \sigma_m) * (2N_f)^b \tag{2.9}$$

Jesus et al. (2012) performed experimental fatigue tests on smooth specimens as well as fatigue crack propagation tests, in order to compare the fatigue behaviour between S355 mild steel ($E =$ 210,5 GPa). The fatigue tests were performed with a strain ratio, R_ε of -1. Table 2 displays the cyclic constants obtained by the experimental work along with other fatigue parameters previously referred.

Table 2 – Cyclic elastoplastic and fatigue properties of S355 structural steel (Jesus et al. 2012).

Material	K' **[MPa]**	n'	σ'_f **[MPa]**	b	ε'_f	c	$2N_f$
S355	598,85	0,0757	952,2	-0,089	0,7371	-0,664	7095

2.2.1. Fatigue analysis of cold formed steel profiles

As previously stated, hot-rolled steel structural members and connections possess fatigue design guidelines. However, there are not acceptable design guidelines regarding cold-formed steel members and connections. FASTCOLD project's goal is to develop general design rules for the design of cold formed steel members and connections subjected to fatigue loading. This sub-chapter presents a review of some of the available test data regarding fatigue design recommendations of cold formed steel members. Literature regarding this matter is quite limited, especially for fatigue life of cold roll formed steel members.

Klippstein, between 1980 and 1988, developed a multi-year project that aimed at assessing the fatigue behaviour of cold-formed steel members and connections (Laboube and Yu 1999). Klippstein (1980) work emerged due to the development of ground-transportation and agricultural-equipment industries, which led to the need for high-strength steel sheet and light weight profiles, along with the development of new or improved fabrication techniques. Fatigue design problems may occur due to these new materials and manufacturing processes. Klippstein (1980) developed a fatigue test on 24 specimens with several different fabrication details. Steels with different yield strengths and different welding processes were used in the investigation. The results were compared with fatigue design curves for hot-rolled and welded-plate beams used in bridges and buildings (rolled beams and plates). The data collected proved that conservative design curves previously mentioned are suitable for steel sheet details. In other words, the author concluded that fatigue design "rules" developed for large details used in bridges and buildings would be suitable for small details fabricated from steels sheet used in the ground transportation and agricultural-equipment industries.

Klippstein in 1981 in his technical paper *Fatigue Behavior of Steel-Sheet Fabrication Details*, for the *International Congress and Exposition*, developed an experiment with 77 cold-formed steel sheet specimens subjected to a constant amplitude stress cycle, with the intent to develop stress-range fatigue design concepts. The specimens used were made of steel sheets with different yield strengths and several types of beam details were analysed, such as cold formed corners, rolled steel sheet surfaces, drilled holes, among others (quoted in Laboube and Yu 1999). In 1985, Klippstein in his technical paper *Fatigue of Fabricated Steel-Sheet Details - Phase II*, for the *International Congress and Exposition* continued his research with fabricated steel sheet details. In the same year, the author developed, based on his previous researches, an appropriate design methodology based on mean fatigue life curves (S-N curves). Different details were assigned to an adequate fatigue design category (quoted in Laboube and Yu 1999). Klippstein, in 1988, in his technical paper *Fatigue Design Curves for Structural Fabrication Details Made of Sheet and Plate Steel*, proposed a classification system for various stress ranges. This classification system is presented in Table 3. Note that constant C_f originated from Fisher's (1970) equations provides a relationship between stress range and life cycles (quoted in Laboube and Yu 1999):

$$\log(N) = \log(C_f) - m * \log(F_{SR}) \quad (2.10)$$

$$C_f = b - n * s \quad (2.11)$$

Where:

- N is the number of full stress cycles to failure;
- m is the slope of the mean fatigue analysis curve;
- F_{SR} is the effective stress range
- b is the intercept of mean fatigue analysis curve;
- n is the number of standard deviations to obtain a desired confidence level;
- s is the approximate standard deviation of fatigue data.

For constants n and s, Klippstein recommended 2 and 0,25 respectively. In Table 4, values for constant b are summarized.

Table 3 – Klippstein's fatigue design categories (Laboube and Yu 1999).

Description	**Stress Category**	C_f
Base metal and components with as received surfaces, including sheared edges and cold-formed corners.	A	3,16E10
Base metal and weld metal in members connected by continuous longitudinal fillet welds.	B	1,0E10
Continuously welded attachments to a plate or a beam, transverse web stiffeners, transverse fillet welds, weld washers with outside diameter less than 2 inches, and continuous longitudinal welds in regions of cold-forming and subsequent welding	C	3,16E9
Weld washers with diameter ranging from 2 to 4 inches. Any welded attachment with a length of 2 to 4 inches parallel to the direction of the applied stress. Transverse welds in regions of cold-forming.	D	1,0E9
Attachments longer than 4 inches parallel to the direction of the applied stress, and intermittent welds parallel to the direction of the applied stress.	E	3,16E8
Bolt and screw holes in connections and other punched and drilled holes, spot welds, and shear connectors.	F	1,0E10

Table 4 – Intercept for mean fatigue curves (Laboube and Yu 1999).

Stress Category	***b***
A	11,0
B	10,5
C	10,0
D	9,5
E	9,0
F	10,5

Hassan, Polyzois, and Morris (1994) studied the influence of wind as a time-variant loading, inducing fatigue damage in transmission towers. The primary goal of the investigation was to study the axial fatigue behaviour of full-size cold formed steel members normally used in the construction of transmission towers. 52 constant amplitude axial fatigue tests were performed with a load ratio of -1. Fatigue loads were applied in triangular wave form. However, the shape of the wave was not crucial. The attention was focused on the upper and lower peaks of loadings. Hassan, Polyzois, and Morris (1994) concluded that the dominant stress variable that had higher impact on fatigue behaviour of cold-formed steel members was the stress range. Also, most fatigue failures appeared at the extremity of the end hole of the specimens. Furthermore, a stiffness reduction was detected (cyclic-dependent softening) for all tested specimens at the final stage of the fatigue life. Another important conclusion was that fatigue tests performed at -50 °C displayed an increase of 11,5% in the stress range levels as opposed to specimens tested at room temperature.

Gustavsson, Larsson, and Melander's (1997) technical paper compared the constant amplitude fatigue properties of six low carbon steels used in the automotive industry as pressed structural steels. Pressed sheet components are often used for the automotive industry as structural components and may be subjected to local high stresses due to loading and geometry, affecting their fatigue life. Moreover, this paper offered a life prediction of pressed sheet specimens involving both the local strain approach and fatigue crack growth. For this experimental work, both unnotched sheet specimens and pressed specimens developed in a laboratory were analysed. Gustavsson, Larsson, and Melander (1997) concluded that:

- ✓ Increasing the tensile strength of the material leads to an increase of fatigue strength of the fully reversed strain controlled fatigue testing of smooth specimens and of the fully reversed bending test of press sheet specimen;
- ✓ The experimental tests with the pressed specimens presented higher fatigue strength than the life predictions based on the local strain approach using non-prestrained specimens;
- ✓ Fatigue life prediction is achievable by superposing a fatigue crack growth estimate of the fatigue life to the local strain approach.

2.3. Finite element method analysis

According to Oñate (2009) "The Finite Element Method (FEM) is a procedure for numerical solution of the equations that govern problems found in nature (…) FEM is understood in mathematical circles as a numerical technique for solving partial differential or integral equations". Through this method it is possible to attain the evolution in space and/or time of variables that characterise the behaviour of a physical system. FEM is an excellent method that allows the computing of stresses, strains and displacements in a structure under a set of loads. FEM is a numerical method that aims the transformation of mathematical expressions into a set of algebraic equation which depend on a finite set of parameters. These numerical methods when applied to structural engineering problems incorporate mathematics, material modelling and computer science. A finite element is a small portion of a continuum, in this case of a solid or structure (Oñate 2009).

FEM can be used in a variety of applications, such as stress and thermal analysis of industrial parts, seismic analysis of dams and power plants, crash car analysis, fluid flow analysis, surgical procedures analysis, among others. Manufacturing processes are also simulated by finite element method. For instance, sheet metal forming is simulated to ensure that the component can be produced and that after springback, the part still obeys the required specifications (Fish and Belytschko 2007).

In roll forming processes, "Workshop tests using trial-and-error method is the common practice but it inevitably requires a large amount of material and time" (Bui and Ponthot 2008). That is one of the reasons that makes numerical simulation an attractive and less expensive alternative, reducing the time necessary for all roll pass design of new products (Bui and Ponthot 2008). For this reason, the software used for the simulations presented in this dissertation were COPRA® RF and COPRA® FEA RF (developed by a German company, data M, focused on the development of design and simulation tools for sheet metal forming). The design software development was based on HP-UX ME10 and AutoCAD® (COPRA® RF) (Ferreira 2016). COPRA® FEA RF directly imports data from COPRA® RF and gives information about forces, stresses, strains as well as a 3D visualization of the final profile granting the possibility to detect three-dimensional defects and springback before the actual manufacturing process. Furthermore, COPRA® FEA RF simulates the roll forming process by non-linear elastoplastic calculation, using MSC Marc/Mentat solvers (data M Sheet Metal Solutions GmbH n.d.).

"The Marc system contains a series of integrated programs that facilitate analysis of engineering problems in the fields of structural mechanics, heat transfer, and electromagnetics", which are Marc and Mentat. These two programs work together in order to create geometric information to define the structure, analyse the structure and portray the graphic results. Marc for Analysis is used "… to perform linear or nonlinear stress analysis in the static and dynamic regimes, to perform heat transfer analysis and electromagnetic analysis", while Mentat "… is an interactive computer program that prepares and processes data for use with the finite element method". Mentat is responsible for generating and displaying a mesh, boundary conditions and loadings (MSC Software Corporation 2013b).

Over the last few years, quality management in roll forming became a crucial aspect, due to the demand for good material, as well as tight machine and tooling tolerances, reason why the

necessity for the implementation of finite element methods (Abee, Sedlmaier, and Stephenson 2010). Moreover, as mentioned, reducing cost in the metal form industry goes through the implementation of numerical simulation using the finite element method. The number of passes, the flower design or bending strategy can be studied and important design decisions can be made before the actual manufacturing process (Ferreira 2016). Also, a more proactive relationship between the tool design, the machine operator and R&D personal can be achieved increasing the company´s know how about the roll forming process. When introducing FE simulation of roll forming, the company aims to (Abee, Sedlmaier, and Stephenson 2010):

- increase the understanding of the roll forming process;
- predict achievable geometrical tolerances;
- optimize the process by reducing forces, roll tool wear, energy consumption, among others;
- predict and optimize product quality.

To conclude, the design process is upgraded when using numerical simulations, since a new iteration to the process can be introduced, as shown in Figure 26 (Ferreira 2016).

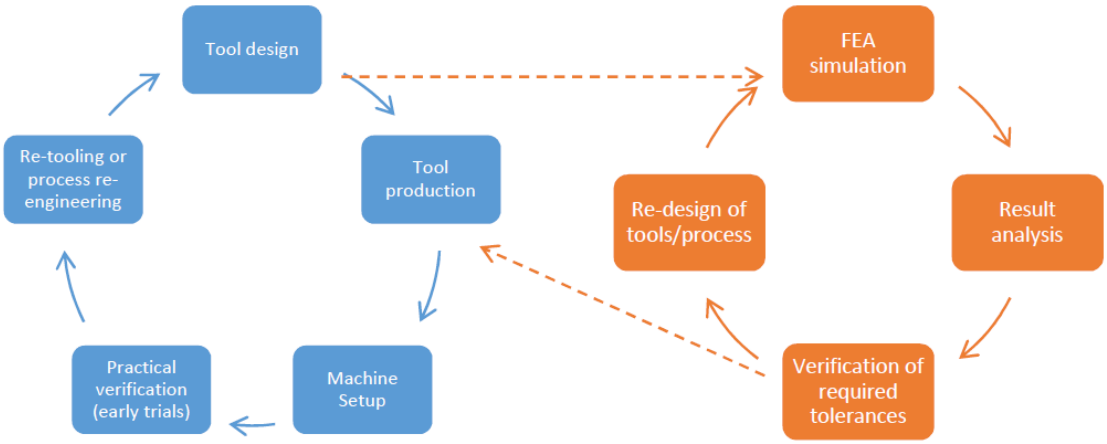

Figure 26 – Design process of a roll forming line; in blue is the traditional process of trial and error; in orange, the upgraded process with virtual testing; dashed lines represent the connection between the cycles (Ferreira 2016).

2.3.1. Softwares based on Finite Element analysis for simulation of cold roll forming processes

The present sub-chapter lists some of the softwares, based on Finite Element analysis found in literature, regarding numerical simulation of cold roll forming processes.

Heislitz et al. (1996) used finite element analysis – 3D FEM code PAM STAMP – to predict strain distributions and sheet geometry during and after the roll forming process and to compare the results with previously conducted experiments. For the simulation, 8 node brick elements were used to generate the mesh of U-channel profile with three bending stations, while four node (rigid) shell elements were used to model the roll surfaces.

Hong, Lee, and Kim (2001) developed a simulation program to examine the roll forming process. The program was based on finite element analysis (using COPRA® FEA RF package) and a kinematic steady-state condition was used.

Farzin, Salmani Tehrani, and Shameli (2002) studied the buckling limit of strain in cold roll forming processes, using LUSAS 12.3 as the finite element analysis software. For this investigation, a quadratic quadrilateral thin shell element (QSL8) was selected.

Lindgren (2007a) analysed the influence of yield strength on longitudinal peak membrane strain at the edge flange and the deformation length, through finite element simulations. The finite element package used was MSC Marc/Mentat. The strip was modelled with a bilinear thick shell element type number 75 (four-node element).

Bui and Ponthot (2008) performed a parametrical study of cold roll-forming processes of a U-channel profile. The goal was to compare numerical results of longitudinal strains and displacement trajectories with experimental results. The simulation was performed with a full 3D finite element model (8-node EAS brick elements), using finite element code Metafor.

Muller, Barrans, and Blunt (2011) developed a new method for validating numerically predicted plastic deformation in a cold formed metal strip. To achieve that, Finite Element Analysis package ABAQUS® was employed to simulate the cold roll forming process of V-band clamps (widely used in the automotive, aircraft and aerospace industries). A two dimensional reduced integration linear plane strain elements (CPE4R) was used along with three different meshes. Each pair of rollers was modelled as analytical rigid bodies. The analysis was carried out in an implicit static environment.

Kang et al. (2014) studied the influence of material strength (martensitic steels) on fillet radius of formed square tubes and corner thickness. A 3D elastic-plastic roll forming finite element model was established using ABAQUS® in order to test the influence of the material and process parameters.

Chapter 3

Numerical simulation of a U-channel profile

The following chapter presents simulation models generated for a U-channel profile (using COPRA® FEA RF package), as well as the material model and the results and conclusions of these simulations. The main objective of this chapter is to study the influence and effects of roll forming processes on the geometry (three-dimensional defects) and on the residual stresses and strains of the profile. To achieve that, this section exhibits a preliminary parametric study, where simulation 1 is considered the reference of this study. A U-channel profile (with the same overall dimensions as the Z-section (rail section) profile to be tested in FASTCOLD project) was selected due to its simplicity of modelling as well as its lower CPU time requirements. Finally, this chapter also includes a study on the influence of mechanical cyclic loads on the residual stresses of the profile, as well as an estimative of fatigue life of U-channel components subjected to this type of loads.

3.1. Model definition

3.1.1. Modelling concepts

During this investigation, the forming rolls were modelled as rigid bodies while the steel strip was defined as a deformable body. For most simulations, including simulation 1, null friction between the rolls and the strip was considered. For the models of every simulation with driven rolls, the rolls are fixed in space while the strip moves forward through the stations due to frictional force. For non driven simulations, the opposite procedure is applied.

3.1.2. Geometry and flower

The roll design was developed in COPRA®RF and simulation models were prepared automatically by the COPRA®FEA RF package from the roll design developed in COPRA® RF. Due to the symmetry of the profile during the roll forming process, only half was simulated, reducing the CPU time of each simulation.

For the first simulation (simulation 1, the reference), the steel strip has a length of 520 mm and an initial thickness of 3,5 mm (Figure 27). These dimensions remained equal for all simulations of the U-channel profile. The distance between stations, for simulation 1 is 400 mm, the forming

line is composed of six stations (Figure 28) and the bending sequence is 10°/ 22°/ 36°/ 52°/ 69°/ 90° (Figure 29). The flower was optimised so that the distribution of strains was as even as possible, in order to avoid peaks of strains that can lead to defects. The flower diagram plays an important role in the flow of the material and in the magnitude of the stresses generated by the forming process.

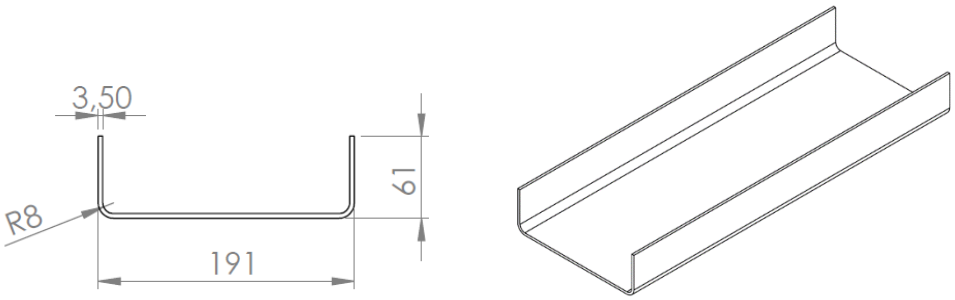

Figure 27 – Dimensions [mm] of the U-channel profile.

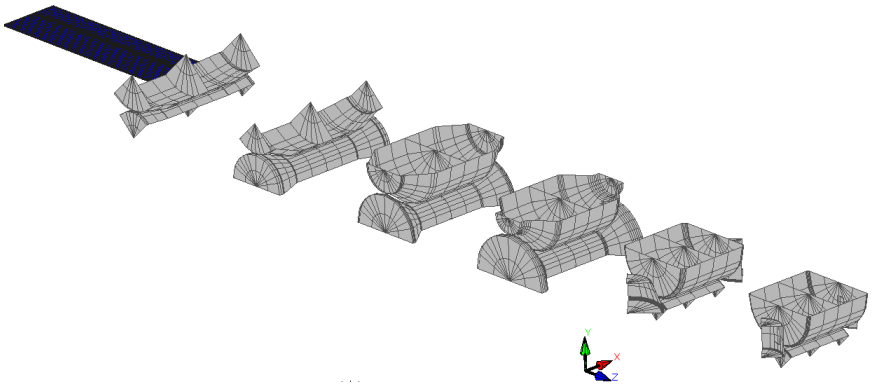

Figure 28 – Stations and respective rolls of simulation 1.

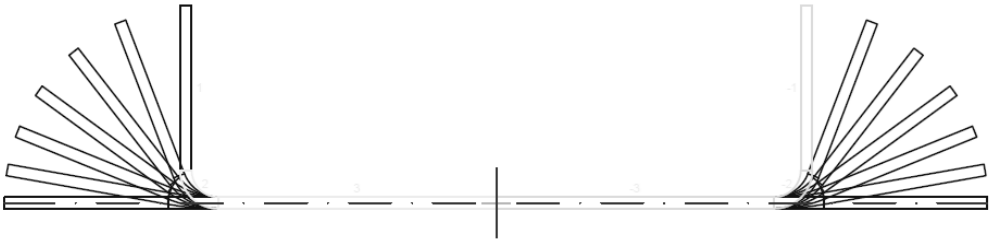

Figure 29 – Flower design of the U-channel profile.

Rolls design of the simulations presented in sub-Chapter 3.2 are illustrated in Appendix 1, Figures 1.1-1.15.

For all simulations, the global coordinate system used was:

- *x* for the horizontal direction perpendicular to the sheet rolling direction;
- *y* for the thickness direction in the flat sheet (vertical);
- *z* for the sheet travel direction (roll forming direction).

3.1.3. Boundary conditions

Due to the symmetry of the profile, only half was simulated. The *X*-direction boundary condition (Figure 30) is applied to all nodes along the symmetry line of the profile, preventing the material to move in the *x* direction.

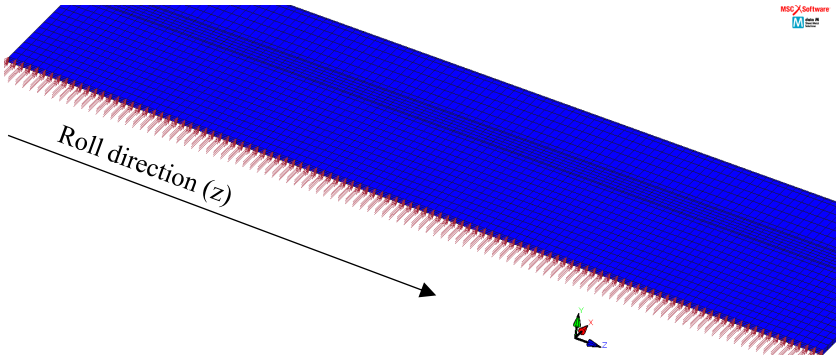

Figure 30 – *X*-direction boundary condition due to the symmetry of the U-channel profile.

On the tail end of the profile, a *Y*-direction boundary condition to restrain the displacement of the last three nodes in y direction (Figure 31) was used, so that the strip would not experience rigid body motion. Only three nodes were selected, to allow the movement of the strip in this direction in the remaining nodes. In addition, those three nodes will be cut off in the end of the simulation. The last three nodes are used, by default, as a result of various experiments performed by data M that proved that this location has the least influence in the roll forming process.

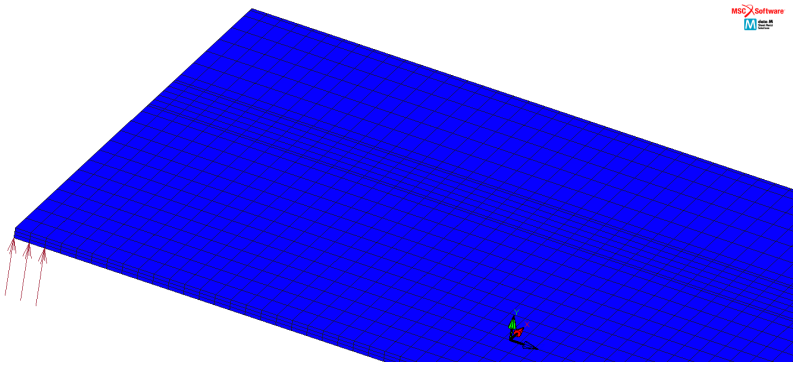

Figure 31 – *Y*-direction boundary condition - restriction of three nodes in the middle of the tail end of the U-channel profile.

The *Z*-direction boundary condition (Figure 32) is necessary to simulate or assume the continuous existence of the strip, since industry normally provides the raw material in a coil. This boundary condition ensures that the strip maintains the same length, so that the numerical simulation is as realistic as possible, since in the industry the product is cut off from the coil with the dimensions required.

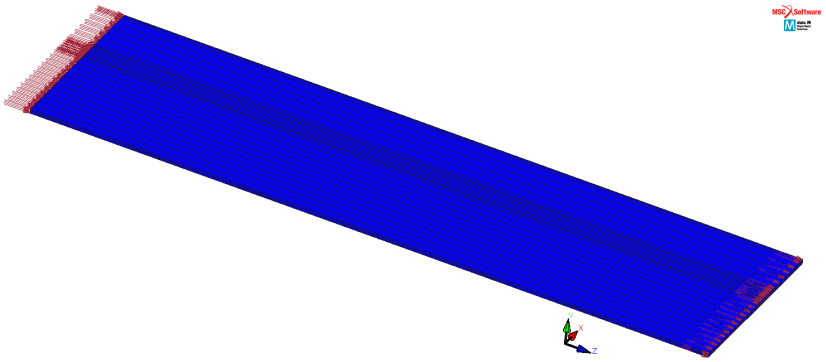

Figure 32 – *Z*-direction boundary condition (boundary condition to simulate the continuous existence of the strip).

Fs boundary conditions (Figure 33) are only applied when the free cut is in place (z and y direction boundary conditions are not activated). Both extremities of the strip are locked along all directions as well as the element right before the region where the strip will be cut off. This element needs to be locked, so that the strip also does not experience rigid body motion after the end cut.

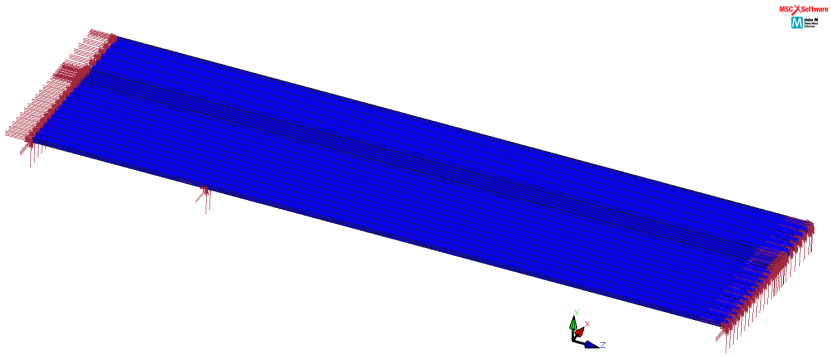

Figure 33 – *Fs* boundary condition (due to the free cut of the U-channel profile).

3.1.4. Element type

For all simulations, the element type chosen was element type 7 (eight node hexahedral solid element with trilinear interpolation). This element is the default type element of the software and "it is used by data M in the COPRA® FEA RF package and typically used in most of their simulations since their practical experience shows that it provides a good representation of the roll forming behaviour of steel materials" (Ferreira 2016). Moreover, previous research at data M showed that the use of shell elements is not appropriate for this type of analysis, since the material behaviour through the thickness is not constant and must be represented. The element stiffness is determined using eight-point Gaussian integration (Ferreira 2016).

3.1.5. Mesh definition

"Mesh definition is the process of converting a physical problem into discrete geometric entities for the purpose of analysis. Before a body can undergo finite element analysis, it must be modelled into discrete finite element analysis" (MSC Software Corporation 2013a).

Mesh definition was based on the experience of roll forming simulations at data M. For "subdivisions straight entities", i. e. the number of subdivisions in straight entities of the section for FEA calculation, value 4,3 was selected. The number of subdivisions for arc entities was 2,2 and the number of subdivisions in the rolling direction was 1,5, according internal COPRA® FEA RF mesh size definition. Initially, COPRA2FEA (functionality of FEA for pre-processing) set 1 as the default value for all parameters (Figure 34). Increasing this value means increasing the density of elements, which leads to higher computation times, but expected better results.

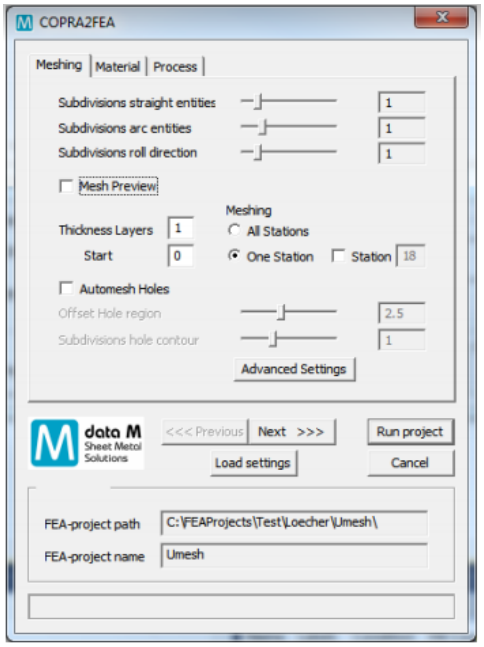

Figure 34 – Default values of subdivisions for the mesh (data M Sheet Metal Solutions GmbH 2015).

More than one element across the thickness of the sheet was important to use since the residual stresses through the thickness play an important role in this investigation (due to the fatigue studies carried out further in this chapter). Most simulations, including simulation 1 use three elements across the thickness of the profile. Figure 35 displays the resulting mesh of the strip.

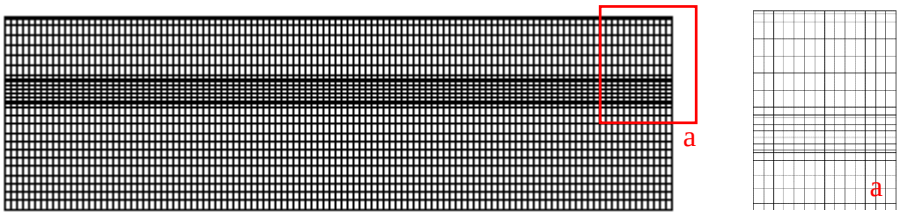

Figure 35 – Mesh of the U-channel profile.

Concerning the number of elements of the simulations presented in subchapter 3.2, simulation 7 has 9990 elements, simulation 4 has 35952 elements, and the remaining simulations have 9324 elements. Note that, the values introduced to define the mesh do not have a direct relation with the element size and not all elements have the same size. The smallest element of simulation 1 has 1,221 x 4,685 mm and is located at the beginning and at the end of the corner region and in the edge flange of the profile.

3.1.6. Material model

The elastic material properties were necessary to be introduced, i.e. the Young´s modulus [N/mm^2] and the Poisson´s ratio, as well as the plastic behaviour of the material, the latter possibly defined directly using Swift's law (Eq. (3.1)):

$$\sigma = K(\varepsilon_0 + \varepsilon_p)^n \tag{3.1}$$

Where:

- σ is the true stress;
- ε_p is the true plastic strain;
- K, n, and ε_0 are material constants determined form a uniaxial tensile test.

However, if the flow stress curve is unknown, it is possible to use the material´s technical data sheet to describe the plastic behaviour, entering the values for yield strength [MPa], ultimate tensile strength [MPa] and the percentage of elongation [%] at the ultimate tensile strength. After inserting these values, the software creates the stress-strain curve that represents the behaviour of the material. When developing the model for the U-channel profile, the experimental flow stress curve was still unknown, reason why the material´s technical data sheet was used. The material chosen for the U-channel profile was S350GD high-strength galvanized coil steel (mechanical properties are presented in Table 5) due to its strength characteristics as well as its corrosion resistance due to zinc coating. This steel is frequently used for manufacturing bent profiles for lightweight thin-walled steel structures.

Table 5 – Properties of S350GD steel (Metinvest ® Technical brochures).

Name	**Yield Strength $R_{p\ 0,2}$ [MPa]**	**Ultimate Tensile Strength R_m [MPa]**	**Elongation at Ultimate Tensile Strength A_{80} [%]**	
S350GD	350	420	16	
Chemical Composition (%)				
C	**Si**	**Mn**	**P**	**S**
0,2	0,6	1,7	0,1	0,045

The values introduced for the elastic properties were 210 GPa for Young´s modulus and 0,3 for Poisson's ratio. With these inputs, the software estimated the constants of Swift's hardening law, presented in Table 6.

Table 6 – Swift's hardening law parameters estimated by the software.

K [MPa]	n	ε_0
646,658	0,148	0,016

In addition, the software displays a plot of the plastic behaviour of the material, as shown in Figure 36.

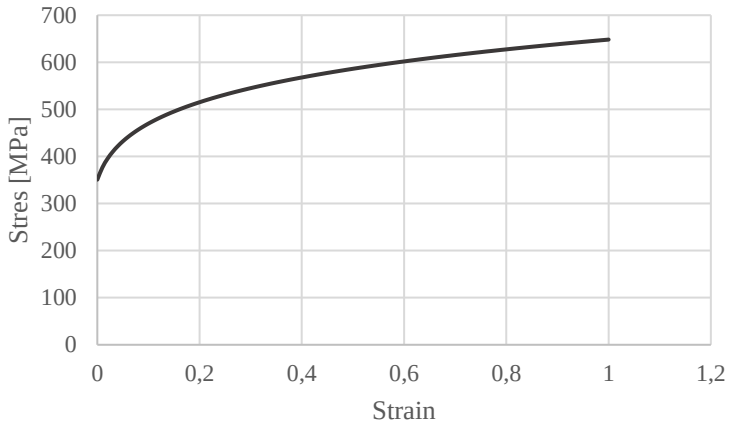

Figure 36 – Stress vs strain diagram that describes the plastic behaviour of the material (S350GD) using Swift´s hardening law.

As regards the constitutive model used in the simulations, the Von Mises yield theory was used with isotropic hardening, which is a common approach for roll forming simulations.

As concerns sheet metal forming strategy, the "coil" option (continuous process) was used instead of "pre-cut length". Sheet metal industries normally use raw material in a coil, which means the forming process is continuous without any pre-defined length (data M Sheet Metal Solutions GmbH 2015). The length of the strip is 1,3 times the distance between each station. When the "coil" option is selected, the software develops a model of a strip with infinite length, to represent the continuous forming that normally occurs in the industry. For this reason, some boundary conditions are added to the model (z direction boundary conditions). In addition, the option "cutting (default 0,5*length)" was selected. The first and final quarter parts of the profile are inactivated when the workpiece leaves the final station. This option simulates the reality in roll forming, since the coil is cut off in order to obtain the product. This operation is responsible for a stress relief that should be taken into consideration in the numerical analysis.

3.2. Parametric study

As mentioned before, simulation 1 is the reference of the following parametric study. As one might observe, there are many parameters that have some influence on the roll forming process, such as the number of stations, the radius/thickness ratio, the distance between stations, the material properties, the friction of the driven rolls and so on. Table 7 illustrates the simulations plan with the correspondent parameters. All simulations have the same mesh (with exception of simulation 2 that has four elements across the thickness instead of three elements) and boundary conditions, as well as the same element type.

Table 7 – Parametric study proposed for the U-channel profile.

	Number of stations	**r/t**	**Distance between stations [mm]**	**Material**	**Driven Rolls**	**Number of elements (thickness)**
Simulation 1	6	2,286	400	S350	no	3
Simulation 2	6	2,286	400	S350	no	**4**
Simulation 3	**9**	2,286	400	S350	no	3
Simulation 4	6	2,286	**1000**	S350	no	3
Simulation 5	6	2,286	400	S350	**yes (μ= 0,15)[a]**	3
Simulation 6	6	2,286	400	S350	**yes (μ= 0,2)[a]**	3
Simulation 7	6	**1,143**	400	S350	no	3
Simulation 8	6	**3,429**	400	S350	no	3
Simulation 9	6	2,286	400	**S460[b]**	no	3

[a] μ = friction coefficient

[b] Mechanical properties of S460 steel are presented in Appendix 2, Table 2.1.

3.3. Nomenclature

This section illustrates the different terms and nomenclature used in this dissertation. Figure 37 presents some nomenclature related to the simulations of the U-channel profile.

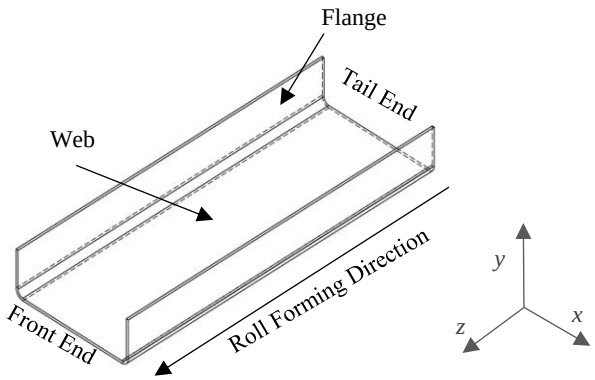

Figure 37 – Designated terms for different sections of the U-channel profile and reference global coordinate system.

3.3.1. Measurement of residual stresses along *xx* direction

In order to measure transverse residual stresses along the *xx* direction of each element, four paths were created (path 1 belongs to plane i, path 2 to plane ii and so on), as Figure 38 shows. Plane i and plane iv are located at the front and tail ends, respectively, while plane ii and iii are located approximately at a distance of 65,7 mm from the front and tail ends, respectively (these planes are located in the 15th node counting from the correspondent extremity of the profile).Transverse residual stresses were measured on the top (*yy*=t/2) and bottom (*yy*=-t/2) surfaces of the profile in each path.

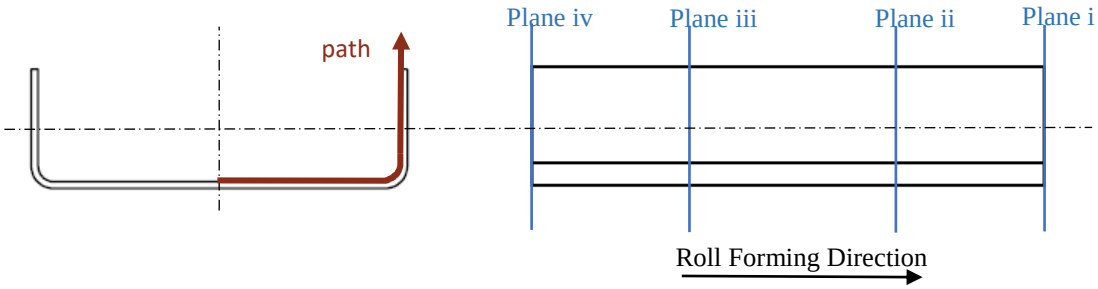

Figure 38 – Paths and planes of the profile created to determine the residual stresses and other parameters in this chapter.

In order to study the through the thickness residual stresses along the *xx* direction of each element, the local/element coordinate system was taken into account, in other words a curvilinear coordinate system that follows the trajectory of elements along the bending trajectory was created, since the *xx* direction of each element does not always match with the *x* direction of the global coordinate system. The software allows the study of results using a customised coordinate system. Figure 39 highlights the differences between these two coordinate systems. Transverse residual stresses were analysed using an element coordinate system.

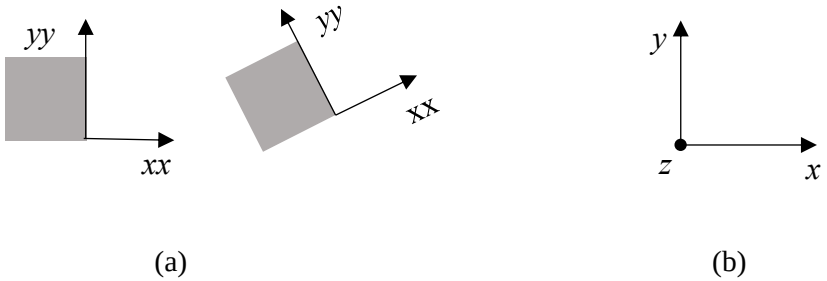

Figure 39 – (a) Local/ Element Coordinate System; (b) Global Coordinate System

Note that in the following results, *xx* direction is the nomenclature used for the element coordinate system, while *x* direction is for the global coordinate system, as it is shown in Figure 39. The local coordinate system is often used since, as the profile bends, extracting residual stresses in a coordinate system similar to a curvilinear system is essential.

Residual stress in the bending zone is one of the most important data to study, since these stresses influence the load-displacement response and ultimate strength of cold formed steel members. The bending zone is divided into four paths across the thickness, as shown in Figure 40. Plots of residual stresses along each path were created in the following subchapter. Figure 40 also illustrates three nodes and the local coordinate system mentioned. Nodes 1 and 3 are in straight segments on the bottom surface of the sheet and node 2 is in the corner.

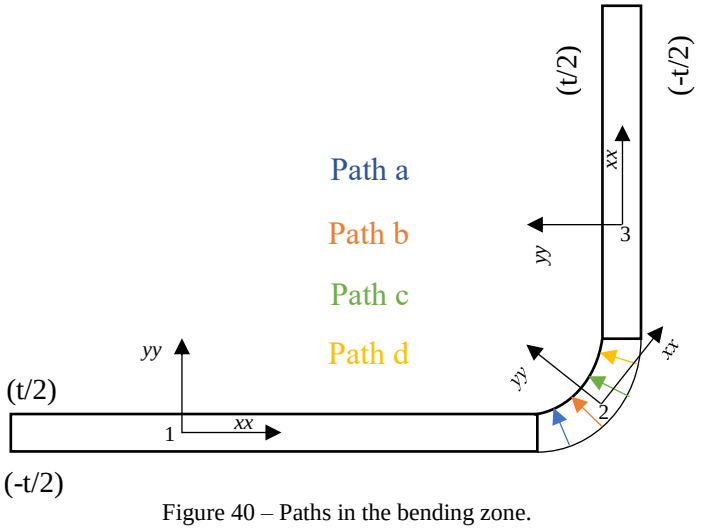

Figure 40 – Paths in the bending zone.

3.3.2. Measurement of bow and springback

Longitudinal bow was measured in the middle of the web of the profile in the roll forming direction (location *a* of Figure 41). Cross bow was measured in the front end and/or in the tail end of the profile in the web (location *b* of Figure 41). Regarding springback, this parameter was measured in the flange of the profile in each plane.

3.3.3. Measurement of longitudinal (z direction) edge strain

Longitudinal edge strain was measured on the top surface near the edge flange of the strip (node location: 2th node from the edge flange and 28th node from the front end of the cut off profile). The location of this node is near the middle of the profile length and approximately 1,2 mm of the flange edge. The red point in Figure 41 illustrates the node where longitudinal edge strain was measured.

3.3.4. Measurement of longitudinal (z direction) plastic strain in the bend zone

Longitudinal plastic strain was measured in the bend zone along the roll forming direction in the 1st node that constitutes the corner region. The red arrow in Figure 41 illustrates the line of nodes where the longitudinal plastic strain in the bend zone was measured.

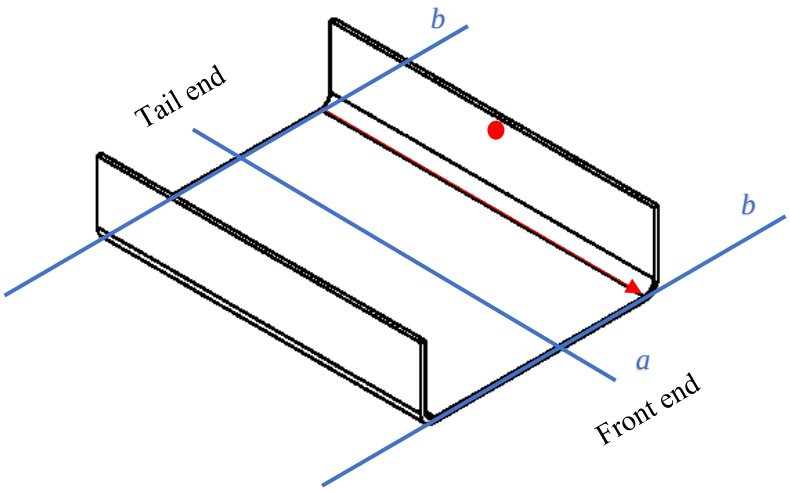

Figure 41 – Location of the regions where longitudinal edge strain, bow and longitudinal plastic strain in the bend zone were measured.

As a side note, the stresses were analysed in the final increment of each simulation after the free cut (increment 1215 for simulation 1). However, for fatigue analysis, the increment right before the free cut (1185) was used to analyse the stresses and strains.

3.4. Roll forming simulations results and discussion

The following subchapter exhibits the results for the simulations that compose the parametric study. Initially, some relevant results for simulation 1 will be presented, as it represents the reference for the whole study. Afterwards, a discussion of results of the remaining simulations and comparison with reference simulation 1 is exposed.

- **Simulation 1 (reference)**

Figure 42 and 43 reveal the field distribution of equivalent Von Mises stress and stresses in the *xx* direction of each element. These distributions represent stresses in the last increment after and before the free cut, respectively and is also possible to visualize the location of the free cut.

The flange of the profile has higher values of Von Mises stresses, since in this process, the flange travels a longer path than the web, leading to higher values of stresses and strains. Furthermore, if the bending process is limited to the elastic domain of the material, when the profile leaves the stand, the strain and stretching will return to the original length. Nonetheless, if the stresses in edge have exceeded the yield point between two bending steps, a permanent strain is introduced in the material, possibly leading to defects such as waviness, twist or other types of deformations. Stresses in the *xx* direction of each element were observed and analysed in increment 1185, since this was the increment used for the simulations for fatigue analysis. Only a portion (approximately in the middle of the profile) is presented in Figure 43, so that it becomes more perceptible the parts of the inner corner surface that are under tension and under compression: most of the inner corner surface is under tension, the only region that is under compression is located in the part of the corner closer to the web. When the material is no longer under the action of the rolls, an elastic springback occurs, which is responsible for the reverse stresses signal expected in the corner. However, due to three-dimensional effects, some irregularities are visible in stresses distributions. Note that, analysis in the cut off sections of the profile were not performed.

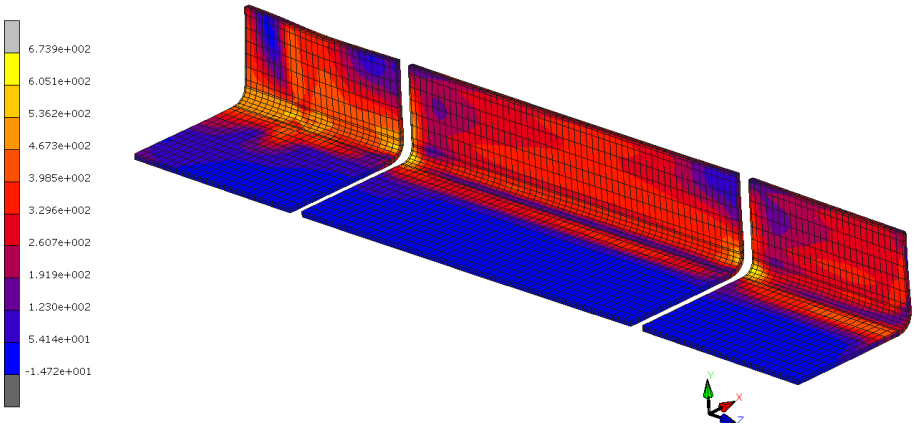

Figure 42 – Equivalent Von Mises stress [MPa] in the last increment of simulation 1 after end cuts (increment 1215).

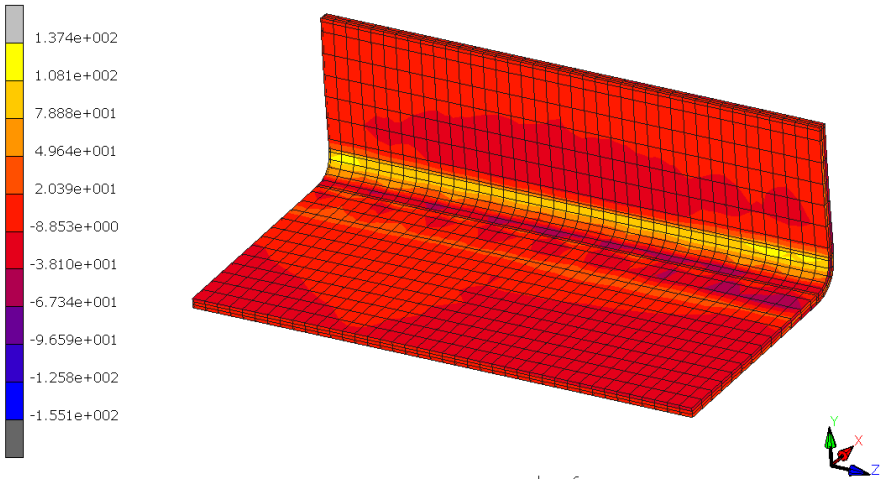

Figure 43 – Stresses [MPa] in the *xx* direction of each element in the last increment before the free cut of simulation 1 (increment 1185).

Regarding longitudinal strains (see section 3.3.3.), peak longitudinal membrane strain is approximately 1,645% (Figure 44). These strains are significantly lower than some values found in literature. Bui and Ponthot (2008) numerically modelled a U-channel profile. The forming line was composed by three stations and the results for the longitudinal strain are displayed in Figure 45. As expected, for a larger number of stations, the peak longitudinal membrane strain decreases, since the applied bending is more gradual, which led to a reduction of strains. Analysing Figure 45, initially the longitudinal strain rises and it reaches a peak, and then, due to springback, it goes down. The longitudinal strain in the strip was above the elastic limit of the material, which led to the development of plastic longitudinal strain and the creation of a permanent deformation (around 0,5%). This plastic deformation can originate the three-dimensional defects mentioned earlier (Bui and Ponthot 2008).

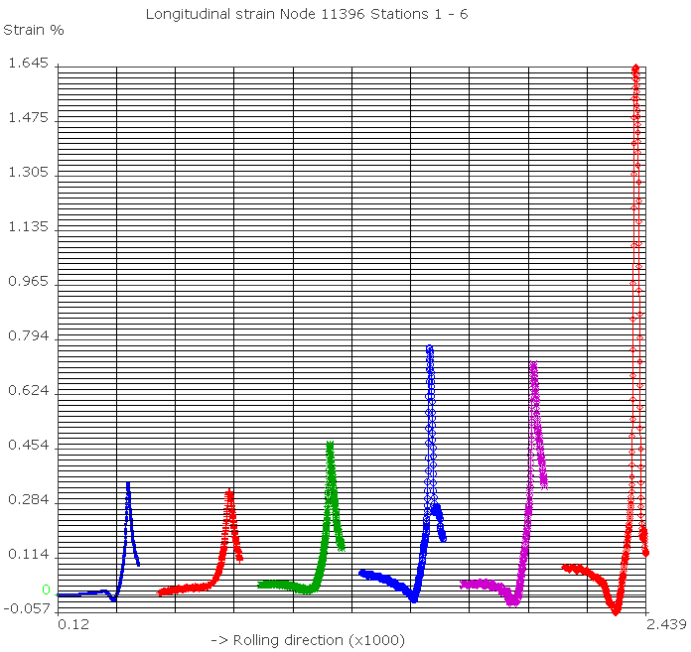

Figure 44 – Longitudinal membrane strain for simulation 1.

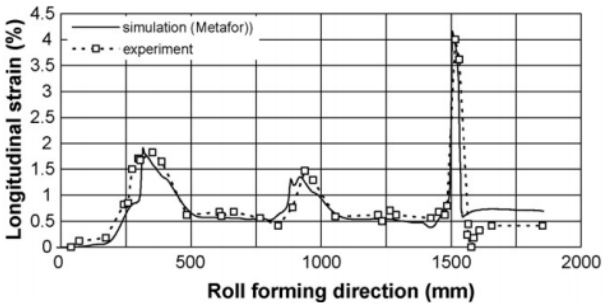

Figure 45 – Longitudinal strain at a distance of 1,5 mm away from the strip edge for a U-channel profile with a forming line composed of three stations (Bui and Ponthot 2008).

- **Simulation 1 vs Simulation 2**

As a reminder, simulation 1 has three elements along the thickness of the profile, while simulation 2 has four elements across the thickness. Figures 46-49 show the through thickness residual stresses (see section 3.3.1.) along the *xx* direction of each element (as mentioned, for these results, the local/element coordinate system was used instead of the global coordinate system).

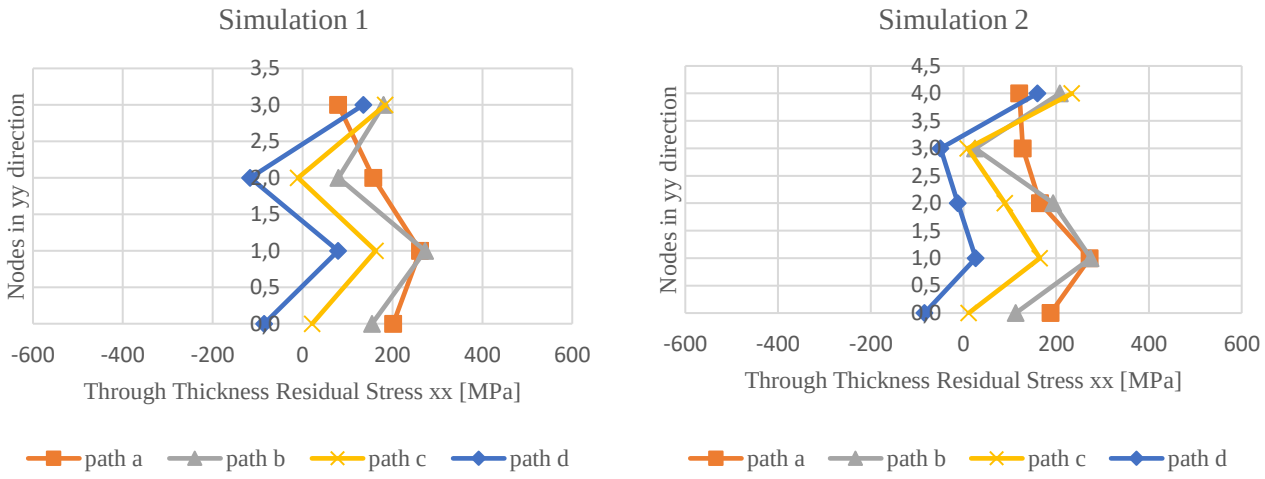

Figure 46 – Comparison of through thickness residual stresses [MPa] along the xx direction between simulation 1 and 2 for plane i.

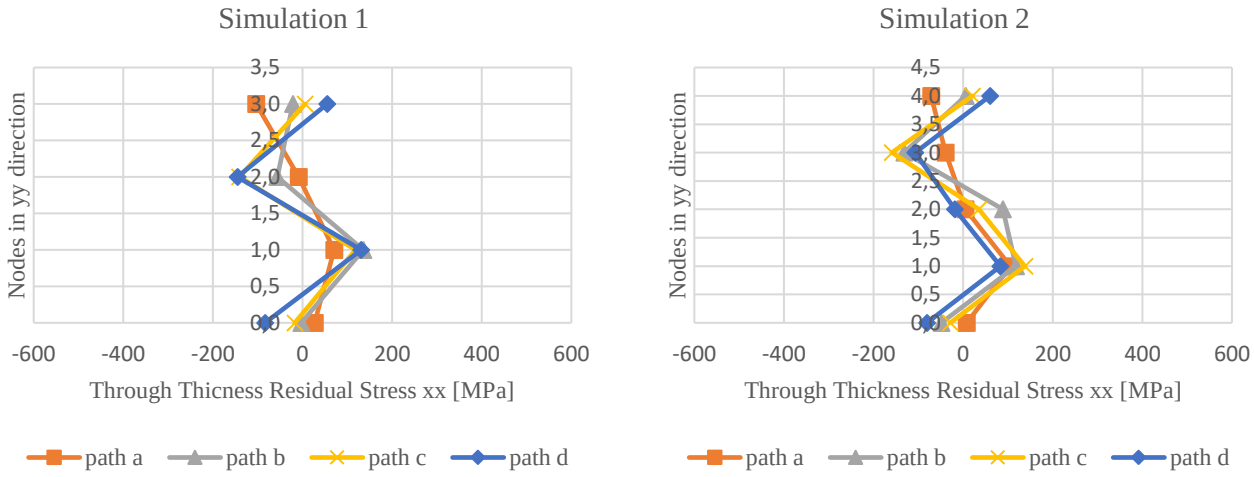

Figure 47 – Comparison of through thickness residual stresses [MPa] along the *xx* direction between simulation 1 and 2 for plane ii.

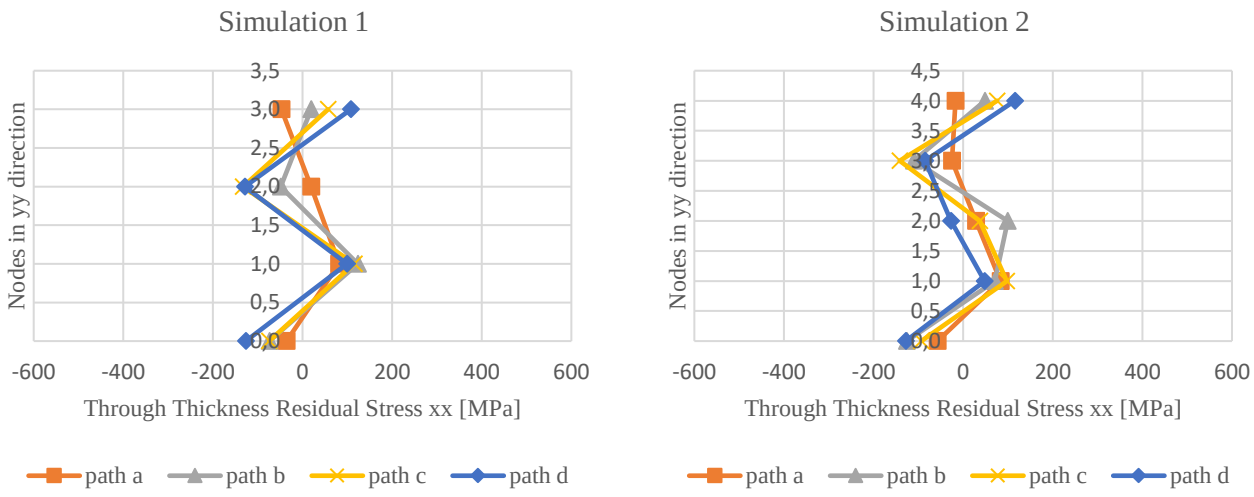

Figure 48 – Comparison of through thickness residual stresses [MPa] along the xx direction between simulation 1 and 2 for plane iii.

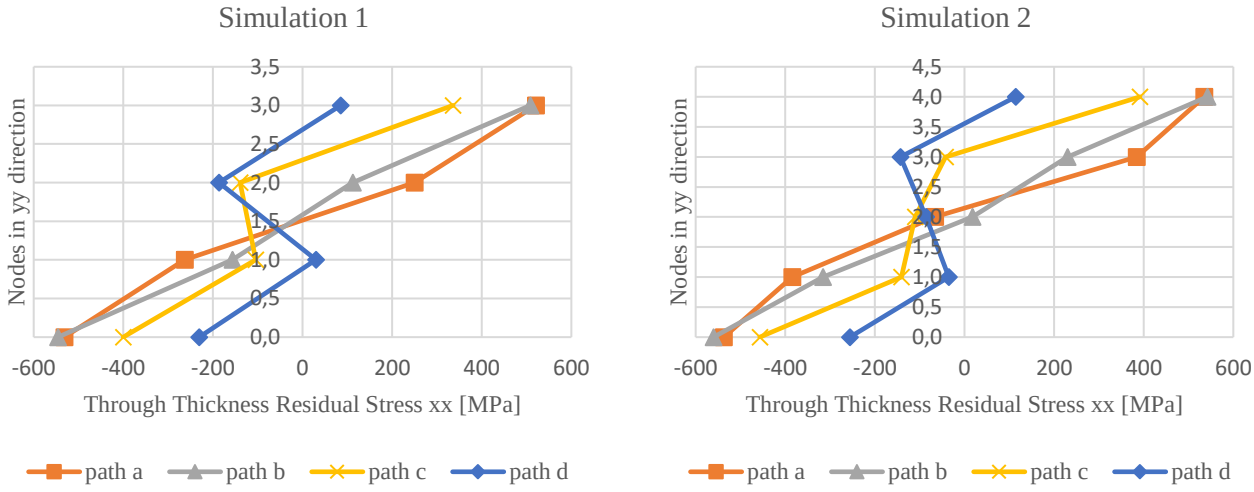

Figure 49 – Comparison of through thickness residual stresses [MPa] along the *xx* direction between simulation 1 and 2 for plane iv.

The results illustrated in Figures 46-49 show that, in spite of refining the mesh along the thickness, the distribution of residual stresses remains identical. For future simulations, three elements along the thickness will be used without compromising results validity.

Furthermore, with regard to the theoretical solution (Figure 18), note that, for intermediate paths (path 2 and 3), the nonlinear residual stress distribution are quite similar. Regarding paths 1 and 4, the results tend to diverge from the theoretical solution due to:

- Stress relief when the profile is cut off once formed, promoting three-dimensional defects such as flare;
- Variation of springback along the profile. According to the theoretical solution, the nonlinear residual stresses distribution results from the contribution of stresses from

plastic bending and the elastic springback. In plane iv, elastic springback reaches higher values (40 to 60% higher) than in other planes.

The number of elements through the thickness also influences the springback behaviour. Increasing the number of elements through the thickness leads to a better distribution of stresses and strains. Figure 50 (see section 3.3.2.) shows the differences in springback for each simulation.

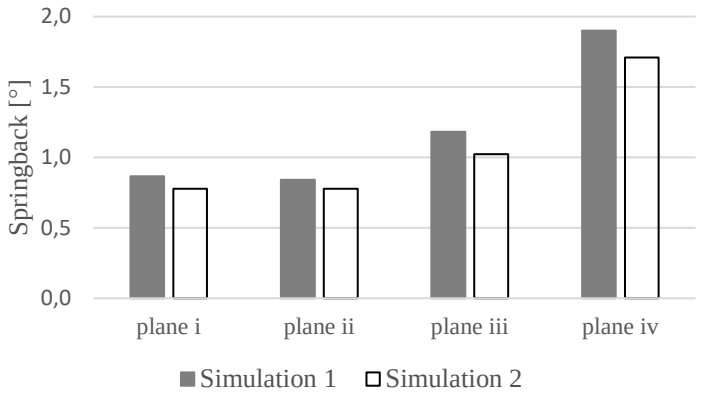

Figure 50 – Comparison of springback between simulations 1 and 2.

Taking in consideration these results, a decrease in springback while increasing the number of elements through the thickness is observed. Increasing the number of elements through the thickness leads to a redistribution of stresses that affects the springback. In spite of that, the variation is considered small, with a maximum difference of 10 % for plane iv.

- **Simulation 1 vs Simulation 3**

As a reminder, simulation 1 has six stations, while simulation 3 has nine stations. Figures 51-52 show the transverse residual stresses along the *xx* direction of each element (see section 3.3.1.). As a side note, only results from path 2 and 3 (plane ii and iii, respectively) were compared, so that the results display the least influence of the cutting process.

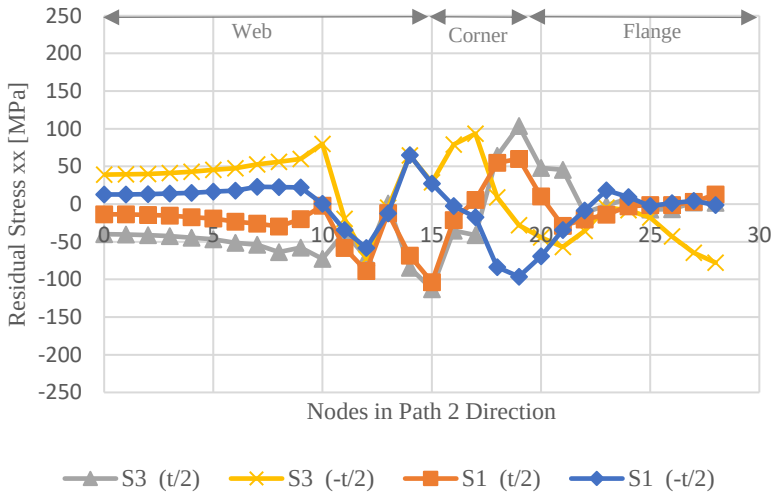

Figure 51 – Comparison of transverse residual stresses [MPa] along the xx direction between simulations 1 and 3 in path 2.

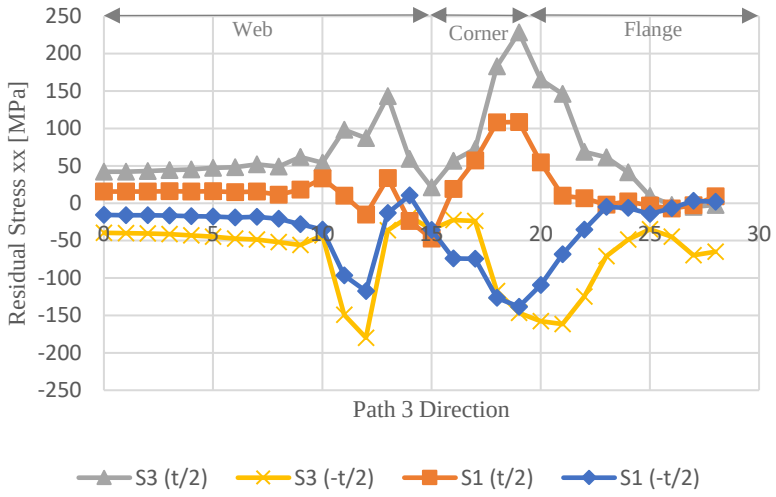

Figure 52 – Comparison of transverse residual stresses [MPa] along the *xx* direction between simulations 1 and 3 in path 3.

The web of the profile (up to node 15) is under compression in the top surface of the profile (t/2) while the bottom surface is under tension (-t/2) for path 2. For path 3, residual stresses display reverse signals to path 2. The bending zone and the flange show far more irregular residual stresses distributions. However, for path 3, the top of the profile is, in almost every node, under tension and the bottom under compression. The key point to observe is the increment of the value of residual stresses in the web when increasing the number of stations from six to nine, for path 2. For path 3, the increase in transverse residual stresses occurs for the web, flange and corner regions. Regarding the through the thickness residual stresses, the distributions of these stresses display similar results to simulation 1 (the results are presented in Appendix 3, Figures 3.1-3.2).

Regarding three-dimensional effects, Figure 53 portrays the edge position of the flange in order to study defects such as flare and waviness. Plots presented in Figures 53-54 display the results in the global coordinate system.

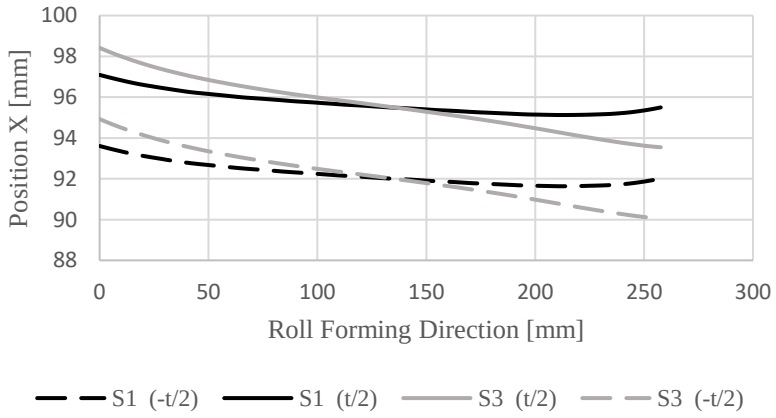

Figure 53 – Edge position of the flange for simulations 1 and 3.

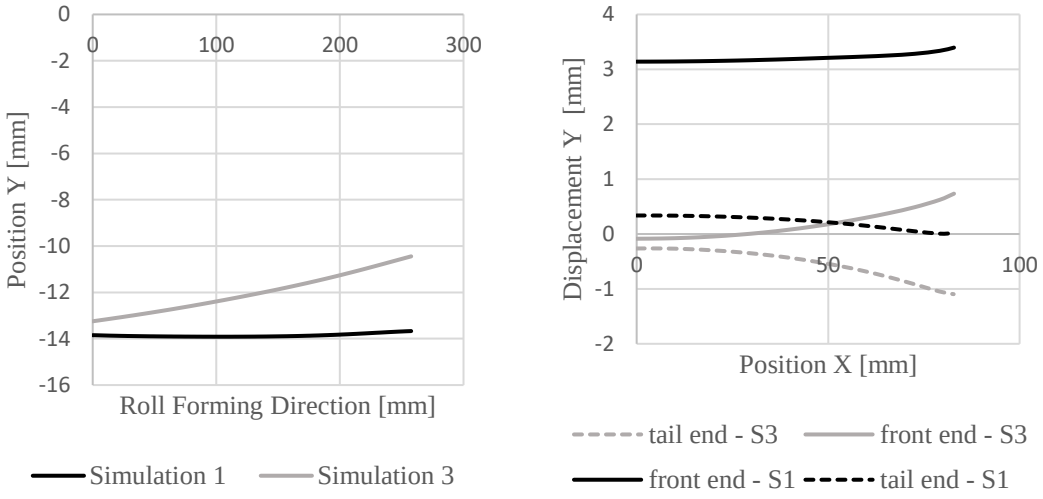

Figure 54 – Longitudinal (left) and cross (right) bow in the bottom surface for simulations 1 and 3.

Most information presented on literature reveals that with fewer passes, forming is more abrupt, which makes the flare larger. In spite of that, these simulations reveal the opposite results. Simulation 1 (with six stations) does not display larger displacement of the edge flange as simulation 3 (with nine stations). These results may have been influenced by the significant increase of springback from simulation 1 to simulation 3 at the extremities of the profile (Figure 55). As mentioned, longitudinal bow is caused by nonuniform transversal distribution of the longitudinal membrane strain, more simply nonuniform longitudinal elongation and shrinkage of the strip. For less number of passes, the amount of transversal bending deformation caused by each pair of rolls can become excessive. In other words, the flange portion and edge portion are forced to rise quickly, which causes larger nonuniformity of the longitudinal membrane strain. However, Figure 54 shows a larger longitudinal bow for simulation 3. Many defects, such as bow, twist, cross-bow, edge waviness can be caused by the roll forming process, imperfections in material, equipment, among others. A good roll design is a key factor to minimize these defects (Halmos 2013). Figure 54 points out that, cross-bow is concave in the tail end and convex in the front end for both simulations (1 and 3). Since roll forming is a progressive process and while in one hand the strip is flat and in the other end the strip is being formed or completely formed, internal residual stresses tend to be formed, promoting these three-dimensional irregularities.

Concerning springback (Figure 55), for plane i and plane iv, the increase in springback is more visible. For planes ii and iii, the changes in springback are almost negligible. However, Badr et al. (2013) investigation revealed that springback decreases when the number of forming stations increases, which means that springback might be influenced by plastic strains in the bend region. Higher plastic strains in the bend regions leads to a decrease in springback. As a matter of fact, simulation 1, in spite of having less forming steps, has a plastic strain in the bend region higher than simulation 3. However, the maximum difference in plastic strain between these two simulations is 0,012 (Figure 56), reason why, springback admits almost the same value for plane ii and plane iii.

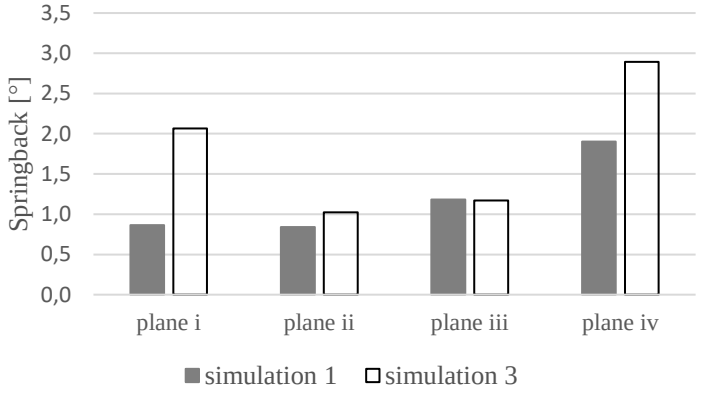

Figure 55 – Comparison of springback between simulations 1 and 3.

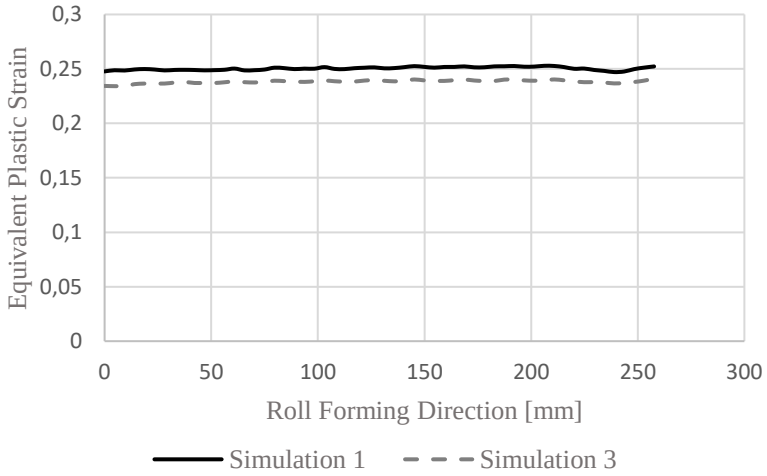

Figure 56 – Comparison of the equivalent plastic strain between simulations 1 and 3 in the bend zone.

As previously stated, according to most literature on this subject, longitudinal peak membrane strains increase with forming angle, since the flange suffers more stretching for higher forming angles - the flange edge travels a higher distance. Figure 57 is in agreement with the literature. For simulation 1, peak longitudinal strain reaches the maximum value of 1,645% while simulation 3 reaches 0,551%.

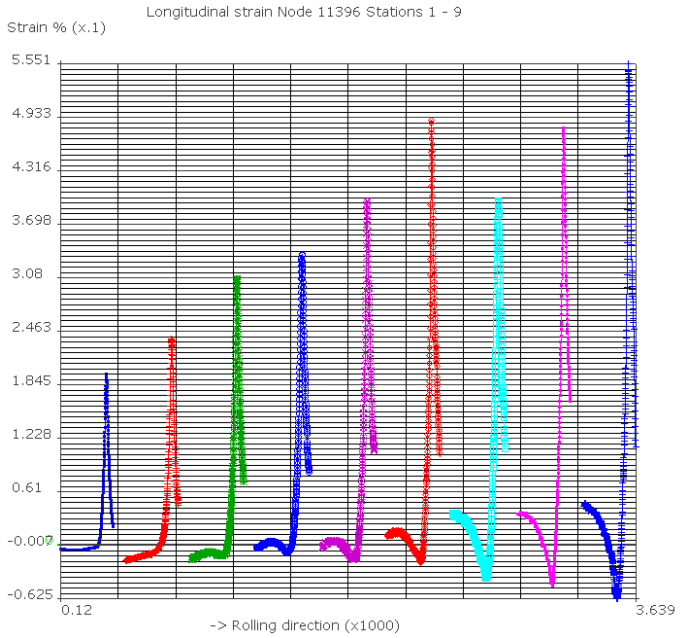

Figure 57 – Longitudinal membrane strain for simulation 3.

- **Simulation 1 vs Simulation 4**

As a reminder, simulation 1 has a distance between stations of 400 mm, while simulation 4 has a distance between stations of 1000 mm. Almost all simulation, including simulation 1, have a strip with 520 mm in length (since the value selected to the coil was 1,3, which means the strip length is 1,3 times the distance between stations). This means that simulation 4 has a strip length larger than simulation 1. Also, for simulation 4, the value introduced in parameter coil was 2 instead of 1,3. This change only occurred, due to the inability of the software to run the model with a coil value of 1,3. For this reason, the comparison between these simulations might not be accurate, since two parameters have changed (for a credible parametric study, only one parameter at a time should be changed).

Increasing the distance between stations means increasing the distance between the first and the last station, allowing a more progressive deformation in the sheet flange, leading to a higher recovery of strains, thus decreasing the permanent plastic strain created at the edge flange. However, Figure 58 shows an increase of 3,3% of the peak longitudinal membrane strain. This value could be explained by the variations of the strip length and the positions in which the longitudinal membrane strains were measured. Nonetheless, Abeyrathna, Rolfe, and Weiss (2017) research showed no significant variation of peak longitudinal membrane strain when increasing the distance between stations.

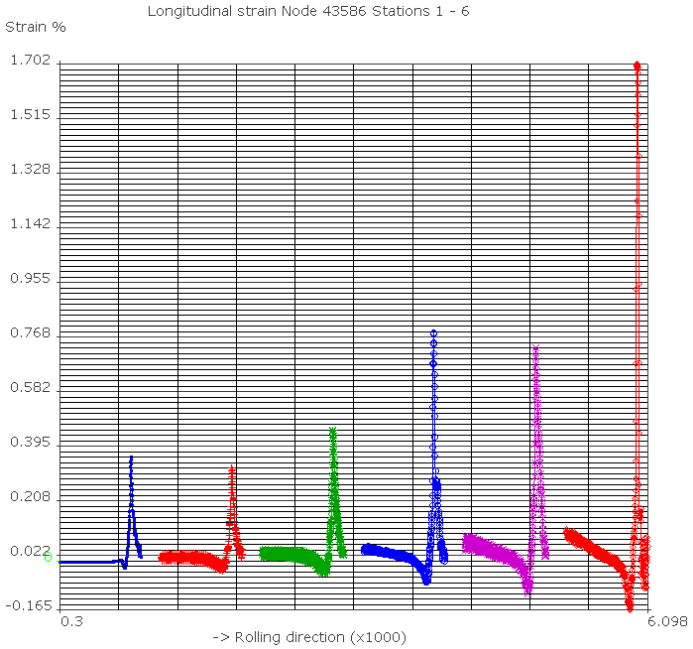

Figure 58 – Longitudinal membrane strain of the node in the middle of the cut off profile length and approximately 1,2 mm away from the edge flange (2nd node from the edge flange and 107th node form the front end of the profile) – Simulation 4.

- **Simulation 1 vs Simulations 5 and 6**

As a reminder, simulation 1 was modelled without friction while simulations 5 and 6 were modelled with friction (with a friction coefficient of 0,15 and 0,2, respectively). Taking friction into consideration means that the rolls are driven. The top and bottom rolls are driven with rolls diameter bottom/top ratio of 1:2. The model presented a speed of 10 rpm for the bottom rolls. The side rolls were non driven.

As far as transverse residual stresses are concerned, the results do not display significant divergences. For simulations 5 and 6, transverse residual stresses are almost coincident and very similar with stresses in simulation 1, either in magnitude and in distribution. Figure 59 proves that similarity for the top surface of path 2. However, these results were also verified for the top and bottom surfaces of all paths (these results are displayed in Appendix 4, Figures 4.1-4.3).

Friction in roll forming processes is responsible for transmitting the driving power from the rotating rolls to the sheet. Bui and Ponthot (2008) findings show no variation in springback for two models (one with a friction coefficient of 0,2 and the other frictionless). However, Figure 60 shows an increase in springback when increasing the friction coefficient, for the present study.

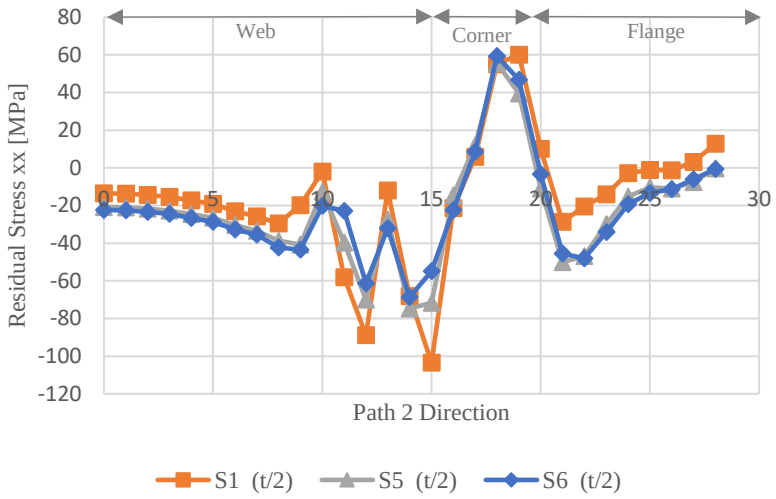

Figure 59 – Comparison of transverse residual stresses [MPa] along the *xx* direction between simulations 1, 5 and 6 in path 2 along the top surface.

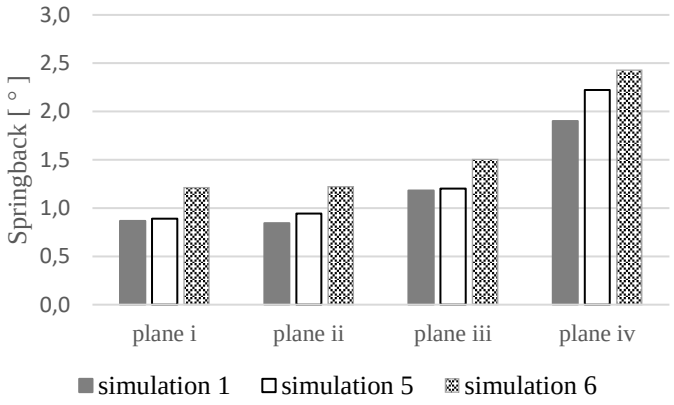

Figure 60 – Comparison of springback between simulations 1, 5 and 6.

- **Simulation 1 vs Simulations 7 and 8**

As a reminder, simulation 1 has a profile with a radius of 8 mm while simulation 7 has 4 mm and simulation 8 has 12 mm (constant thickness of 3,5 mm for all simulations). Regarding through thickness residual stresses along the *xx* direction of each element, the distribution of these stresses and their values did not experience much difference when increasing or decreasing the radius/thickness ratio. Appendix 5, Figures 5.1-5.4 reveal the distributions of the through thickness residual stresses along the *xx* direction of each element for planes ii and iii.

In order to transform a flat strip in to the desired product, the stresses in the bent elements must exceed the yield point of the material. According to literature, the stresses that exceed the yield point lead to the development of permanent deformation and permanent elongation. Roll designers normally prefer bend lines with relatively small radius, since smaller radius creates larger elongation of the outside fibres, which leads to stresses well over the yield point, decreasing

the springback of the profile. For large radius, the stresses will be barely above the yield limit and the elastic strain/permanent strain ratio will be high, which means that the springback will increase when compared to small radius (Halmos 2013). Bui and Ponthot (2008) research also showed that larger bending radius increases springback. For plane iii and plane iv, the results are in agreement with literature on this subject, though for plane i and plane ii, results display a reverse trend (Figure 61).

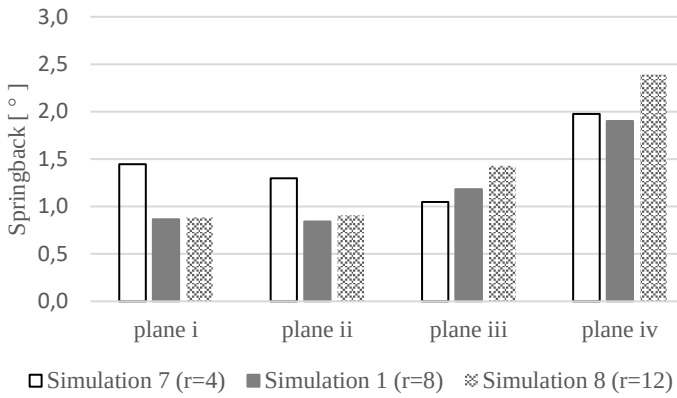

Figure 61 – Comparison of springback between simulations 1, 7 and 8.

- **Simulation 1 vs Simulation 9**

As a reminder, simulation 1 is modelled with S350 steel while simulation 9 uses S460 steel. For the material model of S460 steel, yield strength, ultimate tensile strength and elongation were also introduced in the software and the flow stress curve was estimated by the software code. All the plots that demonstrate these results are presented in Appendix 6, Figures 6.1-6.4. As expected, increasing the strength of the material, leads to higher residual stresses in transversal direction (Appendix 6, Figures 6.1-6.2). Additionally, the distribution of through thickness residual stresses along the *xx* direction of each element displays a different shape of the theoretical solution and simulation 1 (Appendix 6, Figures 6.3-6.4). For most paths, the top surface is under compression while the bottom surface is under tension. These results display some linearity not commonly observed.

Normally, high strength materials flare out at both ends and higher material strengths leads to larger flares (Halmos 2013). Figure 62 is in agreement with the previous statement. End flare is caused by the release of internal stresses (theses stresses are balanced while the section is continuous, but when the piece suffers the cut, these stresses become unbalanced), and for higher strength material, these stresses are higher as well.

As mentioned, some literature reveals that materials with higher yield strength normally have smaller longitudinal membrane strain (longitudinal peak membrane strain measured for simulation 9 was 0,9974%), as well as higher deformation lengths. However, high strength steels have larger springback, since the elastic limit of the material increases, which means higher elastic recovery. Figure 63 reveals that the results are in agreement with the previous assumptions. It can also be concluded that springback fluctuates approximately between 0,9 ° and 3 °.

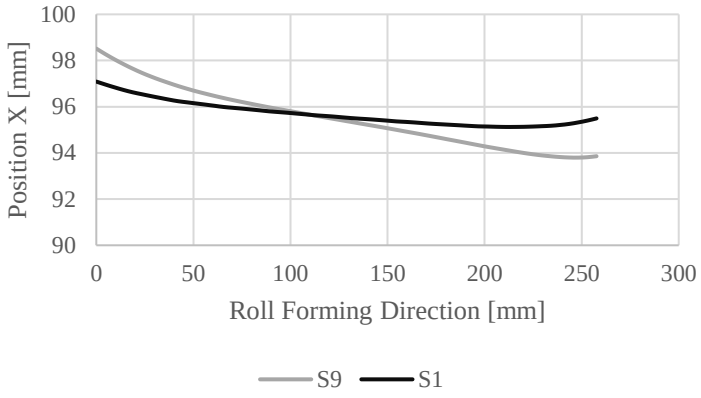

Figure 62 – Edge position of the flange for simulations 1 and 9 in the top surface.

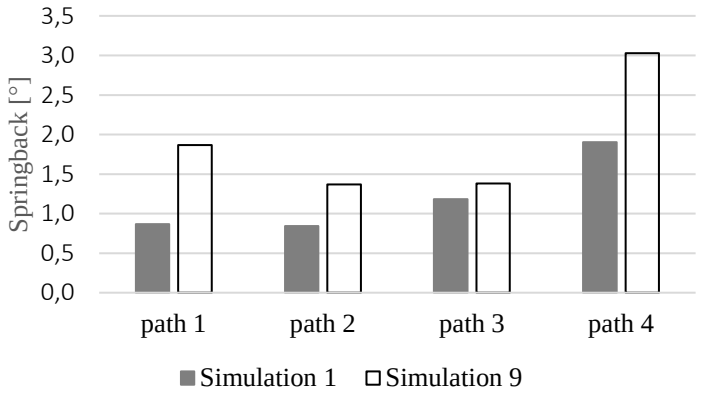

Figure 63 – Comparison of springback between simulations 1 and 9.

3.5. Fatigue analysis of the U-channel profile

Roll forming processes introduce residual stresses in the material. These residual stresses when combined with service loading can change the stress range to be considered in the fatigue analysis. For this reason, an external cyclic mechanical load was applied to the cold roll formed profile in order to determine the resulting stress range and the critical area where fatigue cracks nucleation tends to occur. The finite element analysis was developed using MSC Marc/Mentat software. In order to apply cyclic loads, the model needed some alterations (due to the modification of boundary conditions, external loads, initial conditions, etc.). For that, MSC Marc/Mentat was also used.

Rail sections must be designed to withstand the passage of shuttles (empty or fully loaded). Table 8 reveals typical shuttle´s weights with and without the pallet, as well as the resulting load in kN. This information was supplied by some industrial partners of the project.

Table 8 – Information given by industrial partners of FASTCOLD project about the shuttles and pallets typical masses.

Mass of the shuttle [kg]	**Mass of the pallet [kg]**	**Number of Wheels**	**Load for a wheel without pallet [kN]**	**Load for a wheel with pallet [kN]**
300	1200	8	0,375	1,875 ≈ 2

The load for the U-channel profile was applied in 9 nodes (the centre node is the 39th node counting from the front end of the profile, as it is shown in Figure 64), approximately in the centre of the flange and in the middle of the profile length. The increment used as a starting point for the fatigue analysis (1185) was the one right before the end cut of the profile, reason why the tail end of the profile still had the last station rolls in contact with the material. For the fatigue analysis, a mesh without discontinuities was selected (in other words, the mesh used was of the profile without the end cuts). However, when applying the boundary conditions to the imported mesh, all the elements that were in contact with the rolls were “deactivated”. This way, more than half of the strip could be analysed for the fatigue analysis and the influence of the free cut was disregarded. In other words, this increment was used so that more than half of the strip could be analysed after cyclic loads, ensuring that the free cut of the profile did not influence the results. Regarding boundary conditions, *x*-direction boundary condition due to the symmetry of the U-channel profile were applied in the symmetry line (similar to the boundary conditions used to perform the simulations in the parametric study, Figure 30). Moreover, the nodes in the interface between the “deactivated elements” and the rest of the strip were restrained in the y and z

directions, only in the web zone. Boundary conditions were also applied in the front end of the profile and were not applied in the corner regions or in the flange.

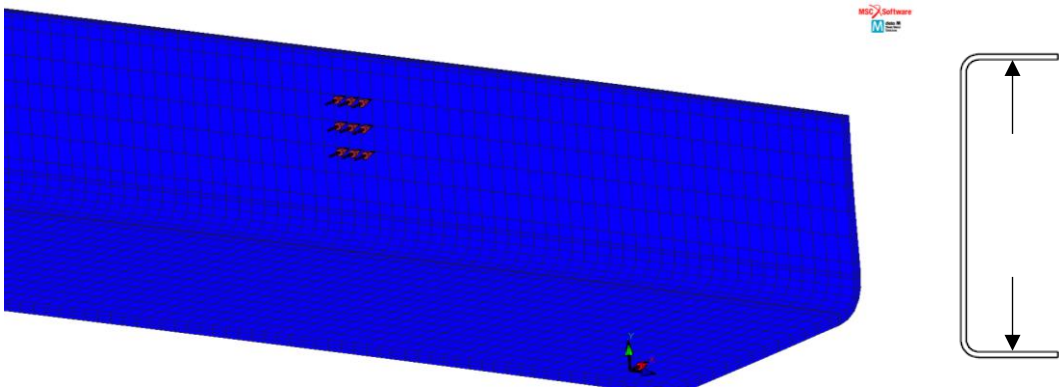

Figure 64 – External cyclic mechanical load in both flanges of the profile.

When a structure is under the application of a repeated load, it can lead to the nucleation and propagation of a crack and the longer the crack, the higher the stress concentration induced by it. This implies that the rate of crack propagation increases with time as the structure strengths decreases, which can lead to its failure (Broek 1982). Cracks tend to propagate in the perpendicular direction to the maximum principal stress. Nevertheless, the majority of mechanical and structural components are under a multiaxial stress state. For multiaxial fatigue analysis, it is crucial to understand the field of stresses and strains in the component, specially the magnitudes and directions of principal stresses, the maximum shearing stress, the maximum normal principal strain and the maximum shearing strain present in any location and orientation of the structure to allow the identification and orientation of the critical point (Ellyn 1997).

For cold roll formed profiles that are under cyclic loading, maximum principal values of stress can change its direction a variety of times, since it is a problem of multiaxial stresses and may involve cyclic transient loadings due to the rolling moving loads, e.g. moving shuttles on a rail. For each time increment and for each node, the software provides the magnitude and direction of the maximum principal stress, which normally changes with time increments. For this reason and in order to simplify the model, the stresses that will be studied aiming the fatigue analysis are the stresses in the *xx* direction of the element coordinate system since the direction of these stresses are known for each position of the element and for each time increment. However, cyclic loading in cold form products for shelter applications involves multiaxial fatigue and transient loads.

The cyclic load (two cycles) was applied and its shape is governed by Eq. (3.2).

$$F(t) = a * \sin\left(t - \frac{\pi}{2}\right) + a \tag{3.2}$$

Where:

- a is a constant that determines the maximum value of the applied load.

Three different loads were applied in order to study the material behaviour to load changes. Since the total load is the sum of the loads applied in each of the nine nodes, for a total load of 2 kN, $a = 111\ N$. Then, loads of 4,5 kN and 9 kN were also simulated, with $a = 250\ N$ and $a =$

500 *N*, respectively. Figure 65 illustrates the load function for a maximum amplitude intensity of 2 kN.

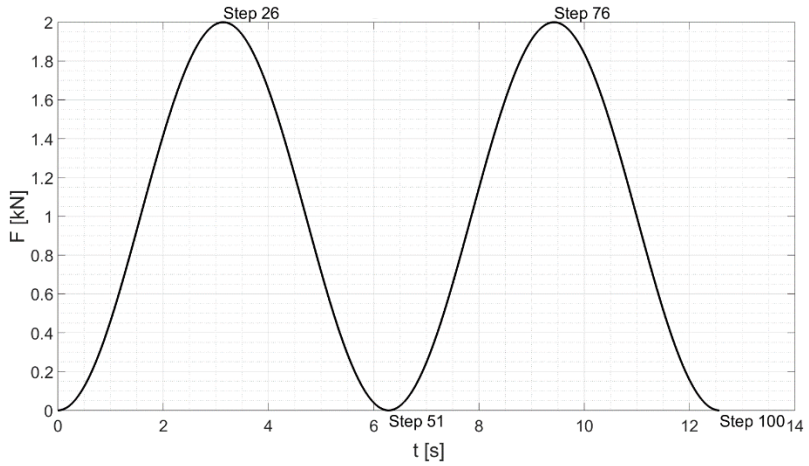

Figure 65 – Cyclic load with a maximum range of 2 kN simulated in the U-channel section.

Firstly, critical areas in which a crack might be initiated were identified. The stress distribution field showed that the corner region near the area where the load was applied suffered significant changes in stresses with the cyclic load, and when the maximum load amplitude was achieved, the corner displayed the highest values of stress, reason why bending regions were established as the critical areas. (see Figure 66).

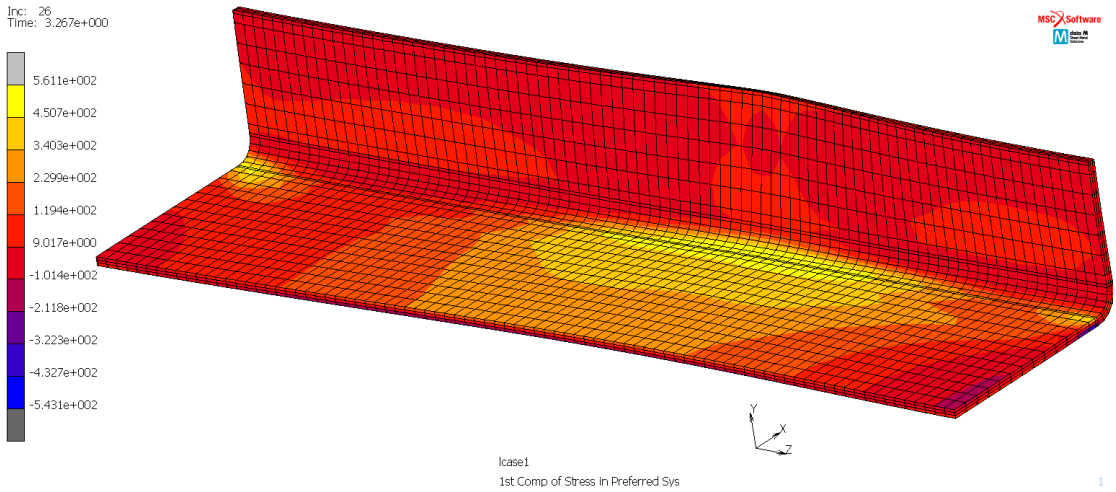

Figure 66 – Stresses [MPa] along the *xx* direction of the element coordinate system for step 26 (see Figure 65) and for a maximum load range of 9 kN.

Secondly, four paths were defined (Figure 67) in the corner region and stresses were measured both in the inner and outer corner surfaces in order to report the changes in magnitude and/or signal of these stresses. Stresses were analysed at the maximum load amplitude (steps 26 and 76 of the numerical simulation) and in the absence of load (steps 51 and 100 of the numerical simulation), Figure 65.

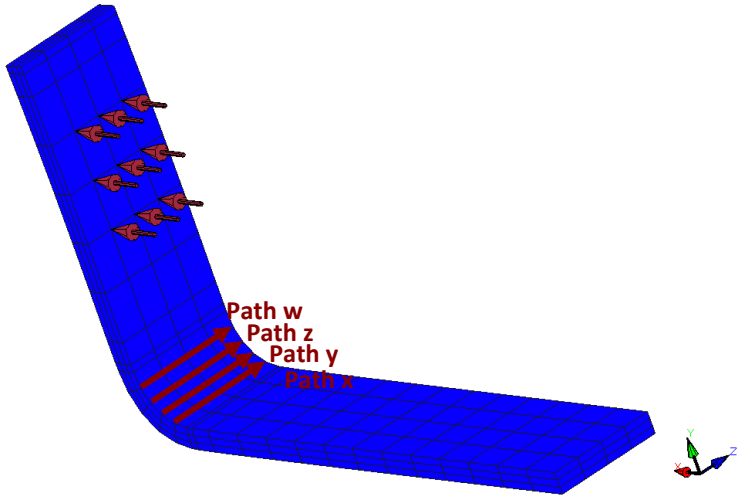

Figure 67 – Paths where stresses were measured.

As mentioned, the maximum cyclic loads applied to the flange of the profile were 2 kN, 4,5 kN and 9 kN and these loads were applied in 9 nodes of the structure. The element size in the flange is approximately 4,69 x 7,94 mm, therefore the load was applied in a total area of 148,95 mm^2. Even though the stresses applied are under the plastic limit of the material, that does not imply the safety of the product because stress concentrations can lead to local stresses and respective strains in the plastic domain. Analysing the results, dividing them into steps and comparing them with the initial state of the profile (the U-channel profile presented stresses and strains that derived from the roll forming process), it was concluded that:

- The inner corner surface was under tension before the application of the external load. This was verified for every path except path x. As expected, the bending process tends to induce a compressive state in the inner corner surfaces and a tensile state in the outer corner. However, due to the elastic return of the material, these stress states tend to be reversed, leaving the inner corner under tension and the outer corner surfaces under compression.

- For steps 26 and 76 and for the inner corner, path x and path y became under tension, for a maximum load amplitude of 2 kN. The magnitude of the stresses increased in comparison with the initial state. However, paths z and w present compressive stresses. For higher loads, all paths were under tensile stresses. For instance, for 4,5 kN only path w displays compressive stresses and for 9 kN all paths are under tension. Higher maximum loads intensify the initial stress state, since it leads to an increase of positive stresses. Compressive stresses do not jeopardize the fatigue resistance of materials. Furthermore, steps 26 and 76 present the same values of stresses. However, stresses after the cyclic loading differ from stresses after the rolling process and before the cyclic loading.

- For steps 26 and 76 and for the outer corner surfaces and for the maximum load of 2 kN, paths x and y are under compression, nonetheless for paths z and w, stresses present a positive value. For higher maximum loads, all paths are under compression and the

magnitude of the stresses are more negative than the initial state. In the second cycle, these steps also show similar values of stresses for the outer corner.

- For steps 51 and 100, all applied loads led to a compressive state of the inner corner. After being under tension when the load amplitude applied was maximum, the release of the load leaves the inner corner surfaces under compression. Path w is the only path that does not follow this tendency (Figure 68). For a magnitude of 9 kN, path w is under tension but with smaller values of stress than the stresses of steps 26 and 56.

- For steps 51 and 100 and for the outer corner, stresses tend to become positive again. However, some paths are still under compression, but with less negative values than the previous state.

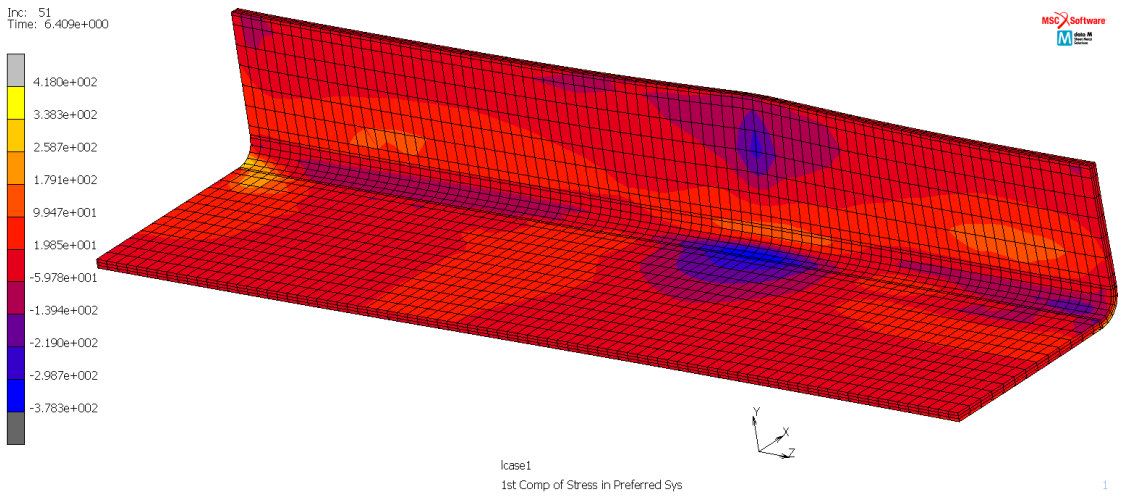

Figure 68 – Stresses [MPa] along the *xx* direction of the element coordinate system for step 51 (see Figure 65) and for a maximum load of 9 kN.

To summarize, the initial state presented tensile stresses in the inner corner and compressive stresses in the outer corner. When the load was being applied, the inner corner presented tensile stresses with higher magnitude, which decreases the fatigue resistance of the material. However, the outer corner surfaces became under compression, which does not represent any harm to fatigue life. When the profile was released of the external load, the inner corner change back to a compressive state while the outer corner surfaces became under tension. This was verified for both cycles. These results are all presented in Appendix 7, Tables 7.1-7.4. Also, after the application of the mechanical load, the corner presented stresses that differ from the ones in the initial state, which proves the existence of an elastoplastic effect of the material, after the first cycle of the external load. The return to the original state should only be observed for a fully elastic behaviour.

Moreover, analysing the results in Appendix 7, Tables 7.1-7.4, path x represents the critical path, specifically the 4th node counting from the beginning of the path since it experiences higher values of stress for steps 26 and 76. For this reason, fatigue life of the profile was estimated taking into account the critical area, particularly this node where a crack is more likely to be initiated. Figures 69-71 display the resulting stress time histories due the application of three different cyclic loads, from which the fatigue actions (stress range and mean stress) can be evaluated.

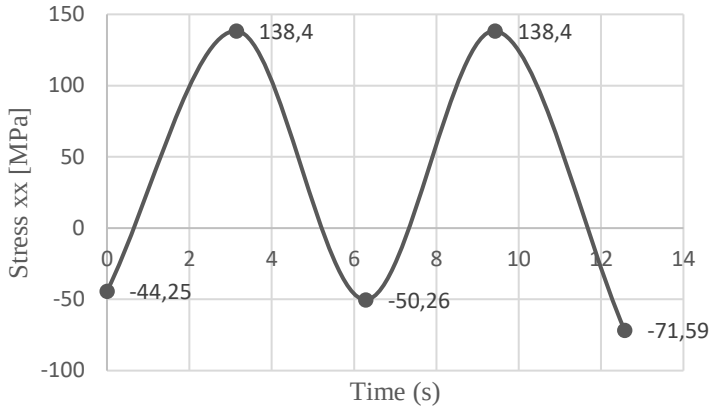

Figure 69 – Stresses in the critical node for a maximum mechanical cyclic load of 2 kN.

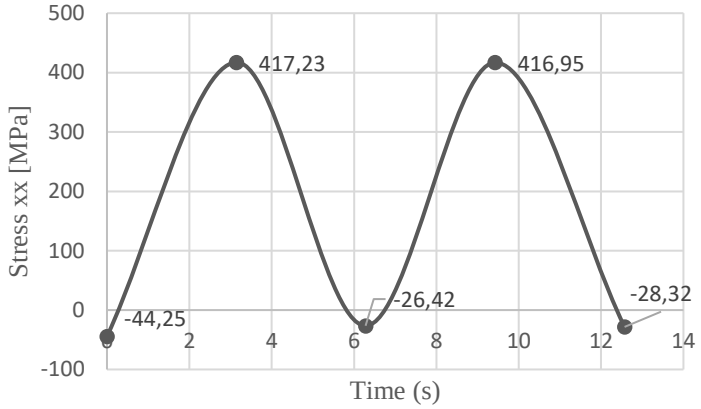

Figure 70 – Stresses in the critical node for a maximum mechanical cyclic load of 4,5 kN.

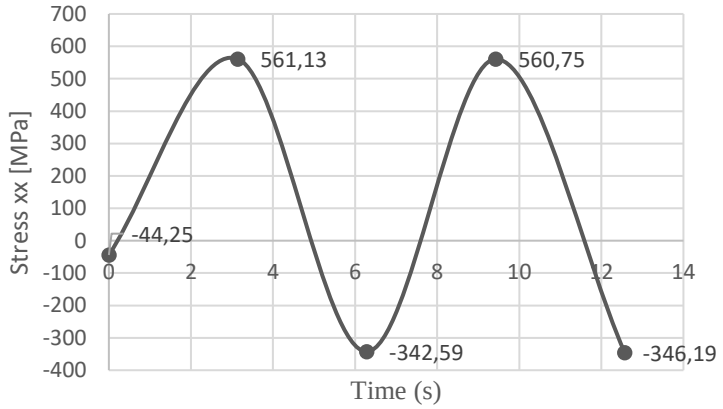

Figure 71 – Stresses in the critical node for a maximum mechanical cyclic load of 9 kN.

Note that, in the first cycle of the applied load, a stress relaxation from the initial state (after roll forming) is visible, especially for higher loads (9 kN).

Stress-based approaches to estimate fatigue life are normally applicable to high cycle fatigue regime, where the strains are essentially elastic, while the strain-based approaches are mostly used for thermal and low cycle fatigue. However, the most common application of strain-based approaches are in fatigue of notched members (Stephens et al. 2001). Mean stresses are of crucial importance to stress-based approaches, since tensile mean stresses lead to a reduction of the fatigue strength coefficient and compressive mean stresses have the opposite effect, in other words, tensile mean stresses are detrimental and compressive mean stresses are beneficial to fatigue life (Figure 72).

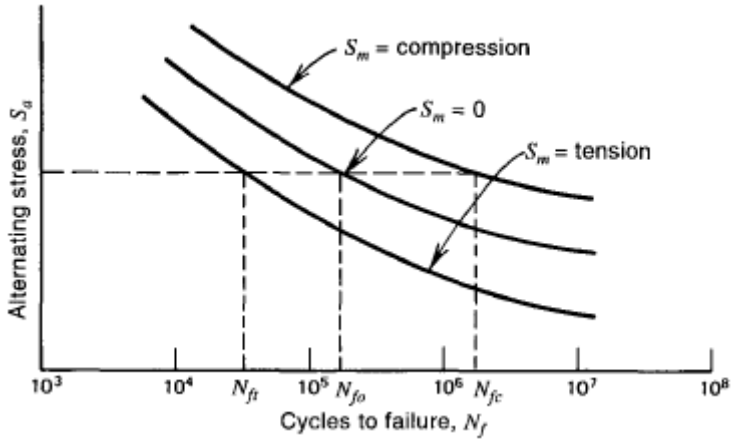

Figure 72 – Effect of mean stress, S_m on fatigue life (Stephens et al. 2001).

After extracting and analysing the results of the stress-strain curves of the material for a maximum load of 2 kN and 9 kN, for the second cycle of each simulation, the material presents an elastic behaviour (no hysteresis stress-strain loops were verified) The same behaviour was assumed for the load of 4,5 kN. These results are reported in Appendix 8, Figures 8.1-8.4. For this reason, local stress-based approaches were used (S-N curves). Therefore, for an estimative of fatigue life of the profile, only stresses from steps 76 and 100, respectively, were considered. Taking into consideration Figures 69-71, the expression to determine fatigue life that includes the mean stress effect, Eq. (2.9) and Table 2, regarding cyclic elastoplastic fatigue properties of S355 mild steel; ($\sigma_f' = 952{,}2\ MPa$ and $b = -0{,}089$), σ_m, $\Delta\sigma$ and N_f were calculated (Table 9).

Table 9 – Estimated number of cycles for three different cyclic loads using the local S-N based approach.

Load	$\boldsymbol{\sigma_{max}}$	$\boldsymbol{\sigma_{min}}$	$\boldsymbol{\sigma_m}$	$\boldsymbol{\Delta\sigma}$	$\boldsymbol{N_f}$
2 kN	138,40	-71,59	33,41	209,99	1,9E+10
4,5 kN	416,95	-28,32	194,32	445,27	4,7E+05
9 kN	560,75	-346,19	107,28	906,94	5,4E+02

Note that σ_f' and b used to determine the number of cycles until failure are the ones obtained by an experimental work for S355 mild steel (Jesus et al. 2012). Due to the lack of information about S350GD, particularly about fatigue constants, the values from S355 were used in this analysis.

Figure 73 reveals the approximate linearity in log-log scales of results between the load applied to the profile and the number of cycles until failure. Nonetheless, the graph only has three points. To confirm this assumption, more loads should be applied in order to confirm the trend.

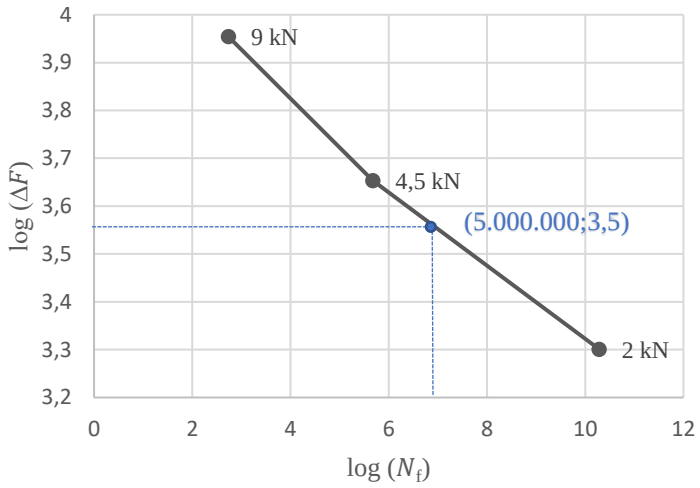

Figure 73 – Number of cycles for maximum loads of 2 kN, 4,5 kN and 9 kN in a logarithmic scale for a U-channel profile.

According to EN 1993-1-9 (2005), for $m = 3$ (slope of fatigue strength curve), the number of cycles for which the structure is considered to have an infinite life is 5 million, as it is shown in fatigue strength curves for direct stress ranges proposed in Eurocode 3 (see Figure 25). Assuming the same number of cycles for an infinite life of this structure, it is possible to determine the maximum load that can be applied without compromising the structure (preventing fatigue damage). Using Figure 73 (blue lines), the maximum load that can be applied for an infinite life of the structure is approximately 3,5 kN.

For a cyclic load of 9 kN the number of cycles obtained was approximately 540, which means, for this load, that is a low cycle fatigue problem, and the local S-N approach might not give a valid estimation of fatigue life of the component. However, the stress-strain curves reveal an elastic and reversible deformation of the material, as previously stated (see Appendix 8, Figures 8.1-8.4). In spite of this results, an isotropic hardening model was used, instead of a kinematic hardening model. Hardening rules establish the conditions for a new plastic flow after the plastic state of the material has been reached. For an isotropic hardening, the subsequent yield surface originated due to an increment in plastic deformation is a uniform expansion of the previous yield surface. This model principal advantage is its simplicity, although some real aspects of material deformations cannot be reproduced with this model, for instance, the Bauschinger effect (Figure 74). For a kinematic hardening model, the yield surface maintains its shape but translates in space. This model appeared to better reproduce the Bauschinger effect, present in metallic materials subjected to cyclic loadings. Bauschinger effect reveals the dependence of yield strength with the direction of loading (Natal Jorge and Dinis 2004). In other words, when a material is being loaded

uniaxially in one direction (e.g. in tension) into the plastic regime, unloaded to zero and then reloaded in reverse direction (e. g. compression), it might yield during the reloading, at a stress level lower than if the reloading was carried out in the original direction – direction dependent and asymmetrical yield behaviour (Yan 1998).

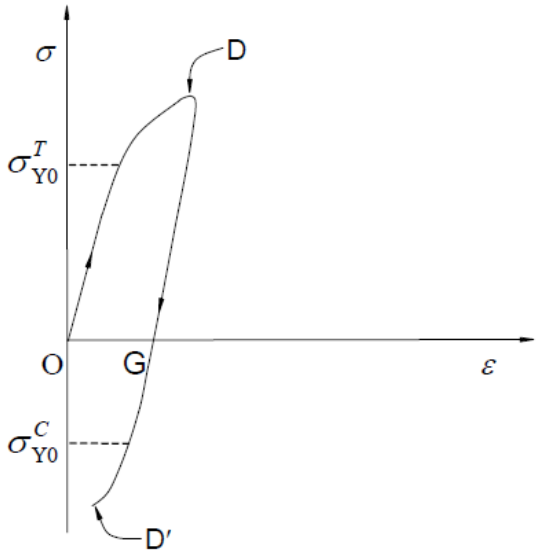

Figure 74 – Bauschinger effect, where σ_{Y0}^{T} is the tensile yield stress and σ_{Y0}^{C} is the compressive yield stress (Yan 1998).

In order to verify the validity of the results, the best approach is to simulate this model using a kinematic hardening rule and draw the stress-strains diagrams. If the Bauschinger effect is noticeable (hysteresis loops verified), then it should be used a strain-based approach to estimate fatigue life of the component.

As mentioned, the previous results were obtained applying the load directly in the profile obtained by the roll forming process (first method), which means that the load was applied in a model with initial conditions of stresses and strains. However, the validity of a second method (superposition method) was relevant to study. To achieve that, a model with an imported mesh of simulation 1 (reference) was created. Note that, this model does not contain initial stresses or strains, but presents the mesh with the final shape of the roll forming process. After that, the same cyclic loads that were used in the previous method were applied to this second model. The goal was to sum the stresses obtained with this second model with the stresses from simulation 1 (referred to as initial state of the profile) and compare the results with the stresses obtained with the first method. After analysing the results, it was concluded that this second method was not viable. This method is sometimes used in engineering problems, due to its simplicity, although, in this case, it is not applicable. There are two distinguished fields of stress (the first one resulting from cold roll forming processes and the second one resulting only from the application of a cyclic load) and the superposition of these two fields is not linear, since the model is elastoplastic. The comparison of results between the two methods was performed using a maximum load of 9 kN and for some paths, the differences in the results could not be neglected (some paths have a relative error of approximately 50%). However, paths y and z present errors between only 1 and 13%. This data is presented in Appendix 7, Table 7.5.

To summarize, the models presented in this chapter contain some limitations, which might influence the validity of the results. For this reason, experimental works are of extreme importance to validate the numerical findings. This being said, for the Z-section profile and for current and future investigations within the FASTCOLD project, some recommendations are presented next:

- To better understand the effects of the free cut of the profile, a simulation with higher strip length should be performed to determine the extent of the influence of the free cut;
- In order to reduce or to optimize the CPU time, a parametric study with different meshes should be performed;
- To apply the cyclic loads, the profile should not have been split symmetrically, because, with this condition, the load was applied in both flanges. However, this symmetric load might not have influenced the stresses presented in the bend zone, because they are sufficiently apart from each other;
- Regarding the hardening rule for these simulations, since the final goal is to study the influence of cyclic loads, the hardening rule should be kinematic instead of isotropic.

Chapter 4

Numerical simulation of a Z-section profile

Similar to Chapter 3, the following chapter presents the simulation model generated for a Z-section profile (rail section profile), as well as the material model and the results and conclusions of this simulation. The main objective of this chapter is to describe the effects of roll forming process on material behaviour, compare it with the results obtained from the parametric study of the U-channel profile and explain the deviations that may occur. Additionally, this section includes the results of an experimental tensile test that was used to determine the stress-strain curve of the material. This curve is compared with the curves estimated by the software, used in Chapter 3. Finally, this chapter also incorporates a study on the influence of mechanical cyclic loads on the residual stresses of the profile, as well as an estimative of the fatigue life of Z-section profile components subjected to these loads.

4.1. Model definition

4.1.1. Modelling concepts

For the Z-section profile, the forming rolls were also modelled as rigid bodies while the strip was modelled as a deformable one. For this simulation, friction was disregarded since there was no available information in FASTCOLD project consortium about this parameter (friction coefficients are difficult to determine experimentally).

4.1.2. Geometry and flower

The roll design was developed in COPRA® RF and the simulation models were prepared automatically by the COPRA®FEA RF package from the roll design developed in COPRA® RF. The distance between stations is 400 mm and the strip length is 520 mm. The dimensions of the Z-section profile are illustrated in Figure 75. The forming line has thirteen stations (Figure 76) and the bending sequence is presented in Appendix 9, Figure 9.1. The flower diagram is shown in Figure 77. All the rolls for the simulation of the Z-section profile is presented in Appendix 1, Figures 1.16-1.28.

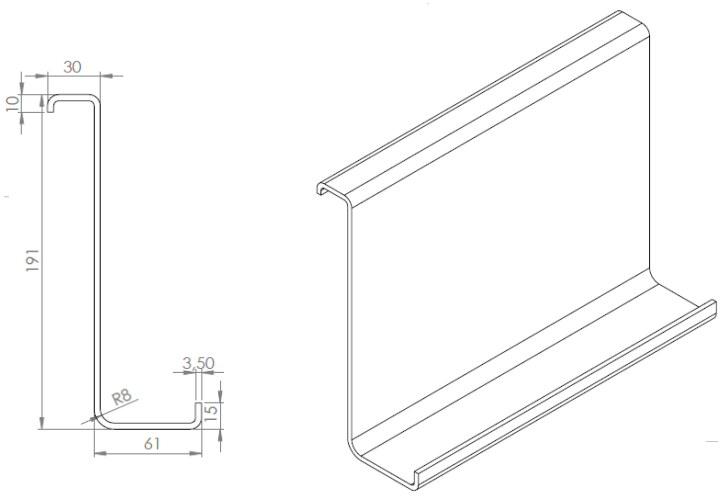

Figure 75 – Dimensions [mm] of the Z-section profile (r=3mm for all inside radii not shown explicitly).

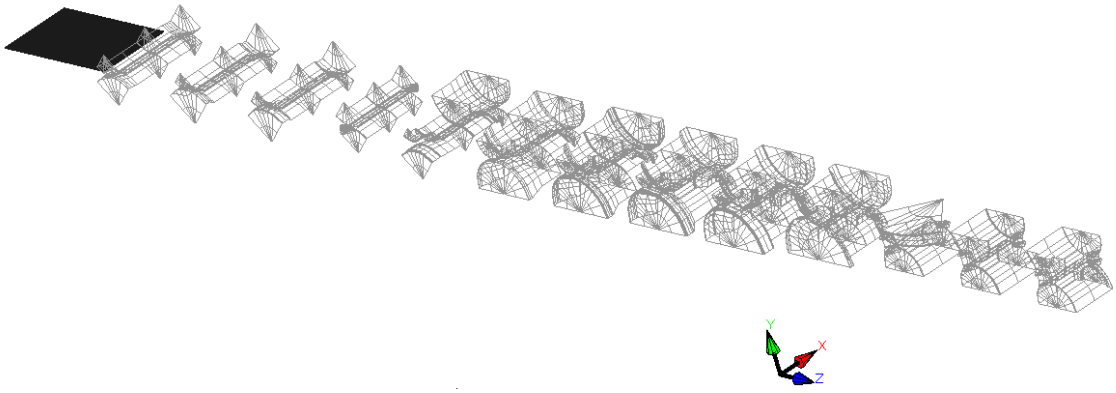

Figure 76 – Stations and respective rolls for the simulation of the Z-section profile.

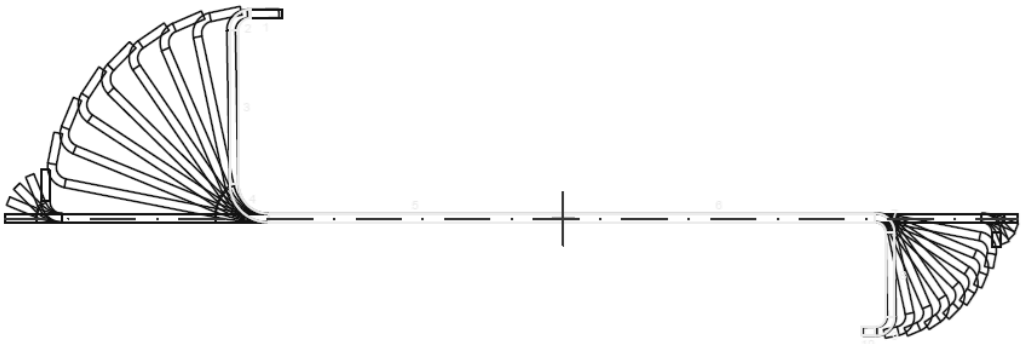

Figure 77 – Flower diagram of the Z-section profile.

Similar to the U-channel profile, the standard global coordinate system used was:

- *x* for the horizontal direction perpendicular to the sheet rolling direction;
- *y* for the thickness direction in the flat sheet (vertical);
- *z* for the sheet travel direction (roll forming direction).

4.1.3. Boundary conditions

On the tail end of the profile, boundary conditions (Figure 78) were used to restrain the displacements in the *x* and *y*-directions of the last three nodes in the middle of the profile, for the same reason they were used in U-channel profile (so that the strip would not experience rigid body motion). All the nodes in the front and tail end were also restricted along the z-direction to simulate the continuous existence of the strip (Figure 79).

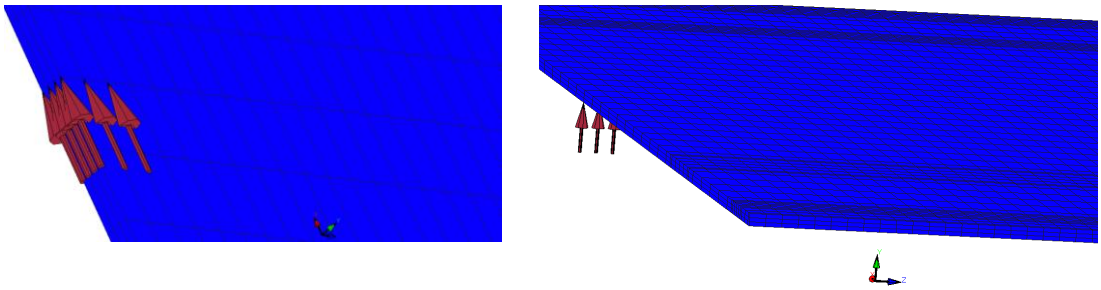

Figure 78 – *X* and *y*-directions boundary conditions – restriction of three nodes in the middle of the tail end of the profile.

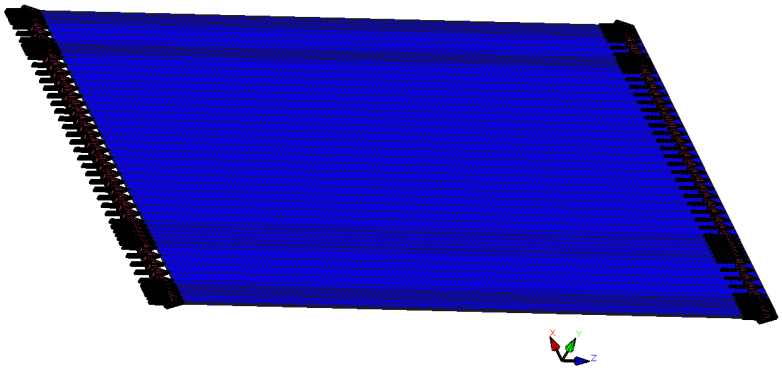

Figure 79 – Boundary condition to simulate the continuous existence of the strip (nodes in the extremities of the strip restrained along *z*-direction).

Finally, boundary conditions to prevent the strip from moving freely in space (preventing a rigid body motion) after the cutting process were also applied, as it is shown is Figure 80.

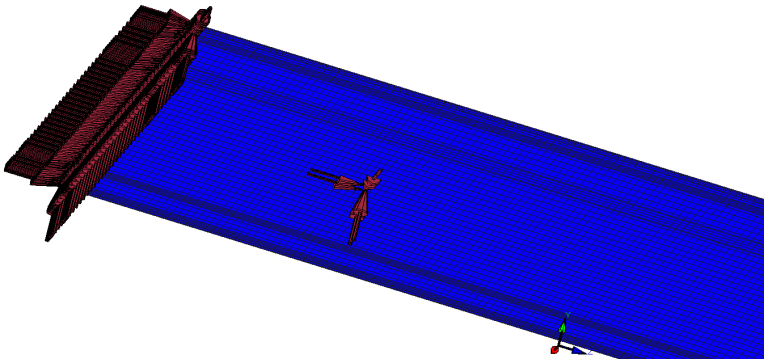

Figure 80 – Boundary conditions due to the free cut process.

4.1.4. Element type

The element type chosen was element type 7, the same element type already chosen for all the simulations of the U-channel profile.

4.1.5. Mesh definition

For subdivisions straight entities, i. e. the number of subdivisions in straight entities of the section for FEA calculation was equal to 2,8. The value introduced for the number of subdivisions for arc entities was 1,8 and the number of subdivisions in the rolling directions was 1,5. The ideal mesh would probably be the same used in the U-channel profile. However, taking into account the increase in the number of stations and the geometry of the profile (making impossible to split it symmetrically and simulate only half of the profile, like in the U-channel profile), the CPU time usage estimated was 15 days. For this reason, a less refined mesh (29016 elements) was used, since, logistically speaking, analysing the results given the time provided would be unfeasible. To conclude, the results may display possible divergences from the reality due to this new mesh. However these results will be compared with the experimental data that will be executed latter in FASTCOLD project, and a parametric study involving different meshes may be performed if necessary. Three elements were also used, along the thickness direction. Figure 81 illustrates the final mesh used for this profile.

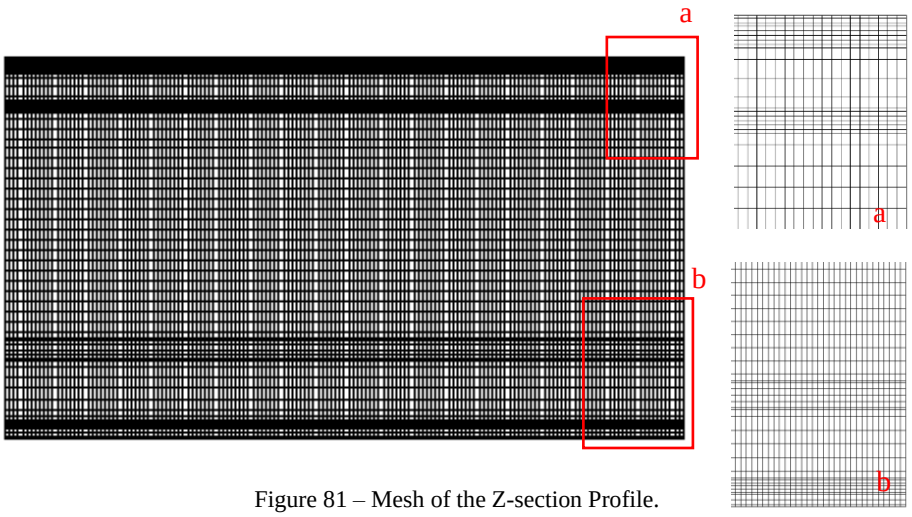

Figure 81 – Mesh of the Z-section Profile.

4.1.6. Material model

Engineering stress-strain curves can be obtained by performing a tensile test on the material. Engineering stresses and strains (Eq.(4.1) and Eq.(4.2)) only consider the specimens' initial size.

$$\sigma_{eng} = \frac{F}{A_0} \tag{4.1}$$

$$\varepsilon_{eng} = \frac{l - l_0}{l_0} \tag{4.2}$$

Where:

- σ_{eng} is the engineering stress;
- ε_{eng} is the engineering strain;
- F is the applied load;
- A_0 is the initial area of the specimen´s cross section;
- l_0 is the initial length of the specimen's gauge;
- l is the current length of the specimen's gauge.

The total strain, ε_t can be considered the sum of two components: the plastic strain, ε_p and the elastic strain, ε_e as it is shown in Eq. (4.3):

$$\varepsilon_t = \varepsilon_p + \varepsilon_e \tag{4.3}$$

The elastic strain depends on the current stress and it is given by Eq. (4.4):

$$\varepsilon_e = \frac{\sigma_{true}}{E} \tag{4.4}$$

Where:

- σ_{true} is the true stress;
- E is the Young´s modulus.

The parameters presented in Swift´s law are true stresses, σ_{true} and strains, ε_{true}. The relationship between these parameters and engineering stresses and strains are given by Eq. (4.5) and Eq. (4.6), respectively.

$$\sigma_{true} = \sigma_{eng}(1 + \varepsilon_{eng}) \tag{4.5}$$

$$\varepsilon_{true} = ln(1 + \varepsilon_{eng}) \tag{4.6}$$

In order to determine the experimental engineering stress-strain curve of the material, tensile tests on two specimens of S350GD steel (Figure 82) with an initial rectangular cross section of 42 mm^2 and 150 mm of total length and 50 mm gauge length were performed. Two samples of S350GD

steel were tested in the *Laboratório de Ensaios Tecnológicos* (LET) - T_Z_2_1 and T_Z_2_2 specimens. As mentioned before, the specimens used were not standardized.

A servo-hydraulic testing machine with a load cell with 100 kN of capacity (Figure 83) was used for the tensile test. The clip gauge used had an initial length of 50 mm. Tests were performed using displacement control.

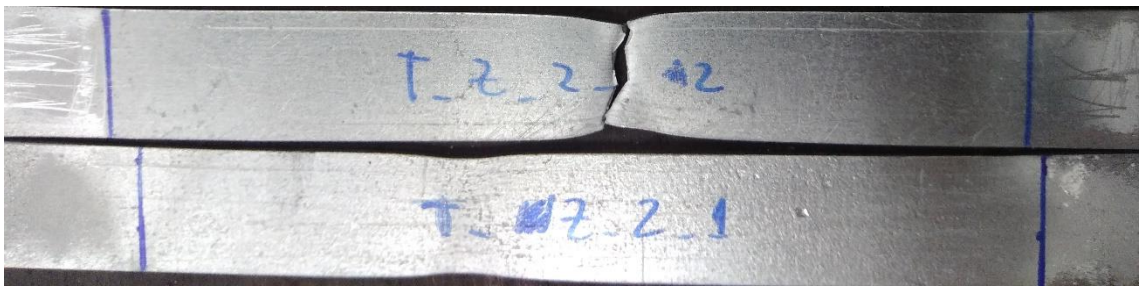

Figure 82 – Specimens of S350GD steel after the tensile tests.

Figure 83 – MTS servo-hydraulic testing machine.

Note that, for specimen T_Z_2_2, the test was performed until material's rupture, while for specimen T_Z_2_1, the test was stopped approximately when the specimen started presenting necking. With the data collected from the experimental work, the true stress - true strain curves (applying Eq. (4.5) and Eq. (4.6)) were also possible to draw and compared with the curve obtained using Swift´s hardening law (Figure 84). Note that the results attained for the two specimens were very similar, reason why data from specimen T_Z_2_1 will be the only considered.

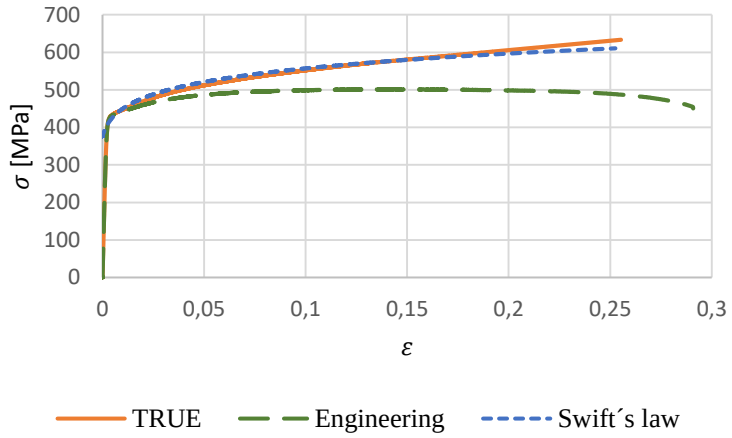

Figure 84 – Comparison of stress-strain diagrams between the engineering curve, true curve and Swift's hardening law curve of S350 GD steel.

In order to determine Swift´s hardening law constants, Swift´s law model - Eq. (3.1), the equation to obtain the plastic strain, given the total and elastic strain – Eq. (4.3) and Eq.(4.7) were used.

$$n = \frac{\log(\frac{\sigma_1}{\sigma_2})}{\log(\frac{\varepsilon_1 + \varepsilon_0}{\varepsilon_2 + \varepsilon_0})} \tag{4.7}$$

Where:

- ε_i is the plastic strain at a given point of the stress-strain curve;
- σ_i is the stress at a given point of the plastic stress-plastic strain curve.

The values for the strength coefficient, K and for the strain-hardening exponent, n that better characterized the flow curve of the material are presented in Table 10.

Table 10 – Swift's hardening law parameters for S350GD steel.

K [MPa]	n	ε_0
700	0,1	0,02

The material model for the Z-section profile was developed taking in consideration the constants from Swift's hardening law presented in Table 10. However, a comparison between the material behaviour determined experimentally and the curve estimated by the software (after introducing the values for yield strength, ultimate tensile strength and elongation – the same curve used in the U-channel profile) was performed. Figure 85 reveals the difference between the curves estimated by the software, given the yield strength of the material, the ultimate tensile strength and the elongation at the ultimate tensile strength and the curve obtained taking into account experimental results. However, the material used for the experimental work had different mechanical properties of the material used initially in the U-channel profile analysis (in spite of both being a S350GD steel). That being said, mechanical properties attained in the tensile tests were introduced in the software in order to obtain a more realistic comparison between the curves. The mechanical

properties gathered experimentally are presented in Table 11 and the comparison between stress-strain curves are presented in Figure 85.

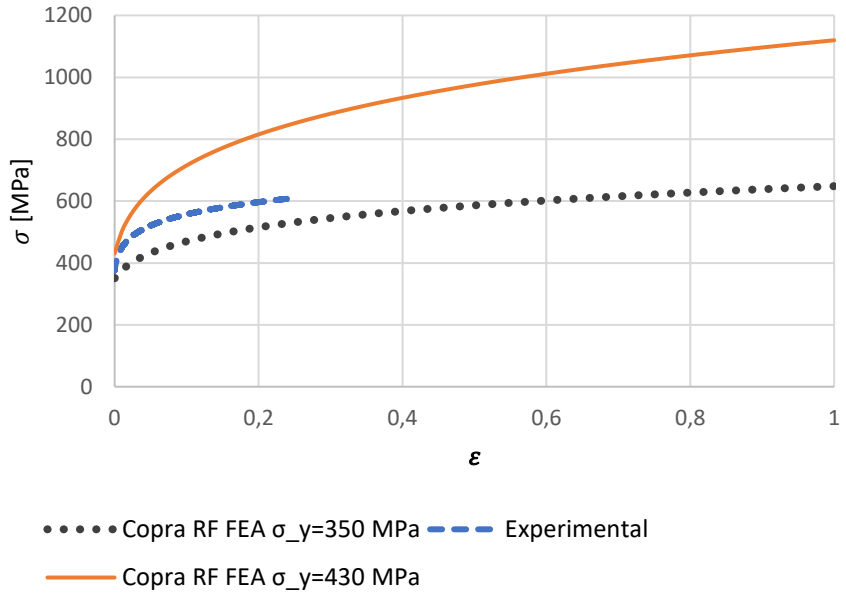

Figure 85 – Comparison between the stress-strain curves using Swift´s hardening law of S350GD steel.

The values introduced for the elastic properties were 210 GPa for Young´s modulus and 0,3 for Poisson's ratio and the constants presented in Table 11 were used for the plastic properties. Similar to the U-channel simulations, the Von Mises yield theory was used with isotropic hardening.

As far as sheet metal forming is concerned, the "coil" option (value of 1,3) and the "cutting (default 0.5*length)" option were also used.

Table 11 – Mechanical properties of S350GD steel obtained experimentally.

Name	**Yield Strength $R_{p\,0,2}$ [MPa]**	**Ultimate Tensile Strength R_m [MPa]**	**Elongation at Ultimate Tensile Strength A_{80} [%]**
S350GD	430	611	22,3

Note that the yield strength of the S350GD is higher than 350 MPa (yield strength measured experimentally was 430 MPa), since 350 MPa is the minimum specification for the yield strength of the material. Usually, most materials present higher values for the yield strength, including the material tested experimentally for this dissertation.

4.2. Nomenclature

Figure 86 reveals some nomenclature related to the Z-section profile simulation.

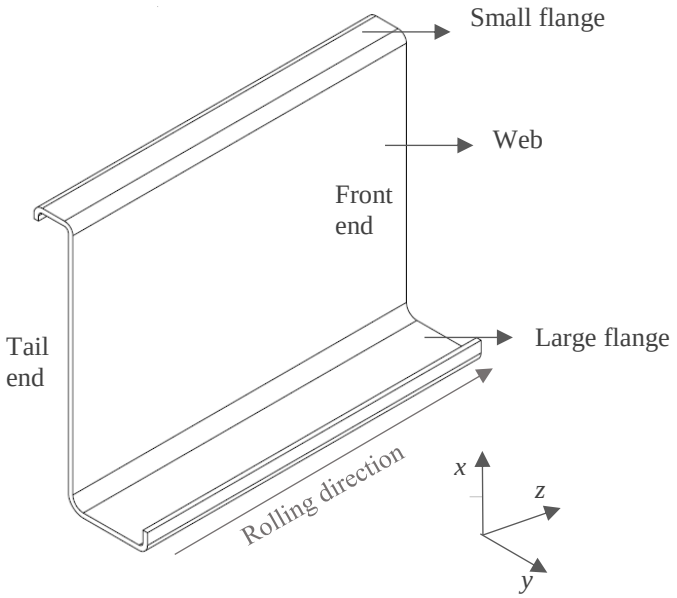

Figure 86 – Designated terms for different sections of the Z-section profile and reference global coordinate system.

4.2.1. Measurement of residual stresses along *xx* direction

As mentioned, the software allows the creation of a customized coordinate system. Residual stresses were measured in the same curvilinear coordinate system used in the U-channel profile. Moreover, the Z-section profile was divided into five planes (plane ii is located in the 20th node counting from the front end of the profile, plane iii in the 40th node and plane iv in the 60th node), as it is shown in Figure 87. These planes are approximately 63 mm apart.

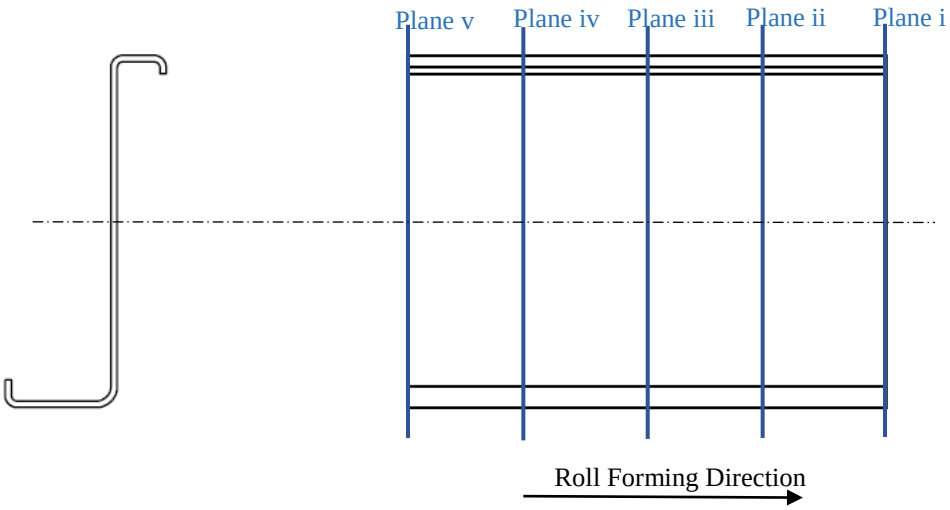

Figure 87 – Division of the Z-section profile in different planes.

Three paths were considered for residual stresses analysis: path 1 belongs to plane ii, path 2 to plane iii and path 3 to plane iv. Residual stresses were measured in the top surface and in the bottom surface, although, Figure 88 is only representing the path in the top surface.

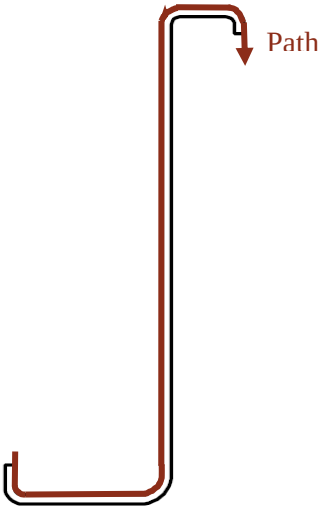

Figure 88 – Direction of each path in the top surface.

Note that plane i is located in the front end of the profile, while plane v is located in the tail end. For through thickness residual stresses, four paths in the large flange were created in which residual stresses were measured (Figure 89).

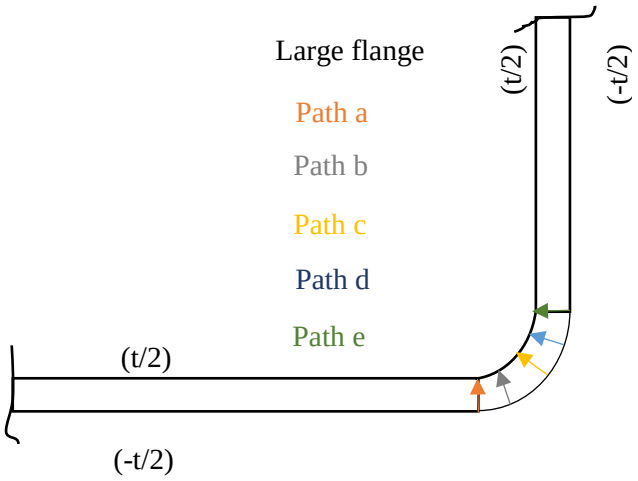

Figure 89 – Paths in the bending zone of the large flange of the Z-section profile.

4.2.2. Measurement of bow and springback

Longitudinal bow was measured approximately in the middle of the bottom surface (-t/2) of the web of the profile along the roll forming direction (z direction). Springback was measured in the large flange of the profile, as an angular deviation from the designed profile (see Figure 95 displayed in sub-chapter 4.3 that describes where springback will be measured).

Note that the profile is divided into 10 entities, as it is shown in Figure 90.

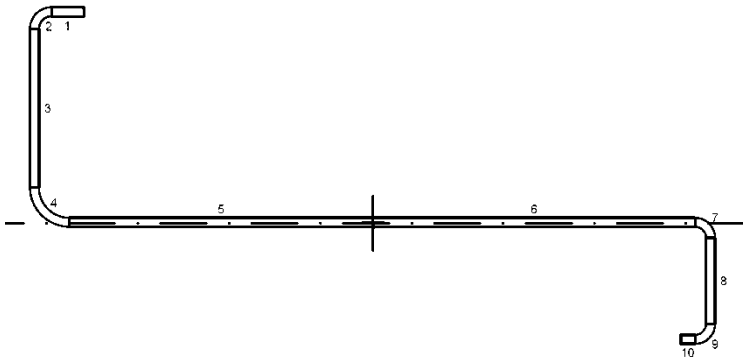

Figure 90 – Division of the Z-section profile in 10 entities.

As a side note, similar to the U-channel profile, the stresses were analysed in the final increment of the simulation after the free cut (increment 3580). However, for fatigue analysis, the increment right before the free cut (3540) was used to analyse the stresses and strains.

4.3. Roll forming simulation results and discussion

Regarding residual stresses, the distribution of transverse residual stresses along the *xx* direction of each element is similar for each path, in other words, for the top and bottom surfaces, the magnitudes and distributions of residual stresses are similar for each path, respectively, as it is shown in Appendix 10, Figures 10.1-10.2. Comparing the bottom and top surfaces, residual stresses suffer a noticeable increase in the corner regions, in both surfaces (Figure 91). The top surface of the large flange is under tension, while the small flange is under compression. The bottom surface displays the reverse results of the top surface. Path 2 and 3 display similar results (see Appendix 10, Figures 10.3-10.4). These opposite trends for the flanges were expected, since the bending of the large flange is in the opposite direction of the small flange. Plastic strains also present an increase in corner regions, as expected (Figure 92). Note that, in Figure 91, the regions that are marked with a grey arrow represent the corner regions.

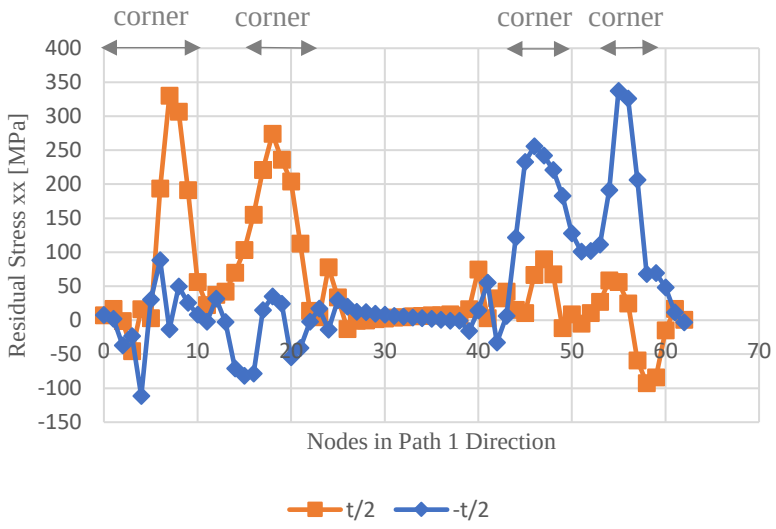

Figure 91 – Comparison of transverse residual stresses [MPa] along the *xx* direction between the top (t/2) and the bottom (-t/2) surface for path 1 of the Z-section profile.

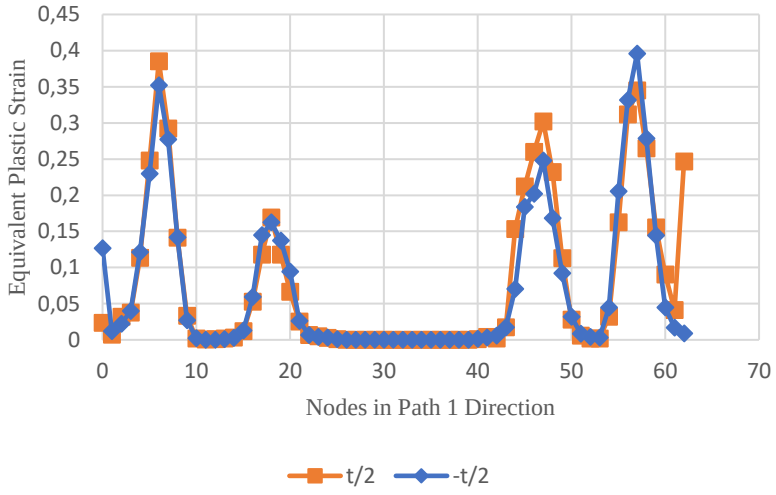

Figure 92 – Comparison of equivalent plastic strain along the xx direction between the top (t/2) and the bottom (-t/2) surface for path 1 of the Z-section profile.

Concerning through thickness residual stresses (Figure 93), as mentioned before, the transverse stress distribution results of the contribution of plastic stress originated to form the corner and elastic springback of the same corner. The nonlinear stress distribution is similar to the theoretical solution and the stress distribution obtained from the U-channel profile. However, the bottom surface is under tension, as opposed to what happened in the U-channel profile. A less refined mesh could be a possible explanation, since the distribution of these stresses are widely dependent on the mesh size that is being used.

Figure 94 shows that the large flange presents flare at both extremities and also presents edge waviness. As mentioned, flare is the result of stress release after the free cut of the profile. Regarding the visible waviness of the edges, it is important to notice that entities 2 and 9 (smaller corners in the flanges – see Figure 90) bending sequences only have four parts (the final shape of these entities is achieved only with four stations), which means that the stretching of outer fibres may exceed the yield point leading to edge waviness. Longitudinal edge strain must be maintained below a certain limit in order to prevent such defects. The distance between stations and the forming sequence have major influence on longitudinal edge strain, although, since the distance between stations is the same used in the U-channel profile, and the results did not display edge waviness, the main reason for this three-dimensional defect is the forming sequence. In addition, Bui and Ponthot (2008) numerical study revealed that low work hardening materials, which means materials with higher hardening exponent, lead to a reduction of edge waviness. The material model used in the U-channel profile has a hardening exponent, n of 0,148 while for the Z-section profile model, n equals 0,1. These findings are in agreement with the results from the Z-section profile simulation.

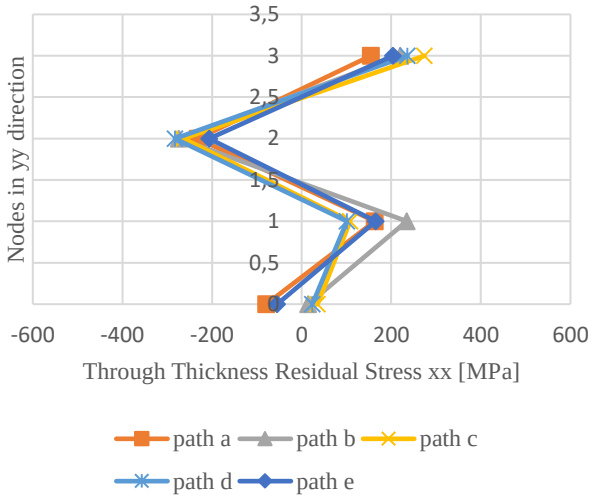

Figure 93 – Through thickness residual stresses [MPa] along the *xx* direction between for plane ii.

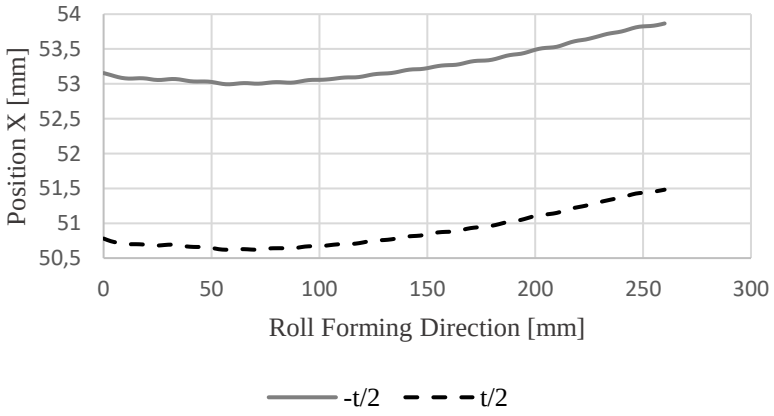

Figure 94 – Edge position of the flange of the Z-section profile.

Geometrical tolerances were not provided for the profile that is under analysis. Nonetheless, an industrial partner of the FASTCOLD project is working with similar profiles (Figure 95) and the tolerances for the same are described in Table 12. Note that the geometry and dimensions of the profile in Figure 95 are quite similar to Z-section profile.

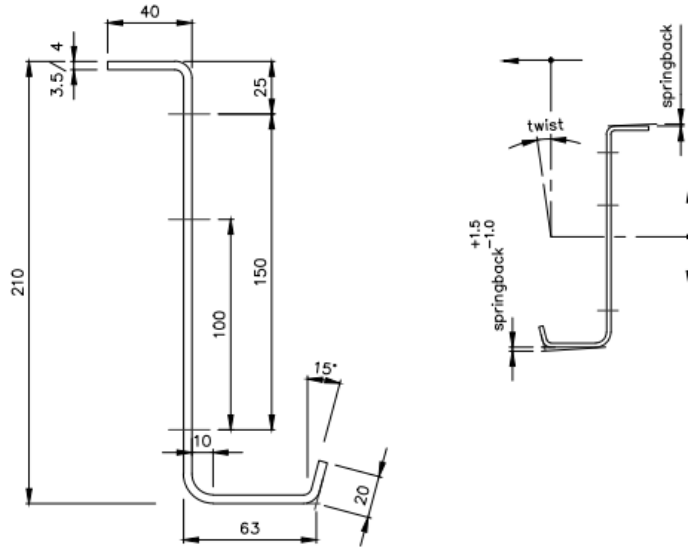

Figure 95 – Geometry and dimensions of a profile used by industrial partners of FASTCOLD project.

Table 12 – Tolerances of a profile used by industrial partners of FASTCOLD project.

Parameter	**Tolerance**
Springback	+/- 1mm
Bow	1mm/m

Longitudinal bow is a common defect in cold roll forming and, as mentioned, it can be caused by uneven longitudinal membrane strain in the web and in the flange. The maximum displacement verified was approximately 1,37 mm (Figure 96), which means that the tolerances are not being respected. Note that the strip only has 260 mm of length, which means the longitudinal bow is approximately 5mm/m.

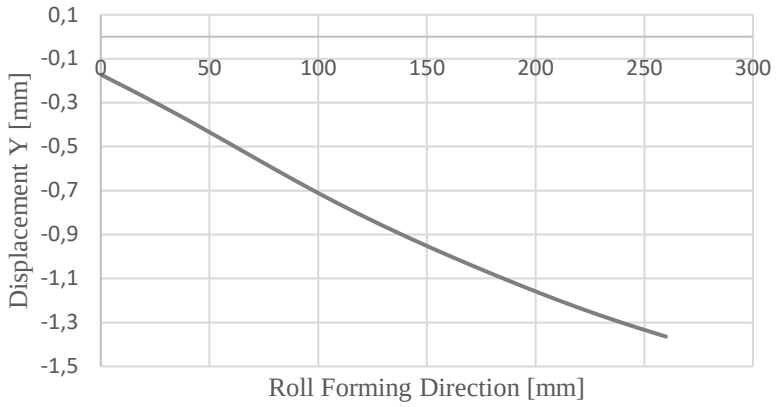

Figure 96 – Longitudinal bow measure on the bottom surface of the web.

The parametric study executed in Chapter 3 revealed that springback depends on the mesh used, especially in the number of elements across the thickness. For the Z-section profile, three elements along the thickness were used, which means that the measured springback might be higher than the springback obtained from an experimental work. Furthermore, the mesh is less refined than the one used in Chapter 3, which can lead to different stresses and strains distributions that can affect springback. Figure 97 also reveals that the tolerances for springback are not being respected, since even for the smaller value of springback (3,13°) the resulting deviation is 3,33 mm.

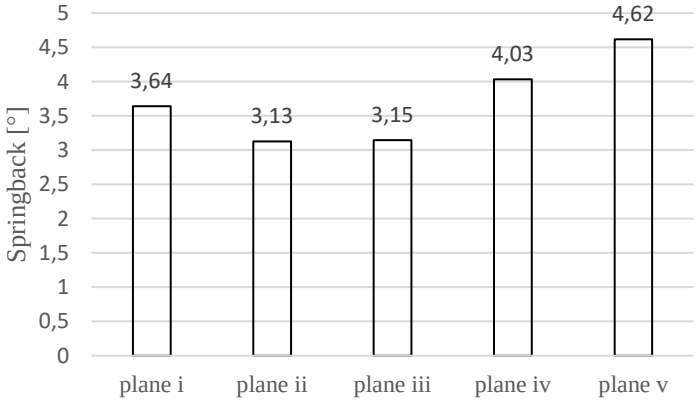

Figure 97 – Springback of the large flange of the Z-section profile.

4.4. Fatigue analysis of the Z-section profile

A similar fatigue analysis performed to the U-channel profile was conducted for the Z-section profile. The same external cyclic mechanical loads (2 kN, 4,5 kN and 9 kN) were applied in the large flange of the profile. These cyclic loads were also composed of two cycles, divided in 100 increments, for a total time of 12,57 seconds (4π seconds). The load was applied in 6 nodes of the large flange (59th to 61st node counting from the front end of the profile – Figure 98) in an area of 110 mm^2, approximately (the element size is approximately 3,33x8,32 mm) and in the middle of the length of the profile, disregarding the elements that were in contact in the rolls. Loads were applied in the top and bottom surfaces of the large flange (Figure 98). The increment used to performed this analysis was the one right before the free cut (increment 3540).

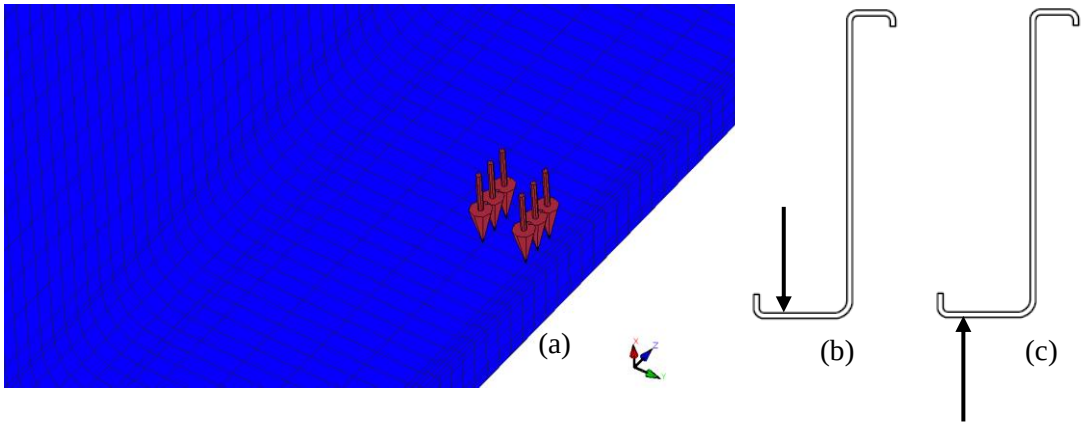

Figure 98 – External cyclic mechanical loads (a) applied in the top (b) and bottom (c) surfaces of the large flange of the Z-section profile.

Regarding boundary conditions, the nodes of the extremities of the web (in this situation, the extremities was considered the elements of the interface between the elements of the profile and the elements that are deactivated to simulate the end cut, similar to the U-channel profile) were restrained in the *x*, *y* and *z* directions, only in the web zone. Boundary conditions were not applied in the corner regions or the flange.

For the same reason described in Chapter 3, the stresses that are going to be studied for the fatigue analysis are the stresses in the *xx* direction of the curvilinear coordinate system.

Firstly, the critical areas and the critical node where fatigue cracks might nucleate were identified. Figure 99 illustrates the stress along the *xx* direction (of the curvilinear coordinate system) distribution field and it is possible to conclude that the corner region represents the critical area. Note that the load was applied as far as possible of the corner region, in order to simulate the worst scenario for fatigue damage.

Secondly, four paths were defined (Figure 100) in the corner region and for an applied load in the top surface of the large flange, stresses were only measured in the inner corner, since the study performed in the U-channel profile revealed that the application of loads intensifies the tensile state of the inner corner surfaces and tensile stresses are detrimental to fatigue life of components. Similar to the analysis performed in the U-channel profile, stresses were measured at the

maximum load amplitude (steps 26 and 76 of the numerical simulation) and in the absence of load (steps 51 and 100 of the numerical simulation), as it is shown in Figure 65.

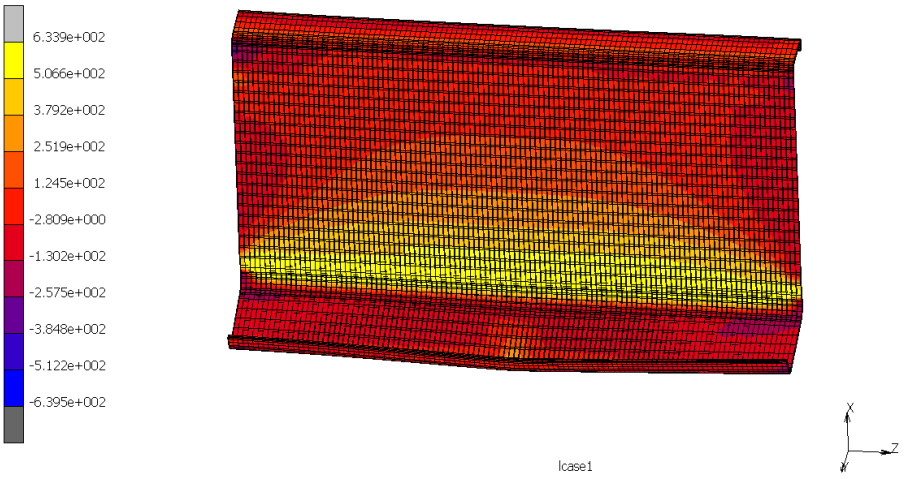

Figure 99 – Stresses [MPa] along the *xx* direction of curvilinear coordinate system for step 26 and for a maximum load applied in the top surface of 9 kN.

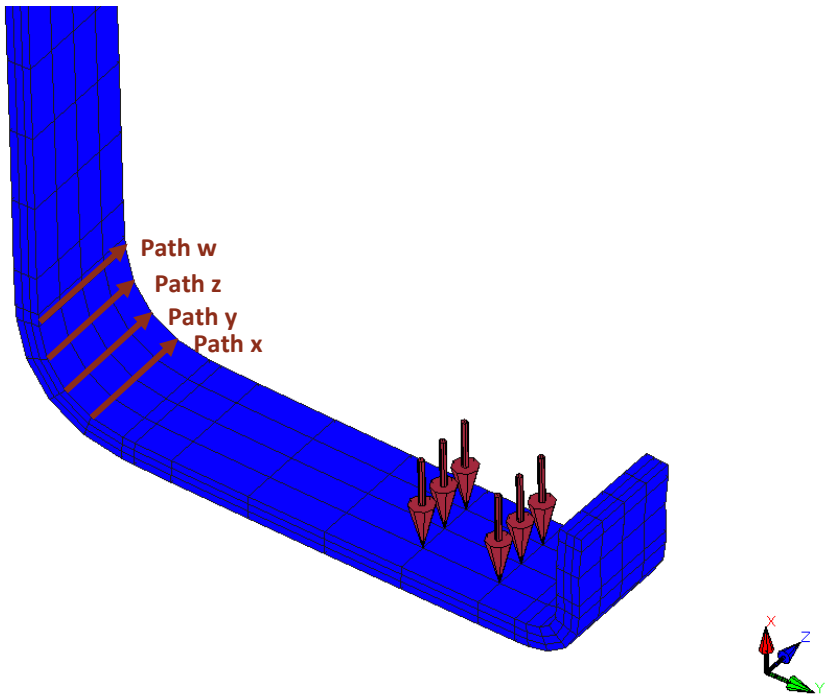

Figure 100 – Paths were stresses were measured in the Z-section profile.

Thirdly, as previously stated, mechanical loads were also applied in the bottom surface of the large flange. The same paths in the corner regions used in the analysis of stresses with loads in the top surface were used in the analysis of stresses with the load applied in the bottom surface. Stresses distribution fields (Figure 101) revealed that the critical area was in the outer corner, since for every maximum load amplitude, the outer corner is under tension, while the inner corner surface is under compression (as mentioned, compressive states of stresses are beneficial to fatigue life).

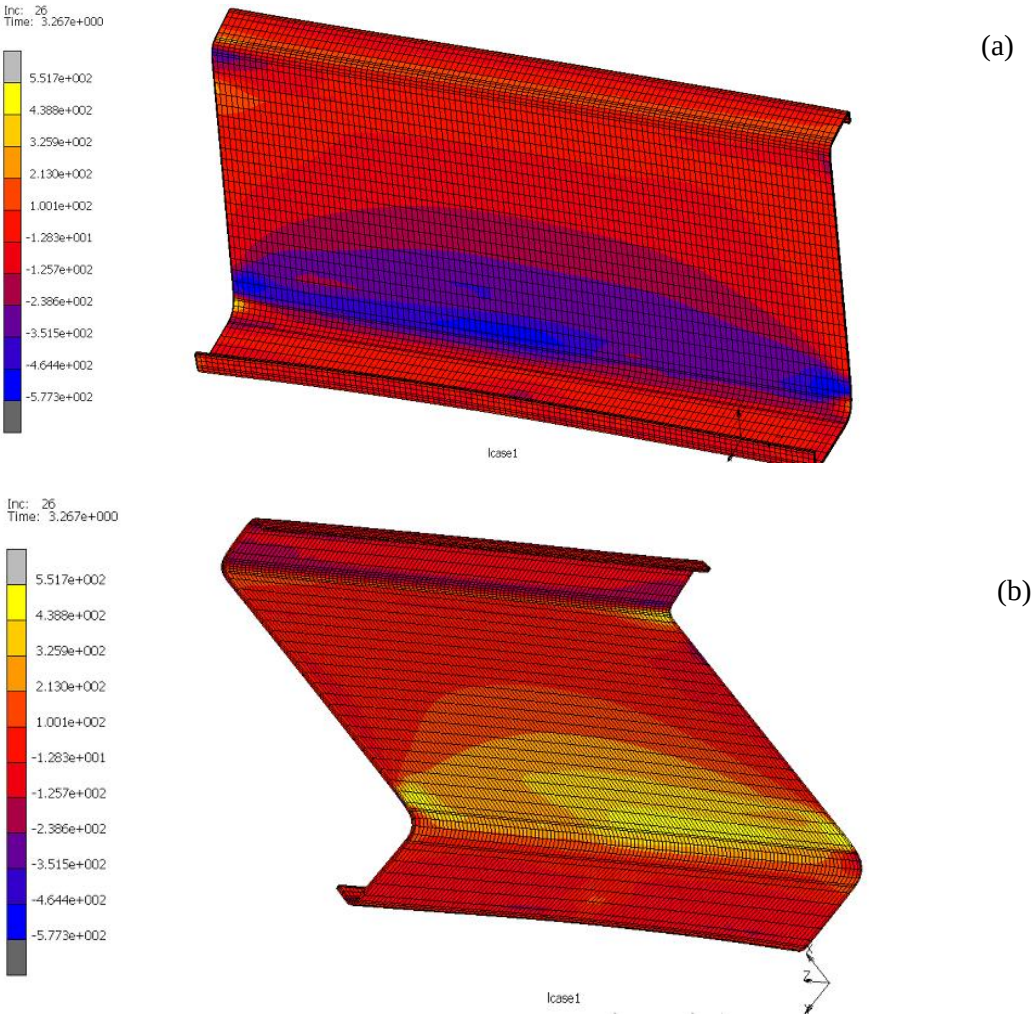

Figure 101 – Stresses [MPa] along the *xx* direction of curvilinear coordinate system for step 26 and for a maximum load applied in the bottom surface of 9 kN: (a) compressive state of the inner corner; (b) tensile state of the outer corner.

Analysing the results, dividing them into steps and comparing them with the initial state of the profile (the Z-section profile presented stresses and strains that derived from the roll forming process), it was concluded that:

- The inner and outer corner surfaces were under tension before the application of external loads. However, the outer corner surfaces presented smaller values for tensile stresses and for path w, the stresses were compressive. These results are consistent with "through thickness residual stresses" plots (Figure 93), that reveal an elastic springback of the material, but, for the bottom surface, the stresses did not reach negative values. In spite of the similarities in terms of distribution of "through thickness residual stresses" between the U-channel profile and the Z-section profile, the stress values diverge from each other. One possible explanation is the different number of station used in each model and/or the difference in the meshes used for each model.

- For steps 26 and 76 and for the load applied in the top surface, the magnitude of stresses tend to increase its value (along the paths created in the inner corner). This increase is more visible for higher loads. Path x represents the exception, since tensile stresses turned into compressive stresses for 2 kN and 4,5 kN. For steps 51 and 100, residual stresses tend to decrease their values from the previous state and for most paths, compressive stresses were achieved.

- For steps 26 and 76 and for the load applied in the bottom surface, stresses increased their values (along the paths created in the outer corner surfaces), and higher loads led to higher tensile residual stresses. Once again, path x represents the exception, since the maximum tensile residual stresses occurred for the minimum load amplitude (2kN). For steps 51 and 100, most paths revealed a decrease in the value of residual stresses, and for higher loads, paths z and w presented compressive stresses.

To summarize, the behaviour of the material did not present much difference from the results observed in the U-channel profile. However, the magnitude of the stresses were slightly different for the reasons mentioned above. These results are all presented in Appendix 11, Tables 11.1-11.4. Similar to the results from the U-channel profile, after the application of mechanical loads, the corner presented stresses that differ from the ones in the initial state, which proves the existence of an elastoplastic effect of the material in the first cycle of the load. The return to the original state should only be observed for an elastic model.

Furthermore, analysing the results in Appendix 11, Tables 11.1-11.4, path w represents the critical path, specifically the 5^{th} node counting from the beginning of the path since it experiences higher values of stress for steps 26 and 76. For this reason, fatigue life of the profile was estimated taking into account the critical area, particularly this node where a crack is more likely to be initiated. Figures 102-107 display the resulting stresses histories due the application of three different cyclic loads, from which the stresses ranges will be extracted.

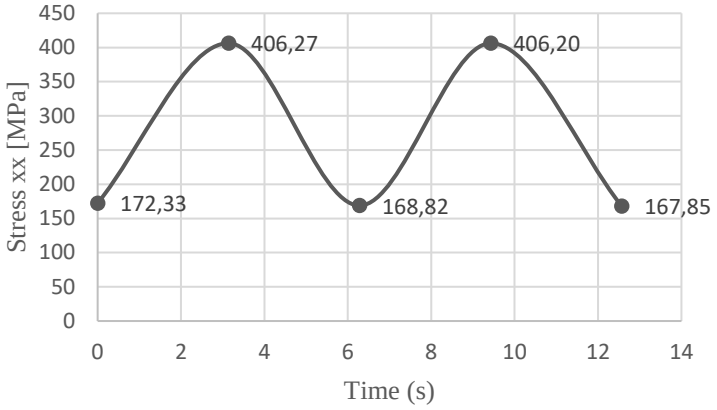

Figure 102 – Stresses in the critical node for a maximum mechanical cyclic load of 2kN applied in the top surface.

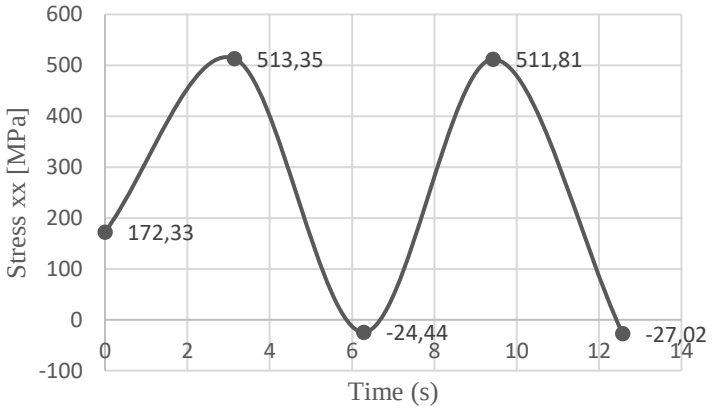

Figure 103 – Stresses in the critical node for a maximum mechanical cyclic load of 4,5 kN applied in the top surface.

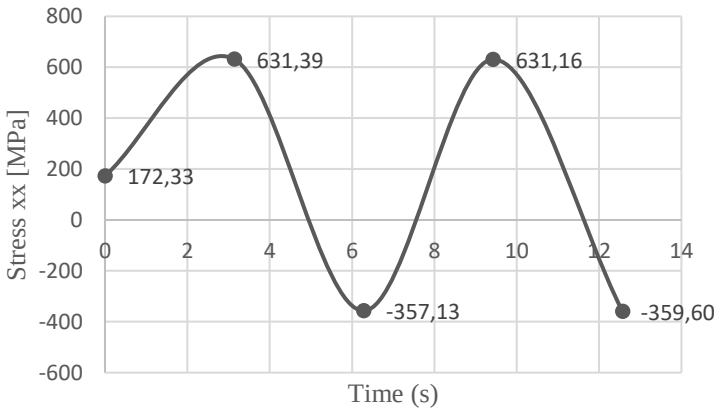

Figure 104 – Stresses in the critical node for a maximum mechanical cyclic load of 9 kN applied in the top surface.

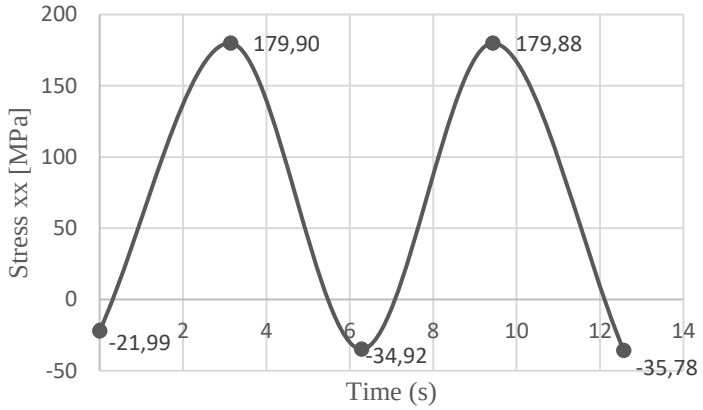

Figure 105 – Stresses in the critical node for a maximum mechanical cyclic load of 2kN applied in the bottom surface.

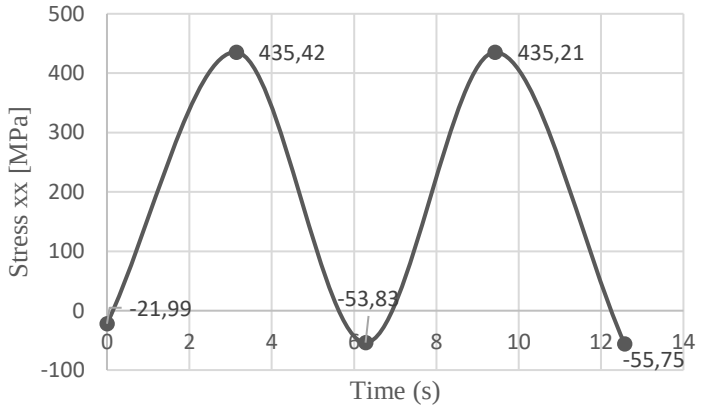

Figure 106 – Stresses in the critical node for a maximum mechanical cyclic load of 4,5 kN applied in the bottom surface.

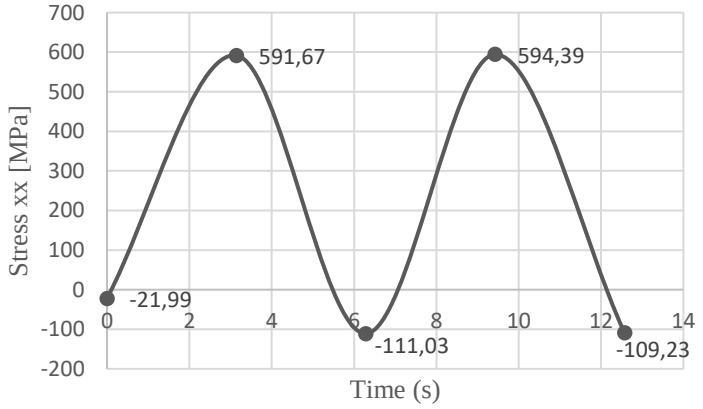

Figure 107 – Stresses in the critical node for a maximum mechanical cyclic load of 9 kN applied in the bottom surface.

The model for the Z-section profile uses an isotropic hardening rule, as the U-channel profile. Since the loads applied are equal and material properties are similar, stress-strains curves were assumed to have a similar behaviour to the U-channel model, in other words, the material presents an elastic behaviour, after the second cycle. For this reason, to estimate the fatigue life of the profile, a local stress-based approach was also used in the Z-section profile model. Taking into consideration the stress range from steps 26 and 76 and fatigue parameters, σ_f' and b obtained by Jesus et al. (2012) experimental fatigue tests on smooth specimens of S355 mild steel (Table 2), σ_m, $\Delta\sigma$ and N_f (Tables 10-11) were calculated.

Table 13 – Estimated number of cycles for three different cyclic loads applied in the top surface of the large flange of the Z-section profile using the local S-N based approach.

Load	σ_{max}	σ_{min}	σ_m	$\Delta\sigma$	N_f
2 kN	406,20	167,85	287,03	238,35	1,2E+08
4,5 kN	511,81	-27,02	242,40	538,83	2,7E+04
9 kN	631,16	-359,60	135,78	990,76	1,4E+02

Table 14 – Estimated number of cycles for three different cyclic loads applied in the bottom surface of the large flange of the Z-section profile using the local S-N based approach.

Load	σ_{max}	σ_{min}	σ_m	$\Delta\sigma$	N_f
2 kN	179,88	-35,78	72,05	215,66	8,8E+09
4,5 kN	435,21	-55,75	189,73	490,96	1,7E+05
9 kN	594,39	-109,23	242,58	703,62	1,3E+03

Figure 108 reveals the approximate linearity in log-log scales of results between the load applied to the profile and the number of cycles until failure. Performing a similar analysis to the U-channel profile and assuming the same number of cycles for an infinite life for this structure, it is possible to determine the maximum load that can be applied without compromising the structure (preventing fatigue damage). The maximum load that can be applied in the top and bottom surfaces for an infinite life of the structure are approximately 2,8 kN and 3,3 kN, respectively (see Figure 108). Similar to the conclusions obtained from the simulations with the U-channel profile, for a cyclic load of 9 kN the number of cycles was 140 for the inner corner and 1300 for the outer corner, for a maximum load applied in the top and bottom surfaces of the large flange, respectively.

To summarize, the model used for the Z-section profile contains some of the limitations of the model used for the U-channel profile. Some conclusions are important to be stated such as:

- The length of the strip did not suffer any change, since the CPU time required to perform a simulation with increased length exceeded the time available to complete this investigation. For this same reason, the mesh used was not the same used in the U-channel

profile model, since the CPU time required to perform this simulation was 15 days. Using a less refined mesh allowed the simulation to be completed in less than half of that time. Figure 109 shows the different CPU times for all the simulations performed in the present chapter and Chapter 3 (U-channel). It is important to have in mind that four CPUs at 50% of capacity were used to perform these simulations;

- The hardening rule for these simulation should also be kinematic instead of isotropic, in order to understand the best approach to use in fatigue life estimations. Note that, the kinematic hardening rule for this model was not used, since the simulation had already been performed when the results from the fatigue analysis of the U-channel profile were extracted and analysed. At that point, initiating another simulation given the remaining time to conclude this dissertation had become unfeasible;
- Figures 101-107 reveal a stress relaxation of the initial state of the profile, similar to what happened in the U-channel profile. This stress relaxation is more visible for higher loads.
- The constants introduced in the software to determine Swift´s hardening law curve for the material were more realistic than the curve estimated by the software for the U-channel profile, from basic tensile properties.

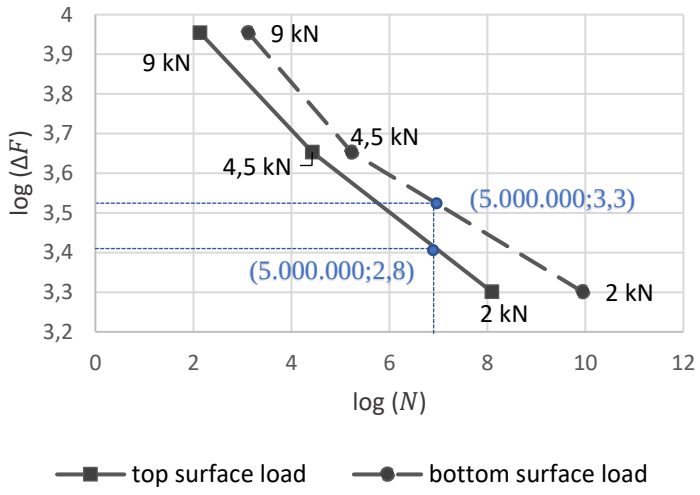

Figure 108 – Number of cycles for maximum loads of 2 kN, 4,5 kN and 9 kN in a logarithmic scale for a Z profile.

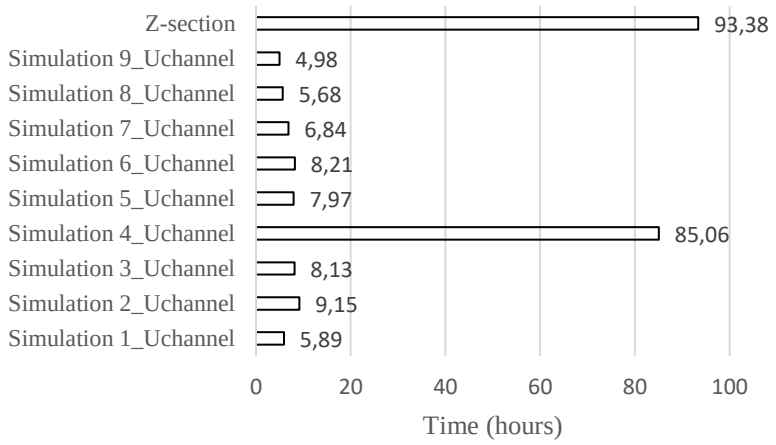

Figure 109 – CPU time required to conclude every simulation performed in Chapter 3 and 4.

Chapter 5

Conclusion

5.1. Conclusions

Racking systems presented, nowadays, in the logistic industry are usually made of thin-walled cold formed steel sections. However, the lack of fatigue design rules in EN1993-1-9: Design of steel strictures-Part 1-9 regarding these structures leads to an unpredictable fatigue failure of these racking systems. FASTCOLD project, among other goals, aims at providing fatigue design rules for cold roll formed steel members. As previously stated, cold roll forming is a complex bending process, where bending occurs gradually (three-dimensional process). In order to evaluate stress range variations in cold formed profiles, especially in Z-section profiles (rail section profile that is being study by FASTCOLD project), due to the application of external mechanical cyclic loads, learning about cold roll forming process and the influence of different model designs in stress state and presence of defects in the final product is of crucial importance. In other words, the stress state of the profile has to be known before (which means, after the roll forming process) and after the application of cyclic loads.

Literature review (Chapter 2) allowed the enlargement of knowledge about the cold roll forming processes and fatigue analysis approaches. In addition, various investigations found on literature were reported in this dissertation to provide a comparison and a better understanding of the results reported in Chapters 3 and 4. The main conclusions reached in Chapters 3 and 4 are presented, as follows:

Chapter 3

Though the parametric study performed in Chapter 3, the influence of different parameters in the final shape of a U-channel profile as well as its stress and strain state after the roll forming process, such as the influence of the number of stations that compose the forming line, the radius/thickness ratio of the bending line, the distance between stations, the material properties, the refinement of the mesh across the thickness and the influence of driven rolls with different friction coefficients, were analysed:

- For regions far away from the extremities of the profile (in other words, regions where the free cut of the profile does not influence the stress-strain state of the profile), through thickness residual stresses across the corner regions present a similar non-linear distribution to the theoretical distribution presented in Chapter 2. However, the theoretical solution assumes a profile without any three-dimensional defects, reason why the theoretical solution for cold roll forming is the same for press-braked profiles. Nonetheless, cold roll forming is a three dimensional process, where the bending occurs continuously. For this reason, three-dimensional effects cannot be neglected;
- Through thickness residual stresses did not display significant deviations when the number of elements across the thickness increased. However, springback decreased (10% smaller than the values presented for the simulation of reference with three elements across the thickness);
- The extremities of the profile reveal the influence of the end cut in the stress state. Furthermore, end cut of profiles are responsible for a stress relief that led to end flare;
- For higher number of stations, the strip bends more gradually, with smaller fold angles leading to less residual peak membrane strains, smaller end flares and less edge waviness. Increasing the number of forming stations from six to nine led to a peak longitudinal membrane strain three times lower. Nevertheless, smaller end flares were not verified for the simulation with nine stations, due to the influence of springback in the extremities of the profile – springback presents higher values in planes i and iv for simulation 3 (nine stations);
- For higher inter-stations distances, the simulation performed did not allow to draw reasonable conclusions, since the length of the strip and consequently the node where the longitudinal peak membrane strain was measured did not match with the strip length and the node (where longitudinal membrane strain was measured) of simulation 1 (reference). However, literature reveals that permanent plastic strain decreases when the distance between stations increases, since the bending occurs more gradually (higher length in the forming line), which provides a higher recovery of strains;
- For simulations with driven rolls, residual stresses did not present divergences from the simulation of reference (simulation 1 with non driven rolls, and consequently, without friction), although, in spite of some studies found on literature stated that friction coefficient did not influence springback, higher friction coefficients led to higher springback for the parametric study conducted in this dissertation;
- For different radius/thickness ratios, through thickness residual stresses did not display significant differences from the simulation of reference (r=8 mm) and from the theoretical solution. Note that thickness size was constant for all simulations (t=3,5 mm). However, some parts of the profile (plane iii and plane iv) presented an increase in springback when increasing the radius/thickness ratio. Smaller radius tend to have smaller values of springback, since the outside fibers of the bend region suffer larger elongations, quickly reaching quickly the yield point, which leads to smaller elastic return of the material. This trend is not verified for every section of the profile. The measurement of springback can be affected by three-dimensional defects. For instance, presence of flare in the extremities of the profile explains the higher values of springback for r=4 mm than the springback for r=8 and 12 mm;
- For materials with higher yield strength, higher residual stresses in transversal direction and higher springback were detected. S460 steel (used in comparison with S350 from simulation 1) has a higher elastic limit than S350 steel, leading to higher elastic recovery

– increased springback. This increase in springback justifies the change in the distribution of through thickness residual stresses – the "approximate linearity" distribution could be due to the increase in the elastic springback component (as a side note, remember that the theoretical non-linear solution of residual stresses results of the sum of the plastic bending component and the elastic bending component, Figure 19).

To sum up, cold rolling is a three-dimensional complex process and the three-dimensional defects cannot be disregard. That being said, a good roll and process design is a key factor to minimize such defects.

Regarding fatigue analysis, after the application of an external cyclic load, it was concluded that the bend lines represent the critical areas, where fatigue crack nucleation tend to occur. The inner bend surface (inner corner) presents, after the roll forming process, a tensile state (every path of the inner corner surface in under tension, except path x and the critical node, which are under compression: -44,25 MPa) and with the application of the external mechanical load, these tensile stresses increase their magnitude, which is detrimental to fatigue life. After analysing the stress range in the critical node for the three loads studied (2 kN, 4,5 kN and 9 kN), a stress relaxation after the first cycle was observed, especially for higher loads. The second cycle showed no variations of the maximum and minimum stresses, proving an elastic behaviour of the material in the second cycle. For this reason, a local stress-based approach was used to estimate fatigue life of the component. For an external load of 9 kN, the number of cycles until failure was 540 – low cycle fatigue. Since stress-based approaches are not suitable for low cycle fatigue, it was clear that the hardening rule used (isotropic hardening) was not appropriate, since the Bauschinger effect was being neglected. Summarizing, a kinematic hardening rule should be used to perform the roll forming simulations.

Chapter 4

For the analysis of the Z-section profile, only one simulation was performed and the mesh used was less refined than the mesh used in the U-channel model, because, given the time available and the CPU time requirements to perform this last simulation, it was unfeasible to use a more refined mesh (the time estimated to simulate the Z-section profile model with the same mesh used in the U-channel profile model would be 15 days).

Taking into consideration the profile after the roll forming process, transverse residual stresses and equivalent plastic strains display peaks of values in the bend surfaces. Moreover, equivalent plastic strains also present high values in the edge flanges of the profile, being the reason for the waviness detected in these areas. Additionally, given the tolerances of a similar profile used by an industrial partner of FASTCOLD project, the results for springback and bow were not in agreement with the provided tolerances. Some reasonable explanations are:

- The mesh used may not be appropriate. A more refined mesh could lead to better results;
- The number of stations is not enough to satisfy such tight tolerances;
- The length of the strip (520 mm) and the distance between stations is not sufficient to allow a smooth progressive bending.

The parametric study conducted in Chapter 3 provides the knowledge to apply the necessary changes to the model of the Z-section profile, thus reducing the defects mentioned earlier.

Concerning fatigue analysis, the mechanical loads (equal to the ones used in Chapter 3) were applied both in the top and bottom surfaces of the large flange of the Z-section profile. Similar to the U-channel profile, the bend surface represents the critical area (inner corner surfaces for the load applied in the top surface and outer corner surfaces for the load applied in the bottom surface). Identical to the results from the U-channel profile, the number of cycles until failure estimated were 140 and 1300 for an external load applied in the top and bottom surfaces, respectively, proving, once again, that the simulation should be performed using a kinematic hardening rule.

Regarding infinite life of components, an important conclusion is that, for the U-channel profile, higher loads (3,5 kN) can be applied to the structure without introducing fatigue damage, while for the Z-section profile the maximum loads that can be applied in the top and bottom surfaces for an infinite life are 2,8 kN and 3,3 kN, respectively. Higher maximum loads were expected for the Z-section profile, since this structure was design to present higher stiffness, due to the presence of small flanges in the end of the structure (Figure 110). However, stress range observed for the Z-section profile when the load was applied in the top surface of the large flange was higher than stress range from the U-channel profile.

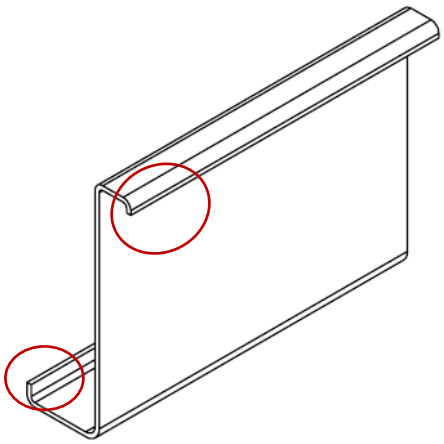

Figure 110 – Small flanges that provide higher stiffness to the Z-section profile.

Note that, for fatigue analysis, increments used for all studies were the ones before the end cut (increment 1185 for simulation 1 – U-channel profile and increment 3540 for the Z-section profile). Numerical studies conducted by partners of FASTCOLD project revealed that the stress fields are not influenced by boundary conditions in the extremities of the profiles' web for strip lengths higher than 500 mm. For this reason, the increments after the free cut were not used since, after the free cut, the strip only has approximately 260 mm of length.

5.2. Future work

Given the extent of proposed goals and tasks, not only for this dissertation, but also for FASTCOLD project, some recommendations about future investigations and work concerning this matter is provided, as follows:

- Perform a parametric study regarding the mesh used in the simulations of the Z-section profile. Given the magnitude of the required CPU time usage to conduct these simulations, an optimized mesh is of crucial importance;
- Design a model with a strip length after end cut of 1000 mm, which implies using a distance between stations of 1000 mm with a value for the "coil" option of 2. However, these parameters should also be defined taking into consideration the experimental set up of the process;
- Optimize the roll forming parameters to satisfy the tolerances provided;
- Design the COPRA RF model with the real dimensions of rolls and machine parameters that will be used by industrial partners to manufacture the profiles;
- Conduct an experimental fatigue tests on smooth specimens of S350GD steel, in order to determine the cyclic elastoplastic fatigue constants, σ_f' and b;
- Perform the simulations of the Z-section profile, using a kinematic hardening rule and revaluate the best approach to estimate fatigue life of the component;
- Conduct experimental fatigue tests on Z-section profile and compare/validate the results of the numerical simulations. Measurement of residual stresses should be performed in the bend line, since numerical results evidentiate this area as the critical part of the profile. Stresses along the *xx* direction of the curvilinear coordinate system are fairly easy to measure since the directions of these stresses are known;
- Introduce in the numerical model the effects on stresses of the sheet coiling, uncoiling and flattening (operations that precede the roll forming process);
- Introduce Fracture Mechanics approaches and analyse the influence of residual stresses on crack propagation.

References

Abee, A., A. Sedlmaier, and C. Stephenson. 2010. "Development of New 3D Roll Forming Applications by Means of Numerical Analysis as a Part of a Quality Control Methodology." *CBM Metal Matters,* 21–24.

Abeyrathna, B. 2014. "In-Line Shape Compensation for Roll Forming through Process Parameter Monitoring." Deakin University.

Abeyrathna, B., B. Rolfe, and M. Weiss. 2017. "The Effect of Process and Geometric Parameters on Longitudinal Edge Strain and Product Defects in Cold Roll Forming." *International Journal of Advanced Manufacturing Technology* 92 (1–4): 743–54.

Abvabi, A. 2014. "Effect of Residual Stresses in Roll Forming Process of Metal Sheets." Deakin University.

B2B Metal. 2014. "S460N Steel Grade, Mechanical Properties, Chemical Composition, Grade Equivalent." 2014. http://www.b2bmetal.eu/en/pages/index/index/id/161/.

Badr, O.M., B. Rolfe, P. Hodgson, and M. Weiss. 2013. "Numerical Investigation about the Effect of Increasing the Number of Forming Passes on the Quality of AHSS Roll Formed Products." In *AIP Conference Proceedings,* 1567:872–75. American Institute of Physics.

Basquin, O. H. 1910. "The Exponential Law of Endurance Tests." *Proceedings-American Society for Testing and Materials* 10: 625–30.

Berner, S., M. Storbeck, and P. Groche. 2011. "A Study on Flexible Roll Formed Products Accuracy by Means of FEA and Experimental Tests." In *AIP Conference Proceedings,* 1353:345–50. American Institute of Physics.

Bhattacharya, D., and P. D. Smith. 1984. "The Development of Longitudinal Strain in Cold Roll Forming and Its Influence on Product Straightness." *First International Conference on Technology of Plasticity,* 422–27.

Boardman, B. 1990. "Fatigue Resistance of Steels." In *ASM Handbook: Properties and Selection: Irons, Steels, and High-Performance Alloys,* 1:673–82.

Broek, D. 1982. *Elementary Engineering Fracture Mechanics*. First edit. Martinus Nijhoff.

Bui, Q. V., and J. P. Ponthot. 2008. "Numerical Simulation of Cold Roll-Forming Processes." *Journal of Materials Processing Technology* 202 (1–3): 275–82.

Coffin, L. F. 1954. "A Study of the Effects of the Cyclic Thermal Stresses on a Ductile Metal." *The American Society of Mechanical Engineers Journal* 76: 931–50.

data M Sheet Metal Solutions GmbH. n.d. “COPRA® FEA RF: Data M.” Accessed May 21, 2018. http://www.datam.de/en/products-solutions/simulation-with-fea/copraR-fea-rf/.

———. 2015. *COPRA® FEA RF User Manual*.

Dattoma, V., M. De Giorgi, and R. Nobile. 2004. “Numerical Evaluation of Residual Stress Relaxation by Cyclic Load.” *The Journal of Strain Analysis for Engineering Design* 39: 663–72.

Ellyn, F. 1997. *Fatigue Damage, Crack Growth and Life Prediction*. First edit. Chapman & Hall.

EN 1993-1-9. 2005. “Eurocode 3: Design of Steel Structures - Part 1-9: Fatigue.” *European Committee for Standardization (CEN)* 7.

Farzin, M, M Salmani Tehrani, and E Shameli. 2002. “Determination of Buckling Limit of Strain in Cold Roll Forming by the Finite Element Analysis.” *Journal of Materials Processing Technology* 125–126: 626–32.

Ferreira, P. 2016. “Roll Forming - a Study on Machine Deflection by Means of Experimental Analysis and Numerical Developments.” Faculdade de Engenharia da Universidade do Porto.

Fish, J., and T. Belytschko. 2007. *A First Course in Finite Elements*. Edited by John Wiley. *Engineering*. Wiley.

Future Market Insights. 2014. “Roll Forming Machine Market: Global Industry Analysis 2012 – 2016 and Opportunity Assessment.” https://www.futuremarketinsights.com/reports/roll-forming-machine-market.

Giorgi, M. De. 2011. “Residual Stress Evolution in Cold-Rolled Steels.” *International Journal of Fatigue* 33 (3): 507–12.

Groche, P., P. Beiter, and M. Henkelmann. 2008. “Prediction and Inline Compensation of Springback in Roll Forming of High and Ultra-High Strength Steels.” *Production Engineering* 2 (4): 401–7.

Güner, A. 2007. “Assessment of Roll-Formed Products Including the Cold Forming Effects.” Graduate School Of Natural And Applied Sciences.

Gustavsson, A., M. Larsson, and A. Melander. 1997. “Fatigue Life of Pressed Steel Sheet Components.” *International Journal of Fatigue* 19 (8–9): 613–19.

Halmos, G. T. 2013. *Roll Forming Handbook. Journal of Chemical Information and Modeling*. Vol. 53.

Han, Z. W., C. Liu, W. P. Lu, and L. Q. Ren. 2001. “The Effects of Forming Parameters in the Roll-Forming of a Channel Section with an Outer Edge.” *Journal of Materials Processing Technology* 116 (2–3): 205–10.

Han, Z. W., C. Liu, W. P. Lu, L. Q. Ren, and J. Tong. 2005. “Spline Finite Strip Analysis of Forming Parameters in Roll Forming a Channel Section.” *Journal of Materials Processing Technology* 159 (3): 383–88.

Hassan, S. K., D. Polyzois, and G. Morris. 1994. “Fatigue Behaviour of Cold-Formed Steel Sections.” *Proceedings of the Twelfth Internation Specialty Converfernce on Cold-Formed Steel Structures*, 675–89.

Heislitz, F., H. Livatyali, M. A. Ahmetoglu, G. L. Kinzel, and T. Altan. 1996. “Simulation of Roll Forming Process with the 3-D FEM Code PAM-STAMP.” *Journal of Materials Processing Technology* 59 (1–2): 59–67.

Hong, S., S. Lee, and N. Kim. 2001. "A Parametric Study on Forming Length in Roll Forming." *Journal of Materials Processing Technology* 113 (1–3): 774–78.

Jesus, A. M.P., R. Matos, B. F.C. Fontoura, C. Rebelo, L. Simões da Silva, and M. Veljkovic. 2012. "A Comparison of the Fatigue Behavior between S355 and S690 Steel Grades." *Journal of Constructional Steel Research* 79: 140–50.

Kang, W., Y. Zhao, W. Yu, S. Wang, Y. Ma, and P. Yan. 2014. "Numerical Simulation and Parameters Analysis for Roll Forming of Martensitic Steel MS980." *Procedia Engineering* 81: 251–56.

Klippstein, K. H. 1980. "Fatigue Behavior of Sheet-Steel Fabrication Details Fatigue Behavior of Sheet-Steel Fabrication Details." *International Specialty Conference on Cold-Formed Steel Structures*.

Laboube, R. A., and W. Yu. 1999. "Design of Cold-Formed Steel Structural Members and Connections for Cyclic Loading (Fatigue)." *Center for Cold-Formed Steel Structures Library*.

Lindgren, M. 2007a. "An Improved Model for the Longitudinal Peak Strain in the Flange of a Roll Formed U-Channel Developed by FE-Analyses." *Steel Research International* 78.

———. 2007b. "Cold Roll Forming of a U-Channel Made of High Strength Steel." *Journal of Materials Processing Technology*.

———. 2009. "Experimental and Computational Investigation of the Roll Forming Process." Luleå University of Technology.

Lindgren, M., and L. Ingmarsson. 2009. "3D Roll-Forming of Hat-Profile with Variable Depth and Width." *Rollform09 1st International Congress on Roll Forming*.

Lohe, D., H. Lang, and O. Vohringer. 2002. *Handbook of Residual Stress and Deformation of Steel*. Edited by G. Totten, M. Howes, and T. Inoue. *Handbook of Residual Stress and Deformation of Steel*.

Manson, S. S. 1954. "Behaviour of Materials under Conditions of Thermal Stress." *NACA TN-2933. USA: National Advisory Committee for Aeronautics*.

Metinvest ® Technical brochures. n.d. "S320GD and S350GD High-Strength Galvanized Coils."

Moen, C. D., T. Igusa, and B. W. Schafer. 2008. "Prediction of Residual Stresses and Strains in Cold-Formed Steel Members." *Thin-Walled Structures* 46 (11): 1274–89.

Morrow, J.D. 1965. "Cyclic Plastic Strain Energy and Fatigue of Metals." *International Friction, Damping and Cyclic Plasticity, ASTM, STP* 378: 45–87.

MSC Software Corporation. 2013a. "Marc® 2013.1 User ' s Guide." In .

———. 2013b. *Marc® 2013 Volume A : Theory and User Information*. MSC Software Corporation.

Muller, M., S.M. Barrans, and L. Blunt. 2011. "Predicting Plastic Deformation and Work Hardening during V-Band Formation." *Journal of Materials Processing Technology* 211 (4): 627–36.

Natal Jorge, R. M., and L. M. J. S. Dinis. 2004. "Teoria Da Plasticidade."

Oñate, E. 2009. *Structural Analysis with the Finite Element Method. Linear Statics: Volume 1: Basis and Solids*. First Edit. Springer.

Panton, S. M., J. L. Duncan, and S. D. N. Zhu. 1996. "Longitudinal and Shear Strain Development in Cold Roll Forming." *Journal of Materials Processing Technology* 60: 219–24.

Saffe, S. N. M., N. Takuo, and O. Hiroshi. 2014. "Effect of Initial Thickness to Cut End Deformation of Hat Shape Channel Steel by Roll Forming." *Key Engineering Materials* 622–623: 1132–38.

Schafer, B. W., and T. Peköz. 1998. "Computational Modeling of Cold-Formed Steel: Characterizing Geometric Imperfections and Residual Stresses." *Journal of Constructional Steel Research* 47 (3): 193–210.

Senanayake, R.S., I.M. Cole, and S. Thiruvarudchelvan. 1994. "The Application of Computational and Experimental Techniques to Metal Deformation in Cold Roll Forming." *Journal of Materials Processing Technology* 45 (1–4): 155–60.

Stephens, R., A. Fatemi, R. R. Stephens, and H. Fuchs. 2001. *Metal Fatigue in Engineering*. Second. Jonh Wiley & Sons, inc.

Tehrani, M. S., P. Hartley, H. M. Naeini, and H. Khademizadeh. 2006. "Localised Edge Buckling in Cold Roll-Forming of Symmetric Channel Section." *Thin-Walled Structures* 44 (2): 184–96.

Wehner, T., and A Fatemi. 1991. "Effects of Mean Stress on Fatigue Behaviour of a Hardened Carbon Steel." *International Journal of Fatigue* 3: 241–48.

Yan, J. 1998. "Study of Bauschinger Effect in Various Spring Steels." University of Toronto.

Zhuang, W. Z., and G. R. Halford. 2001a. "Investigation of Residual Stress Relaxation under Cyclic Load." *International Journal of Fatigue* 23, Supple: 31–37.

———. 2001b. "Investigation of Residual Stress Relaxation under Cyclic Load." *International Journal of Fatigue,* 31–37.

Appendix 1

Rolls design

Roll design for simulation 1 of the U-channel profile

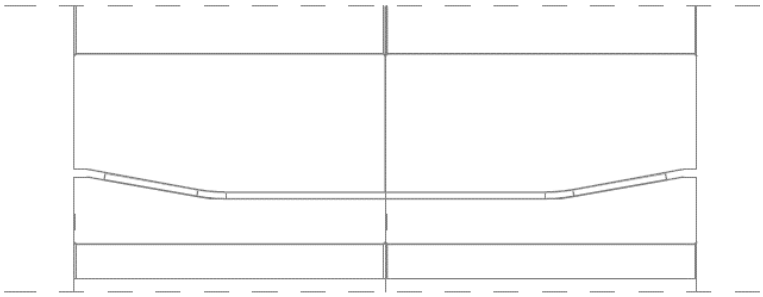

Figure 1.1 – Rolls of forming station 1 of simulation 1.

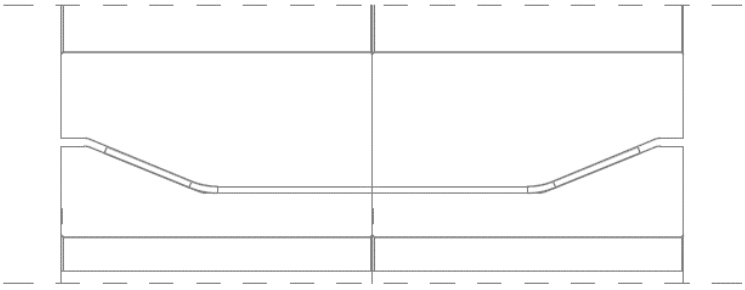

Figure 1.2 – Rolls of forming station 2 of simulation 1.

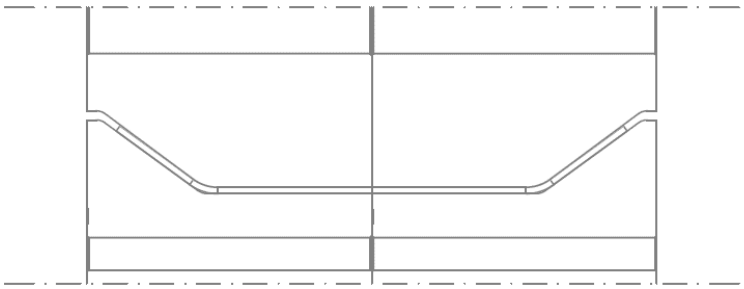

Figure 1.3 – Rolls of forming station 3 of simulation 1.

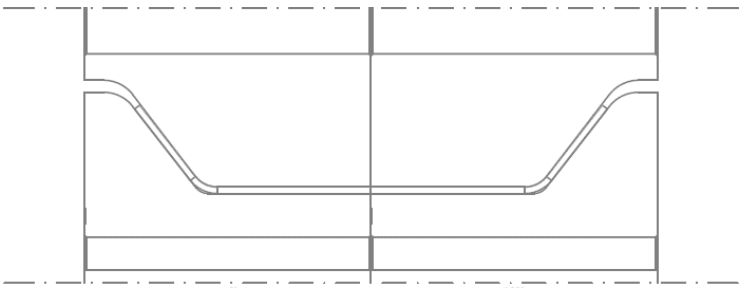

Figure 1.4 – Rolls of forming station 4 of simulation 1.

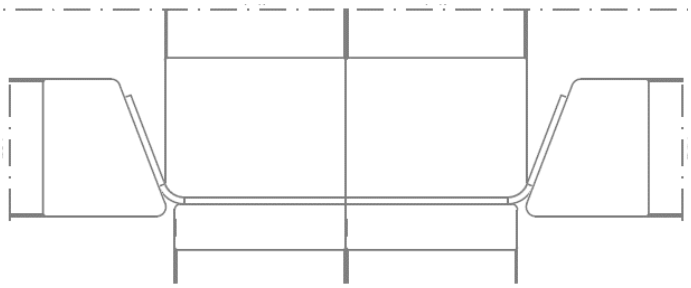

Figure 1.5 – Rolls of forming station 5 of simulation 1.

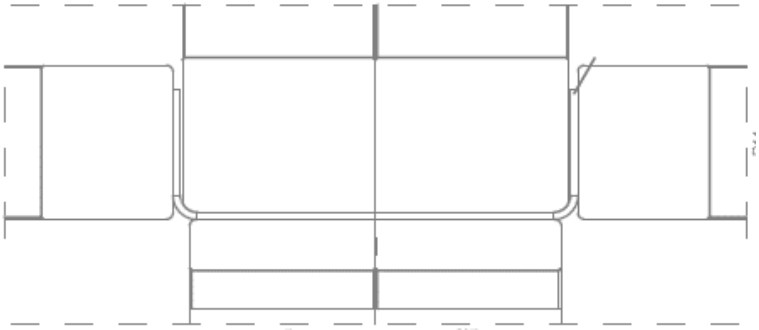

Figure 1.6 – Rolls of forming station 6 of simulation 1.

Note that rolls used in simulation 1 are the same used for all the simulations that compose the parametric study, except for simulation 3.

Roll design for simulation 3 of the U-channel profile

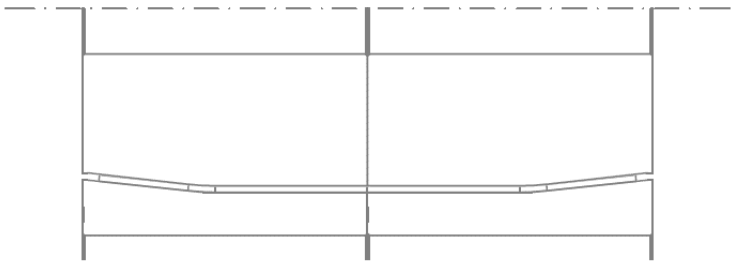

Figure 1.7 – Rolls of forming station 1 of simulation 3.

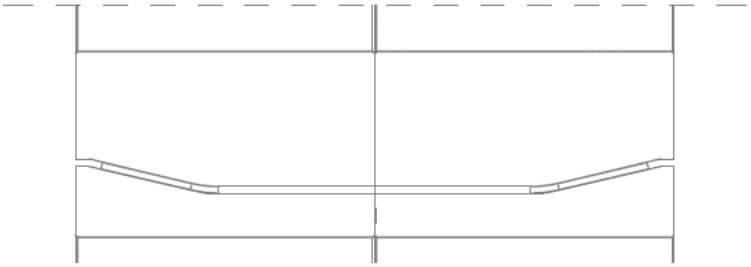

Figure 1.8 – Rolls of forming station 2 of simulation 3.

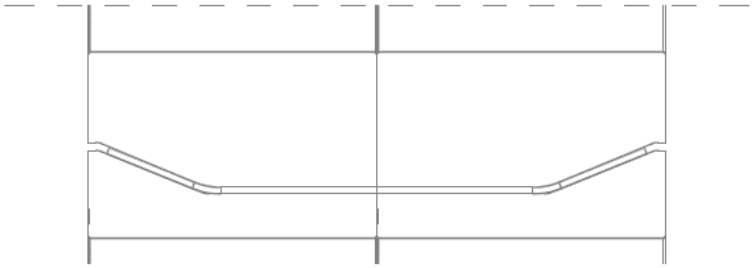

Figure 1.9 – Rolls of forming station 3 of simulation 3.

Figure 1.10 – Rolls of forming station 4 of simulation 3.

Figure 1.11 – Rolls of forming station 5 of simulation 3.

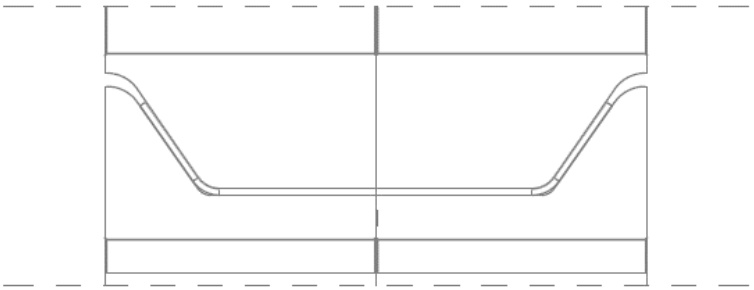

Figure 1.12 – Rolls of forming station 6 of simulation 3.

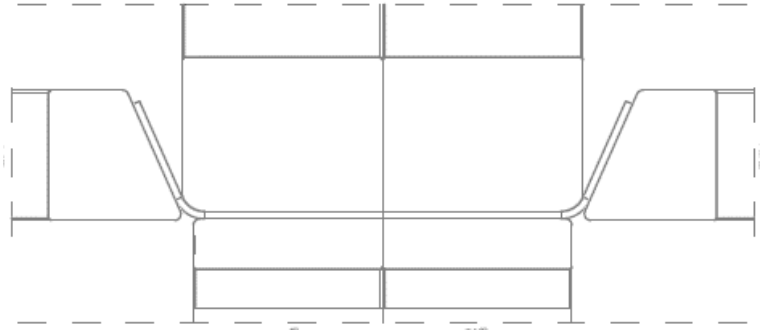

Figure 1.13 – Rolls of forming station 7 of simulation 3.

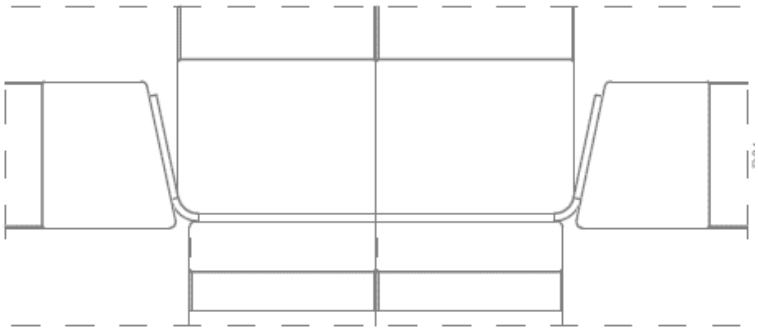

Figure 1.14 – Rolls of forming station 8 of simulation 3.

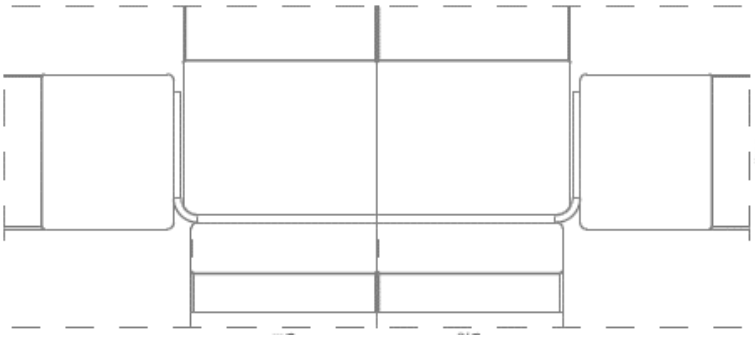

Figure 1.15 – Rolls of forming station 9 of simulation 3.

Roll design for the simulation of the Z-section profile

Figure 1.16 – Rolls of forming station 1 of the Z-section profile model.

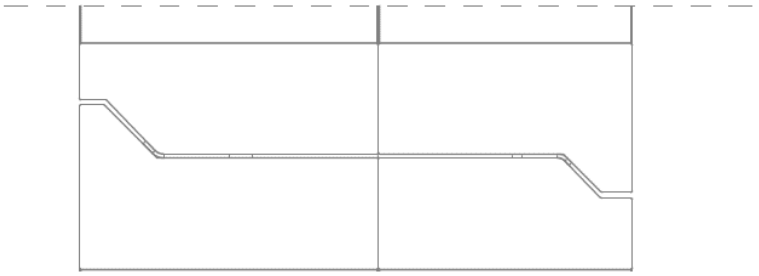

Figure 1.17 – Rolls of forming station 2 of the Z-section profile model.

Figure 1.18 – Rolls of forming station 3 of the Z-section profile model.

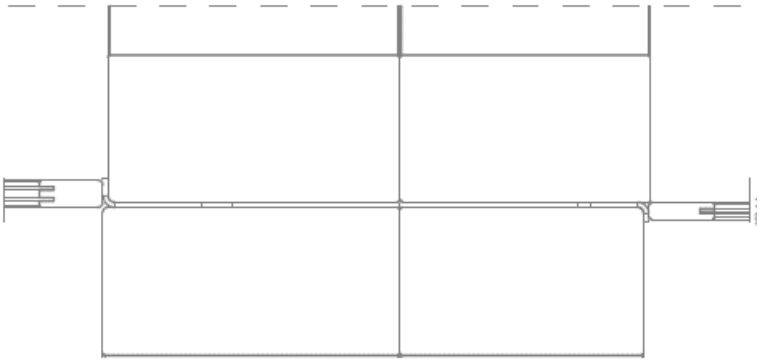

Figure 1.19 – Rolls of forming station 4 of the Z-section profile model.

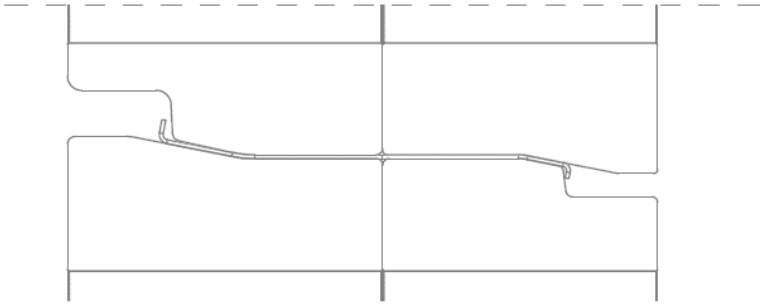

Figure 1.20 – Rolls of forming station 5 of the Z-section profile model.

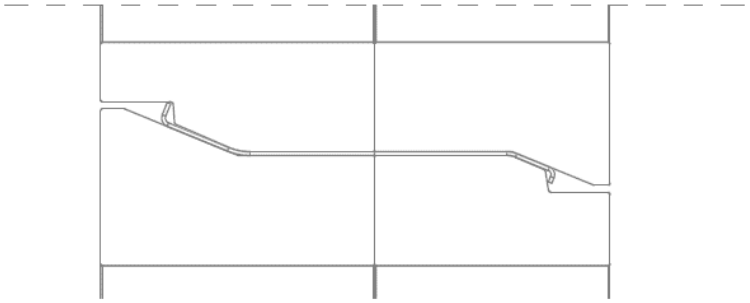

Figure 1.21 – Rolls of forming station 6 of the Z-section profile model.

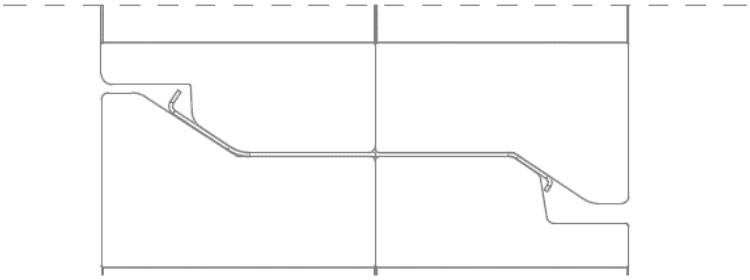

Figure 1.22 – Rolls of forming station 7 of the Z-section profile model.

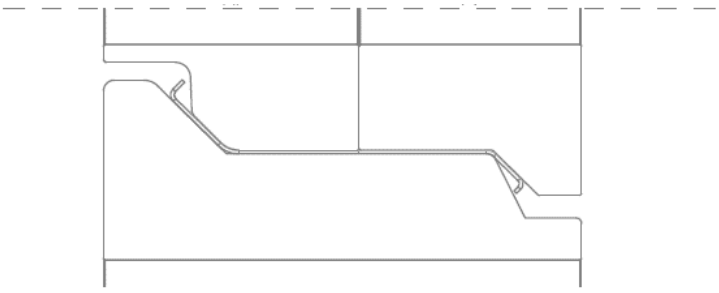

Figure 1.23 – Rolls of forming station 8 of the Z-section profile model.

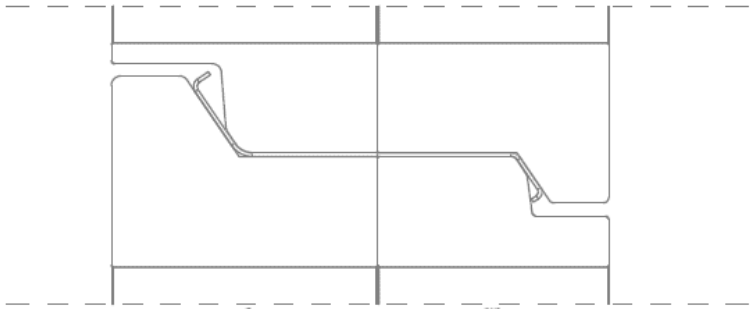

Figure 1.24 – Rolls of forming station 9 of the Z-section profile model.

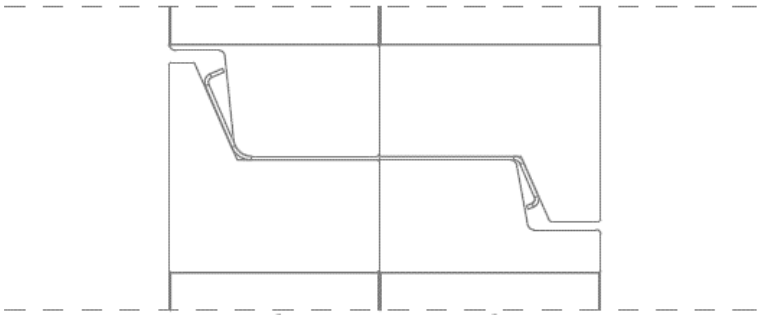

Figure 1.25 – Rolls of forming station 10 of the Z-section profile model.

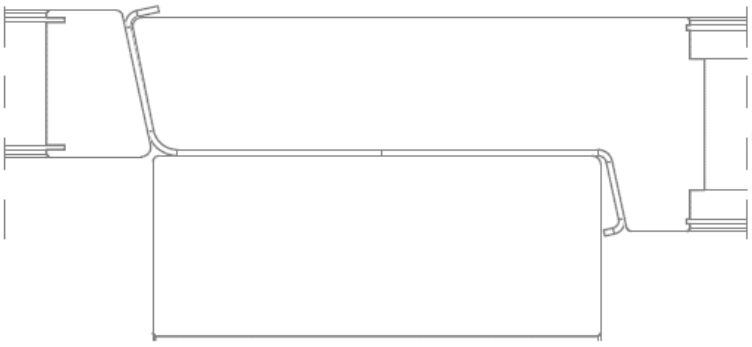

Figure 1.26 – Rolls of forming station 11 of the Z-section profile model.

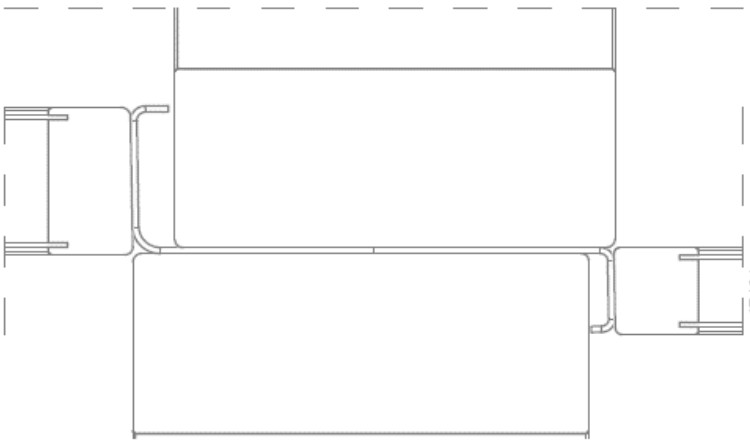

Figure 1.27 – Rolls of forming station 12 of the Z-section profile model.

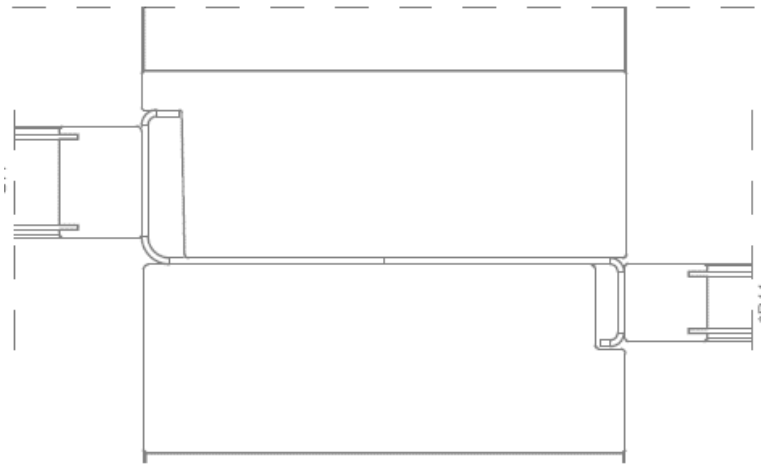

Figure 1.28 – Rolls of forming station 13 of the Z-section profile model.

Appendix 2

Mechanical properties of S460 steel

Table 2.1 – Mechanical properties of S460 steel (B2B Metal 2014).

Name	**Yield Strength $R_{p\ 0.2}$ [MPa]**	**Ultimate Tensile Strength R_m [MPa]**	**Elongation at Ultimate Tensile Strength A_{80} [%]**
S460	460	540	17

Appendix 3

Through thickness residual stresses – Simulations 1 vs 3 (U-channel)

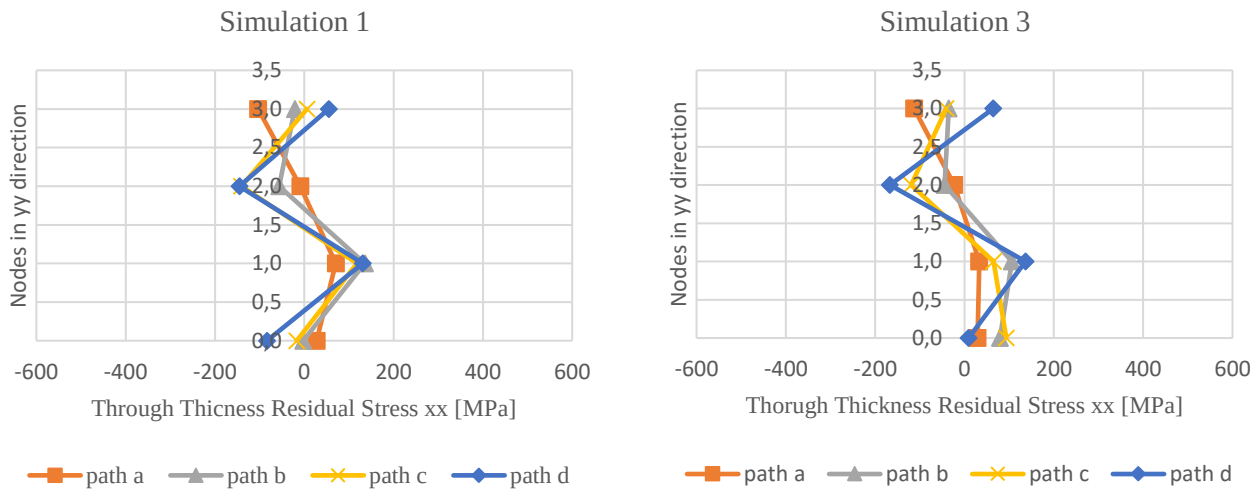

Figure 3.1 – Comparison of through thickness residual stresses [MPa] along the xx direction between simulations 1 and 3 for plane ii.

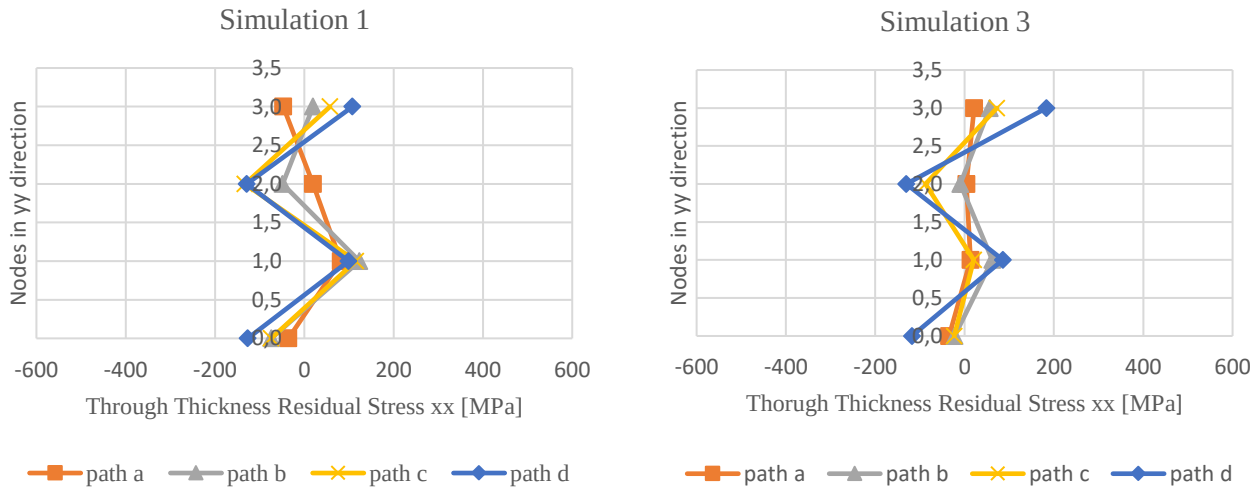

Figure 3.2 – Comparison of through thickness residual stresses [MPa] along the xx direction between simulations 1 and 3 for plane iii.

Appendix 4

Transverse Residual Stresses – Simulations 1 vs 5, 6 (U-channel)

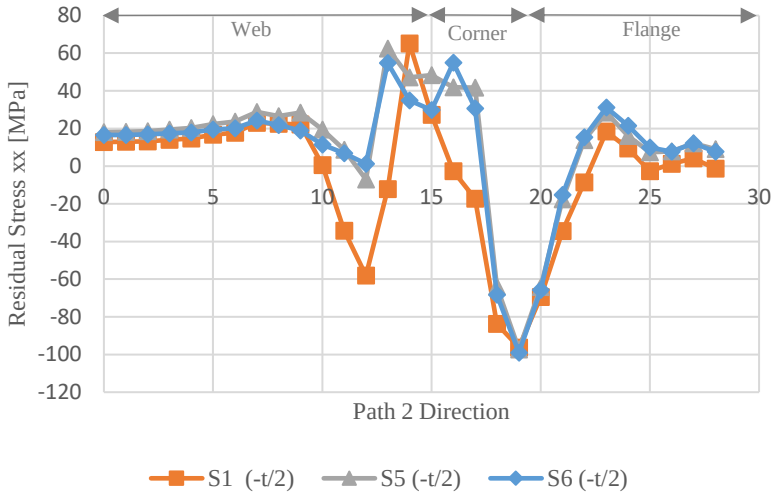

Figure 4.1 – Comparison of transverse residual stresses [MPa] along the xx direction between simulations 1, 5 and 6 in path 2 for the bottom surface.

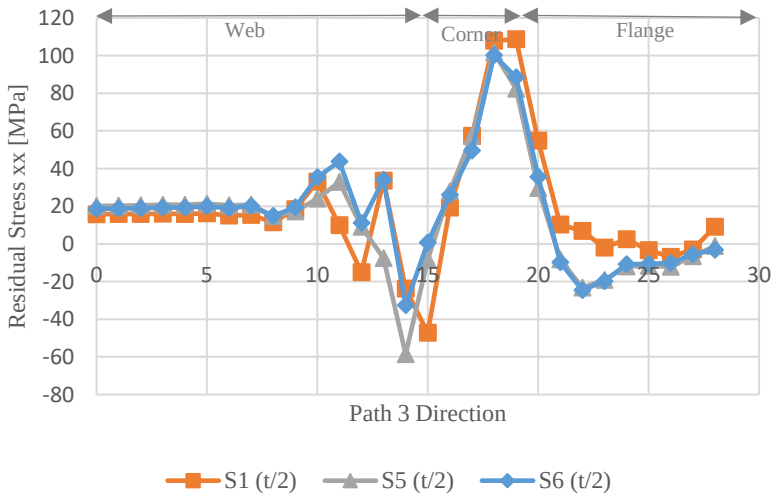

Figure 4.2 – Comparison of transverse residual stresses [MPa] along the xx direction between simulations 1, 5 and 6 in path 3 for the top surface.

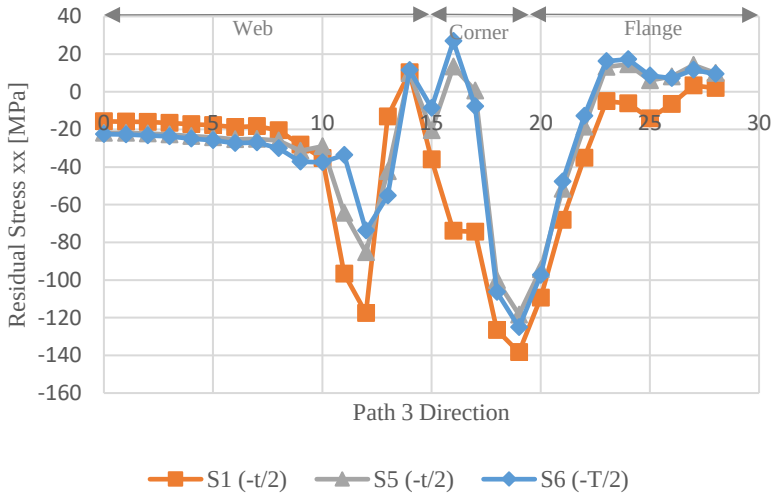

Figure 4.3 – Comparison of transverse residual stresses [MPa] along the xx direction between simulations 1, 5 and 6 in path 3 for the bottom surface.

Appendix 5

Through thickness residual stresses – Simulations 1 vs 7, 8 (U-channel)

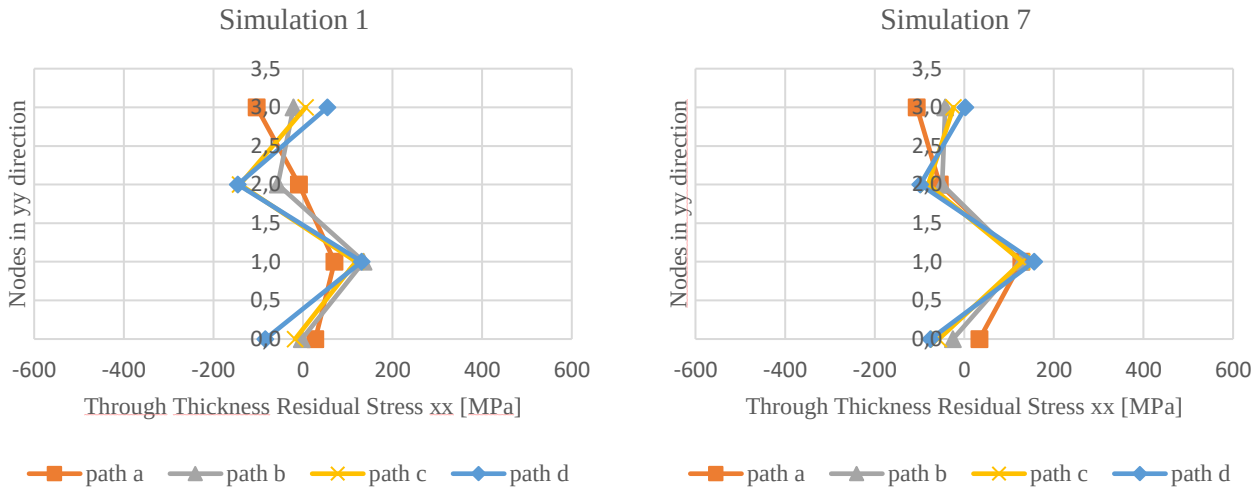

Figure 5.1 – Comparison of through thickness residual stresses [MPa] along the xx direction between simulations 1 and 7 for plane ii.

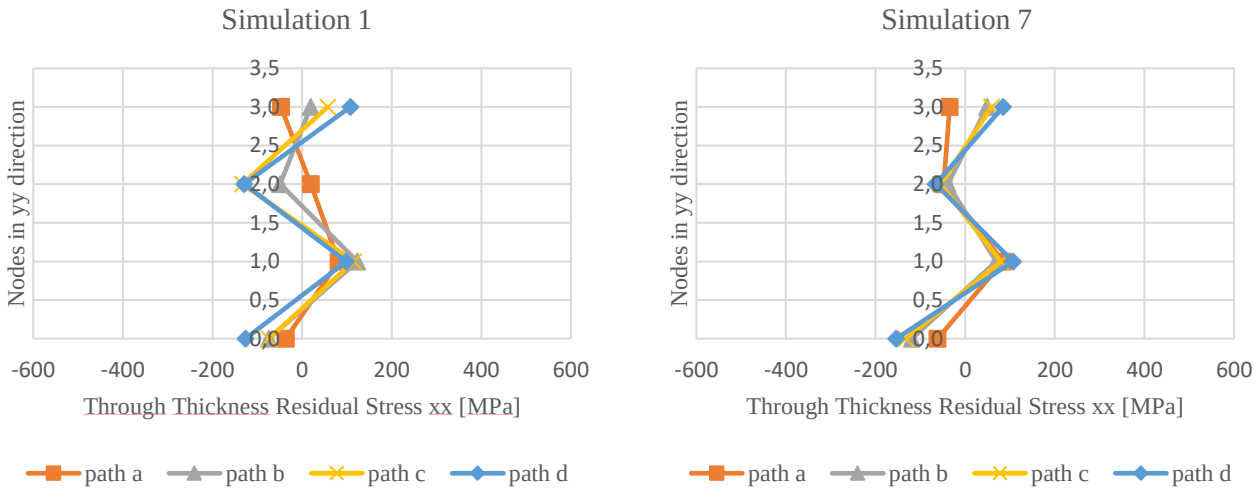

Figure 5.2 – Comparison of through thickness residual stresses [MPa] along the xx direction between simulations 1 and 7 for plane iii.

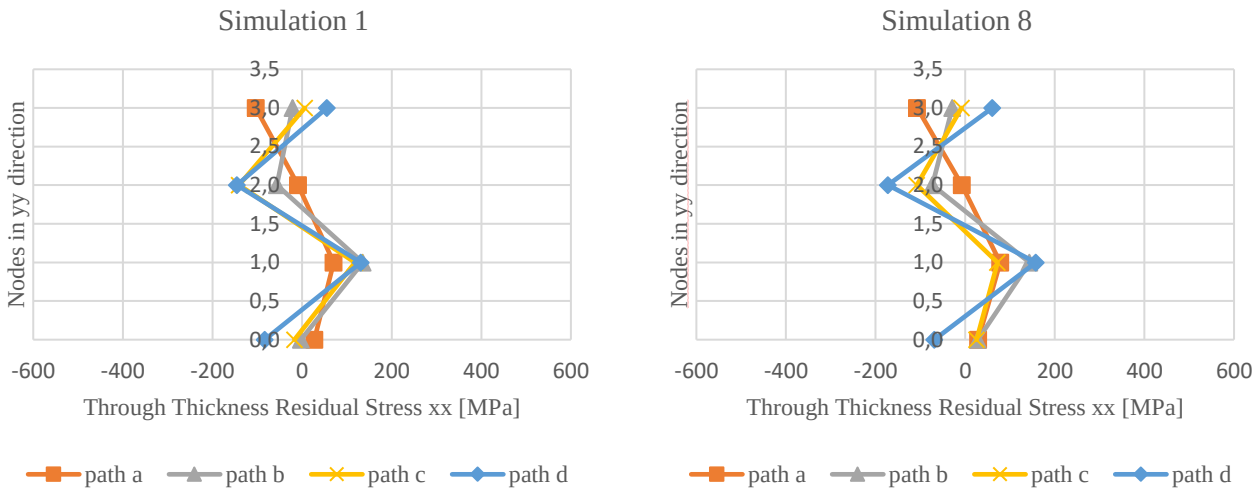

Figure 5.3 – Comparison of through thickness residual stresses [MPa] along the xx direction between simulations 1 and 8 for plane ii.

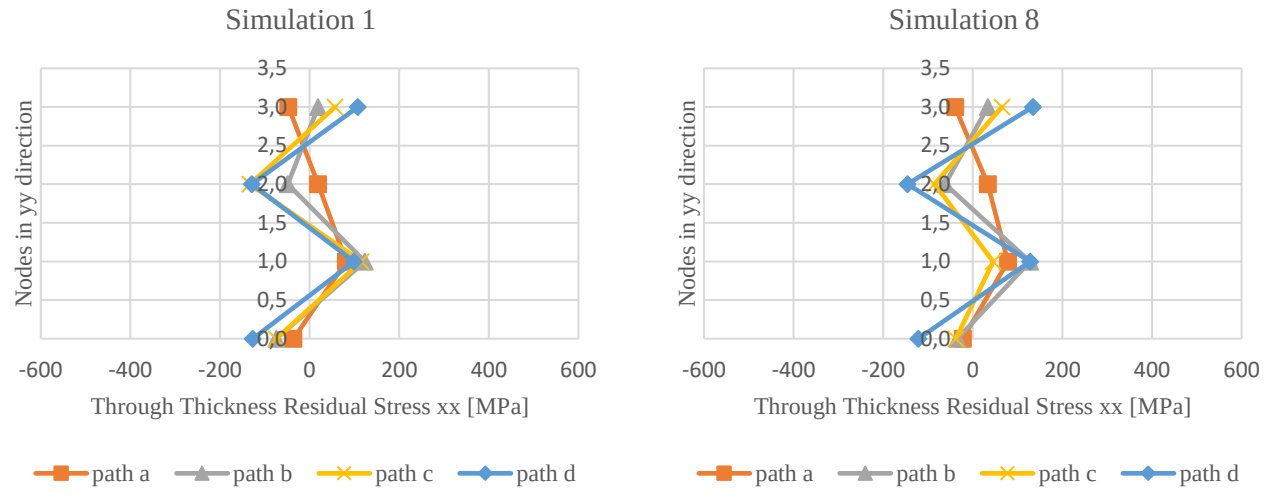

Figure 5.4 – Comparison of through thickness residual stresses [MPa] along the xx direction between simulations 1 and 8 for plane iii.

Appendix 6

Residual stresses – Simulations 1 vs 9 (U-channel)

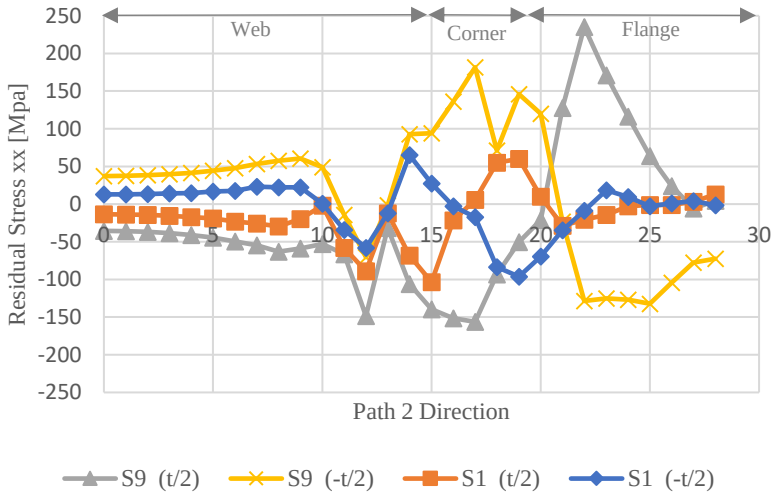

Figure 6.1 – Comparison of transverse residual stresses [MPa] along the xx direction between simulations 1 and 9 in path 2.

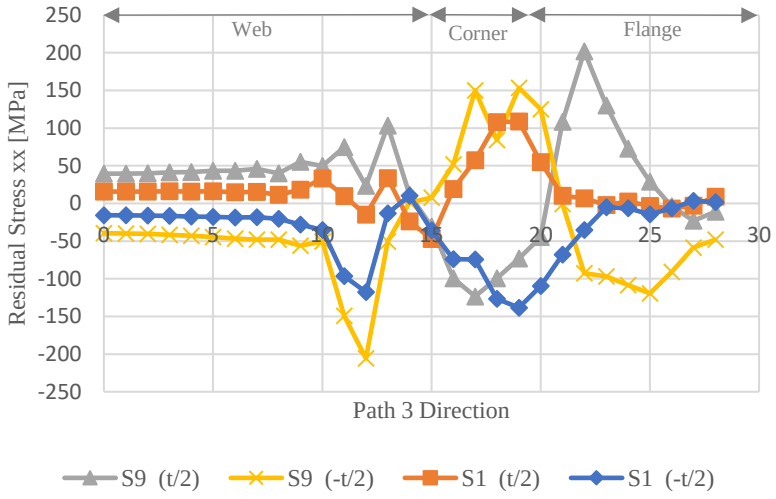

Figure 6.2 – Comparison of transverse residual stresses [MPa] along the xx direction between simulations 1 and 9 in path 3.

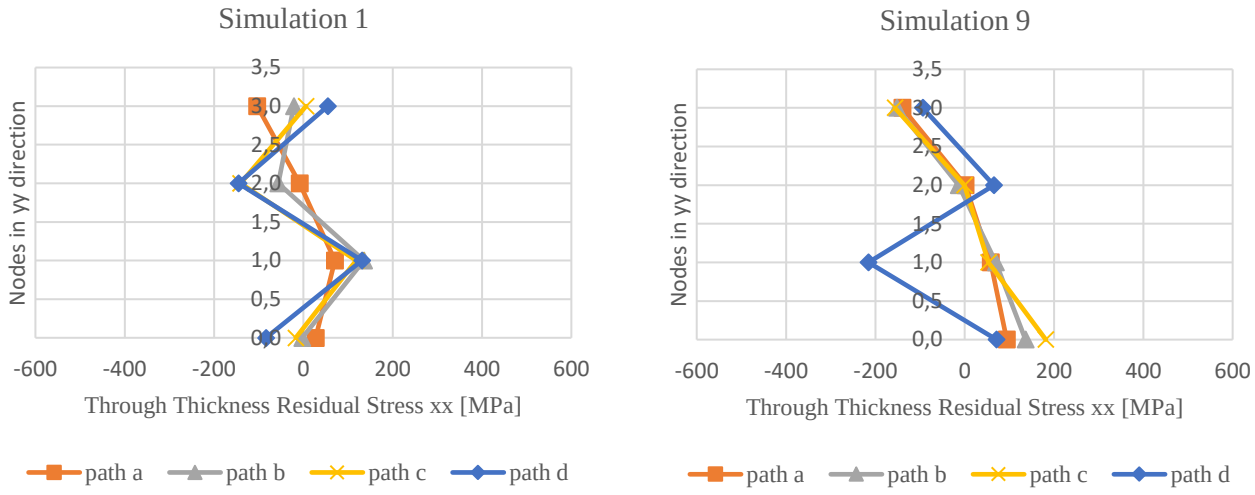

Figure 6.3 – Comparison of through thickness residual stresses [MPa] along the xx direction between simulations 1 and 9 for plane ii.

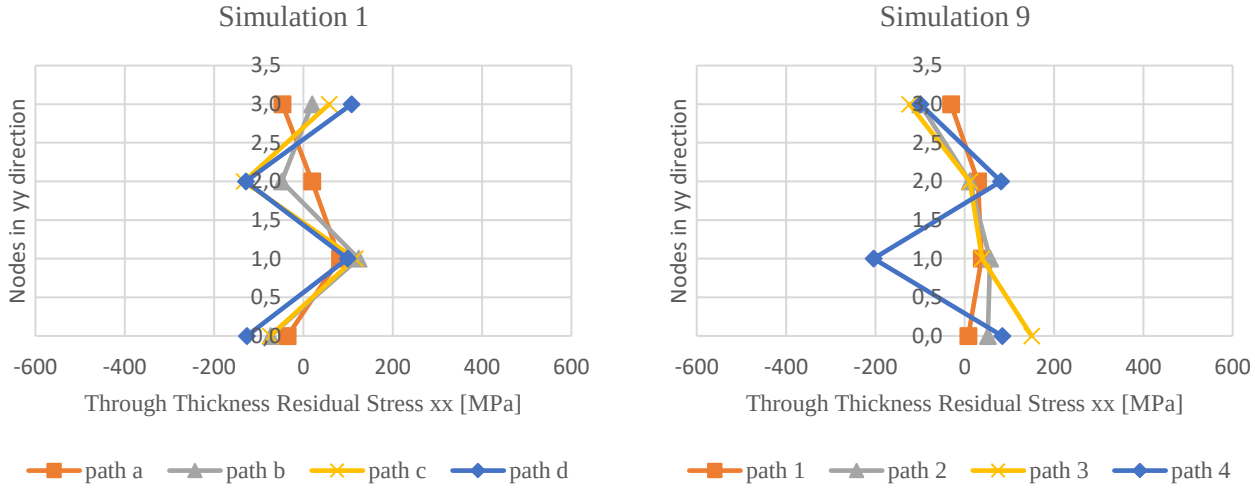

Figure 6.4 – Comparison of through thickness residual stresses [MPa] along the xx direction between simulations 1 and 9 for plane iii.

Appendix 7

Stresses along the xx direction for the inner and outer corner of the profile after cyclic loads – U-channel

Table 7.1 – Stresses [MPa] along the xx direction of the element coordinate system [MPa] for the inner corner of the profile. Comparison between the initial state and results (in step 26 and 76) after application of 2 kN, 4,5 kN and 9 kN.

		Inner corner_Step26			**Inner corner_Step76**		
Load	**Initial state**	**2 kN**	**4,5 kN**	**9 kN**	**2kN**	**4,5 kN**	**9 kN**
	-24,13	136,88	402,48	555,09	136,88	402,22	554,72
	-63,15	113,11	409,80	558,35	113,11	409,53	557,98
path x	-48,86	135,32	418,01	560,44	135,32	417,72	560,05
	-44,25	138,40	417,23	561,13	138,40	416,95	560,75
	-48,16	123,24	406,42	558,88	123,24	406,18	558,50
	12,81	54,05	265,99	469,24	54,05	265,90	469,03
	29,37	72,25	282,74	475,27	72,25	282,61	475,06
path y	39,11	78,07	287,14	476,68	78,07	287,01	476,46
	26,77	57,45	275,35	471,68	57,45	275,25	471,45
	12,12	37,09	260,31	462,07	37,09	260,23	461,86
	36,16	-55,39	77,21	298,33	-55,37	77,29	298,38
	39,98	-58,44	82,57	307,78	-58,42	82,66	307,83
path z	54,56	-59,10	82,29	312,95	-59,08	82,38	312,97
	50,38	-50,92	78,95	310,73	-50,91	79,04	310,76
	42,39	-56,91	65,70	299,54	-56,90	65,80	299,57
	80,21	-58,26	-30,56	129,91	-58,26	-30,43	130,14
	83,82	-60,90	-32,96	141,56	-60,89	-32,81	141,80
path w	90,15	-59,99	-38,60	149,78	-59,98	-38,45	150,00
	91,42	-58,50	-49,01	151,66	-58,49	-48,85	151,86
	86,86	-57,56	-57,03	145,58	-57,55	-56,99	145,77

Table 7.2 – Stresses [MPa] along the xx direction of the element coordinate system [MPa] for the inner corner of the profile. Comparison between the initial state and results (in step 51 and 100) after application of 2 kN, 4,5 kN and 9 kN.

		Inner corner_Step51			**Inner corner_Step100**		
Load	**Initial state**	**2 kN**	**4,5 kN**	**9 kN**	**2kN**	**4,5 kN**	**9kN**
	-24,13	-48,75	-31,65	-317,38	-68,37	-33,49	-320,85
	-63,15	-75,60	-34,02	-341,24	-97,50	-35,91	-344,81
path x	-48,86	-54,69	-29,05	-350,86	-77,19	-30,97	-354,48
	-44,25	-50,26	-26,42	-342,59	-71,59	-28,32	-346,19
	-48,16	-61,01	-27,61	-319,52	-79,58	-29,44	-323,02
	12,81	-72,69	-37,20	-187,66	-90,89	-38,33	-190,05
	29,37	-58,12	-28,51	-205,77	-77,66	-29,70	-208,26
path y	39,11	-53,81	-27,78	-214,71	-72,56	-28,98	-217,24
	26,77	-73,27	-38,14	-213,45	-90,04	-39,31	-215,96
	12,12	-89,79	-45,92	-199,98	-104,11	-47,05	-202,39
	36,16	-100,01	-38,12	-5,47	-111,03	-38,35	-6,33
	39,98	-104,54	-36,67	-11,27	-116,24	-36,90	-12,19
path z	54,56	-105,94	-39,25	-12,35	-116,56	-39,48	-13,31
	50,38	-97,23	-42,78	-9,23	-104,89	-43,01	-10,18
	42,39	-101,30	-53,73	-4,57	-105,98	-53,96	-5,46
	80,21	-44,55	-7,77	109,91	-42,66	-7,47	110,13
	83,82	-46,94	-10,34	116,13	-44,49	-10,02	116,34
path w	90,15	-46,23	-17,02	121,84	-43,96	-16,69	122,03
	91,42	-44,69	-28,47	126,55	-42,77	-28,14	126,73
	86,86	-43,79	-37,54	126,54	-41,32	-37,34	126,72

Table 7.3 – Stresses [MPa] along the xx direction of the element coordinate system [MPa] for the outer corner of the profile. Comparison between the initial state and results (in step 26 and 76) after application of 2 kN, 4,5 kN and 9 kN.

		Outer corner_Step26			**Outer corner_Step76**		
Load	**Initial state**	**2 kN**	**4,5 kN**	**9 kN**	**2 kN**	**4,5 kN**	**9 kN**
	-12,14	-151,67	-377,52	-540,61	-151,67	-377,55	-540,12
	-2,09	-145,25	-380,58	-540,10	-145,25	-380,61	-539,61
path x	-10,77	-156,13	-393,94	-540,97	-156,13	-393,95	-540,48
	-28,46	-171,19	-406,61	-542,07	-171,19	-406,61	-541,58
	-26,72	-164,54	-402,38	-543,01	-164,54	-402,40	-542,52
	-45,54	-81,99	-259,09	-438,92	-81,99	-259,15	-438,58
	-33,10	-76,81	-260,36	-441,82	-76,81	-260,41	-441,47
path y	-35,04	-79,14	-265,34	-443,61	-79,14	-265,39	-443,25
	-50,52	-86,68	-272,87	-445,64	-86,68	-272,93	-445,27
	-54,95	-86,30	-268,97	-445,75	-86,30	-269,04	-445,38
	-41,26	53,90	-45,53	-233,02	53,89	-45,61	-232,90
	-38,39	56,19	-45,89	-237,99	56,18	-45,97	-237,84
path z	-47,32	54,12	-47,90	-241,77	54,11	-47,98	-241,59
	-47,23	54,65	-43,62	-241,83	54,65	-43,69	-241,65
	-45,67	58,54	-32,33	-238,17	58,54	-32,39	-237,99
	-107,37	64,55	57,73	-60,95	64,54	57,68	-60,94
	-110,07	65,55	59,25	-63,34	65,54	59,20	-63,31
path w	-113,41	65,26	60,18	-65,14	65,25	60,13	-65,10
	-112,36	63,55	62,47	-63,96	63,55	62,43	-63,92
	-110,84	64,68	67,25	-60,03	64,68	67,23	-60,01

Table 7.4 – Stresses [MPa] along the xx direction of the element coordinate system [MPa] for the outer corner of the profile. Comparison between the initial state and results (in step 51 and 100) after application of 2 kN, 4,5 kN and 9 kN.

		Outer corner_Step51			**Outer corner_Step100**		
Load	**Initial state**	**2 kN**	**4,5 kN**	**9 kN**	**2 kN**	**4,5 kN**	**9 kN**
	-12,14	-3,44	-32,97	156,48	-2,90	-31,72	159,37
	-2,09	6,25	-28,11	175,97	6,81	-26,83	178,92
path x	-10,77	-3,44	-38,60	182,36	-2,88	-37,29	185,34
	-28,46	-19,42	-53,77	175,94	-18,86	-52,46	178,90
	-26,72	-16,18	-57,34	157,35	-15,63	-56,08	160,25
	-45,54	15,59	-24,68	67,28	15,94	-23,92	69,18
	-33,10	22,81	-20,25	80,01	23,17	-19,46	81,96
path y	-35,04	21,37	-23,04	84,42	21,73	-22,25	86,40
	-50,52	13,45	-31,85	78,18	13,81	-31,07	80,16
	-54,95	11,48	-32,95	63,81	11,83	-32,19	65,75
	-41,26	87,74	43,74	1,14	87,84	43,92	1,76
	-38,39	90,82	46,16	5,28	90,92	46,35	5,95
path z	-47,32	89,28	45,69	5,46	89,39	45,88	6,16
	-47,23	89,46	49,88	3,41	89,57	50,08	4,12
	-45,67	92,49	59,96	-0,84	92,60	60,16	-0,14
	-107,37	51,57	34,94	-54,71	51,51	34,75	-54,99
	-110,07	52,33	36,29	-54,64	52,27	36,09	-54,92
path w	-113,41	51,99	37,34	-55,38	51,93	37,15	-55,65
	-112,36	50,43	40,15	-54,81	50,37	39,98	-55,08
	-110,84	52,05	46,17	-52,73	51,99	46,01	-53,02

Table 7.5 – Stresses [MPa] along the xx direction of the element coordinate system [MPa] for the inner corner of the profile. Comparison between the first and second methods (in step 26) after application 9 kN.

Inner corner_Step26					
Load	**Initial state**	**First method**	**Second method**	**Sum**	**Relative error (%)**
	-24,13	555,09	464,65	440,52	-20,64
	-63,15	558,35	466,03	402,87	-27,85
path x	-48,86	560,44	466,58	417,72	-25,47
	-44,25	561,13	466,46	422,21	-24,76
	-48,16	558,88	465,13	416,97	-25,39
	12,81	469,24	395,33	408,15	-13,02
	29,37	475,27	399,10	428,47	-9,85
path y	39,11	476,68	400,45	439,56	-7,79
	26,77	471,68	399,22	425,99	-9,69
	12,12	462,07	394,94	407,06	-11,90
	36,16	298,33	251,63	287,79	-3,53
	39,98	307,78	253,36	293,34	-4,69
path z	54,56	312,95	253,17	307,73	-1,67
	50,38	310,73	253,56	303,93	-2,19
	42,39	299,54	251,40	293,79	-1,92
	80,21	129,91	115,88	196,09	50,94
	83,82	141,56	119,88	203,71	43,90
path w	90,15	149,78	121,49	211,64	41,30
	91,42	151,66	120,36	211,78	39,65
	86,86	145,58	115,91	202,78	39,29

Appendix 8

Stress-strain curves of S350GD steel

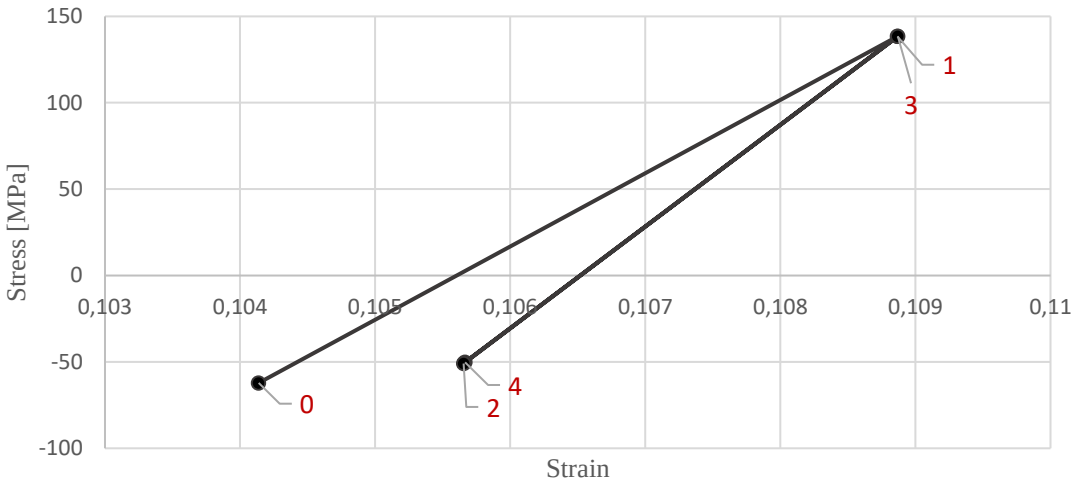

Figure 8.1 – Stress vs strain diagram that describes the elastic behaviour of the material (S350GD) in the second cycle of the external cyclic load of 2 kN. Point 0 represents the initial state of the profile (step 0), point 1 represents the stress-strain state in step 26, point 2 refers to step 51, point 3 to step 76 and point 4 to step 100.

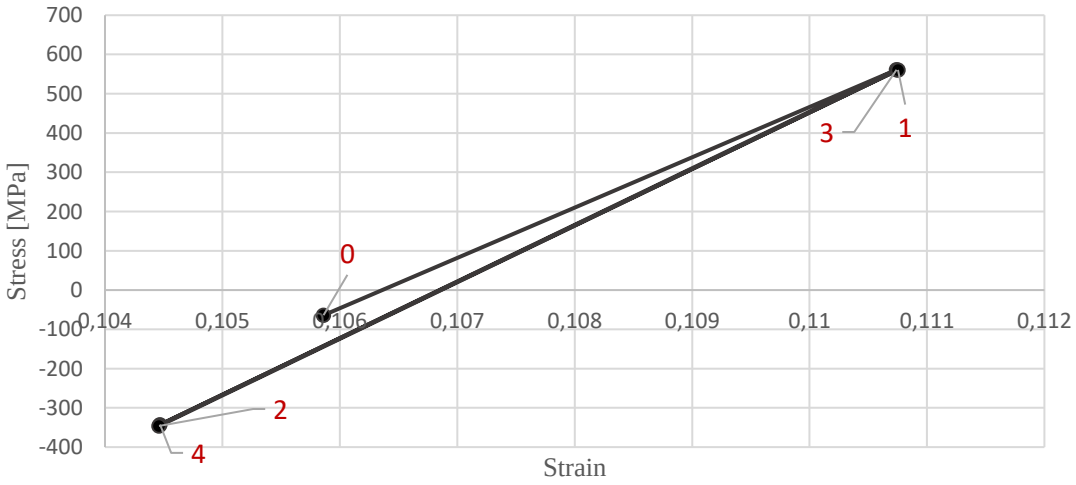

Figure 8.2 – Stress vs strain diagram that describes the elastic behaviour of the material (S350GD) in the second cycle of the external cyclic load of 9 kN. Point 0 represents the initial state of the profile (step 0), point 1 represents the stress-strain state in step 26, point 2 refers to step 51, point 3 to step 76 and point 4 to step 100.

Stress-strain curves presented in Figures 1-2 do not illustrate the material behaviour between the initial state (point 0) and the stress-state at the maximum load amplitude – step 26 (point 1). For this reason, between these two points, four stress-strain values were extracted from the results obtained after the simulation, in order to analyse the behaviour of the material until the application of maximum load amplitude, Figures 3-4.

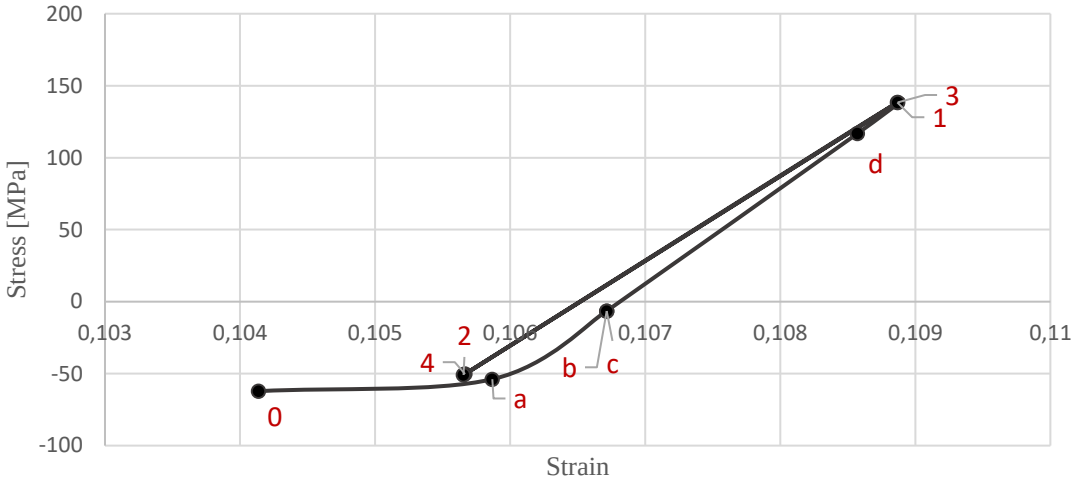

Figure 8.3 – Stress vs strain diagram that describes the elastic behaviour of the material (S350GD) for an external cyclic load of 2 kN. Point 0 represents the initial state of the profile (step 0), point 1 represents the stress-strain state in step 26, point 2 refers to step 51, point 3 to step 76 and point 4 to step 100. Points a, b, c and d represent the stress-state in steps 5, 10, 15 and 20, respectively.

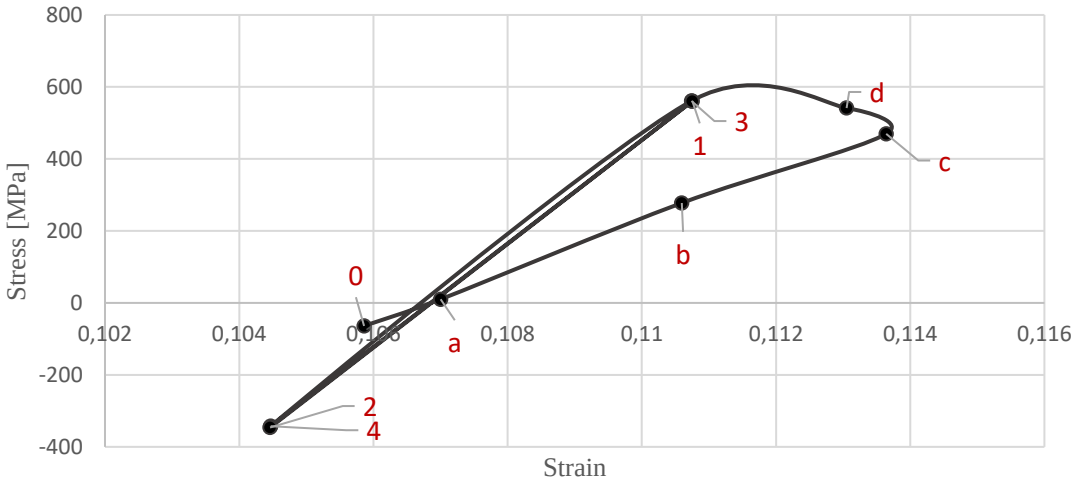

Figure 8.4 – Stress vs strain diagram that describes the elastic behaviour of the material (S350GD) for an external cyclic load of 9 kN. Point 0 represents the initial state of the profile (step 0), point 1 represents the stress-strain state in step 26, point 2 refers to step 51, point 3 to step 76 and point 4 to step 100. Points a, b, c and d represent the stress-state in steps 5, 10, 15 and 20, respectively.

Figures 3-4 reinforce the elastoplastic behaviour of the material in the first cycle of the external load. In the second cycle, maximum and minimum stresses are coincident, respectively, which demonstrates an elastic behaviour of the material in the second cycle of the external load. As a reminder, for fatigue analysis, the trajectory of stresses do not display much influence, although the stress range is of crucial importance to determine fatigue life of a component.

Appendix 9

Bending sequence– Z-section profile

	s = 2.50			1. Entit	2. Entity	3. Entit	4. Entity	5. Entit	6. Entit	7. Entity	8. Entit	9. Entity	10. Enti
OK	Stripwidth			Angle	Angle	Angle	Angle	Angle	Angle	Angle	Angle	Angle	Angle
Profile	290.19			--	90.00	--	90.00	--	--	90.00	--	90.00	--
							@ -1.00			@ -1.00			
12. Formingstation	290.19			--	90.00	--	89.00	--	--	89.00	--	90.00	--
							@ -11.13			@ -11.13			
11. Formingstation	290.19			--	90.00	--	77.88	--	--	77.88	--	90.00	--
							@ -11.13			@ -11.13			
10. Formingstation	290.19			--	90.00	--	66.75	--	--	66.75	--	90.00	--
							@ -11.13			@ -11.13			
9. Formingstation	290.19			--	90.00	--	55.63	--	--	55.63	--	90.00	--
							@ -11.13			@ -11.13			
8. Formingstation	290.19			--	90.00	--	44.50	--	--	44.50	--	90.00	--
							@ -11.13			@ -11.13			
7. Formingstation	290.19			--	90.00	--	33.38	--	--	33.38	--	90.00	--
							@ -11.13			@ -11.13			
6. Formingstation	290.19			--	90.00	--	22.25	--	--	22.25	--	90.00	--
							@ -11.13			@ -11.13			
5. Formingstation	290.19			--	90.00	--	11.13	--	--	11.13	--	90.00	--
							= 0.00			= 0.00			
4. Formingstation	290.19			--	90.00	--	--	--	--	--	--	90.00	--
					@ -22.50							@ -22.50	
3. Formingstation	290.19			--	67.50	--	--	--	--	--	--	67.50	--
					@ -22.50							@ -22.50	
2. Formingstation	290.19			--	45.00	--	--	--	--	--	--	45.00	--
					@ -22.50							@ -22.50	
1. Formingstation	290.19			--	22.50	--	--	--	--	--	--	22.50	--
					= 0.00							= 0.00	
0. Entryguidestation	290.19			--	--	--	--	--	--	--	--	--	--

Figure 9.1 – Bending sequence of the Z-section profile.

Appendix 10

Through thickness residual stresses – Z-section profile

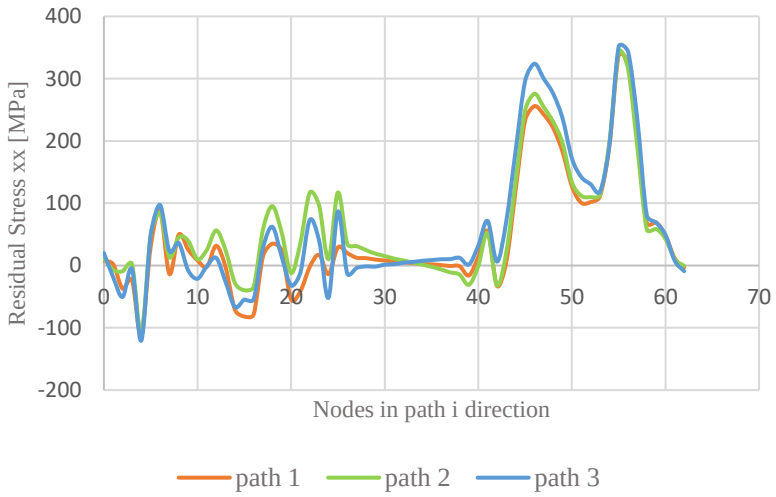

Figure 10.1 – Comparison of transverse residual stresses [MPa] along the xx direction between paths 1, 2 and 3 for the bottom surface of the Z-section profile.

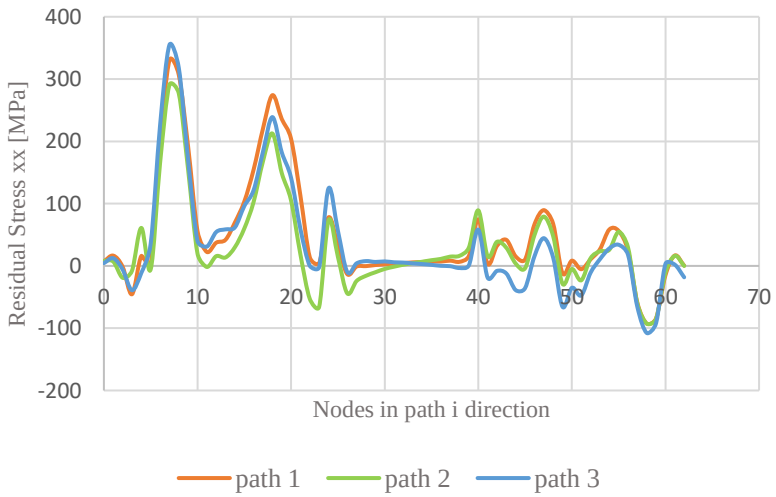

Figure 10.2 – Comparison of transverse residual stresses [MPa] along the xx direction between paths 1, 2 and 3 for the bottom surface of the Z-section profile.

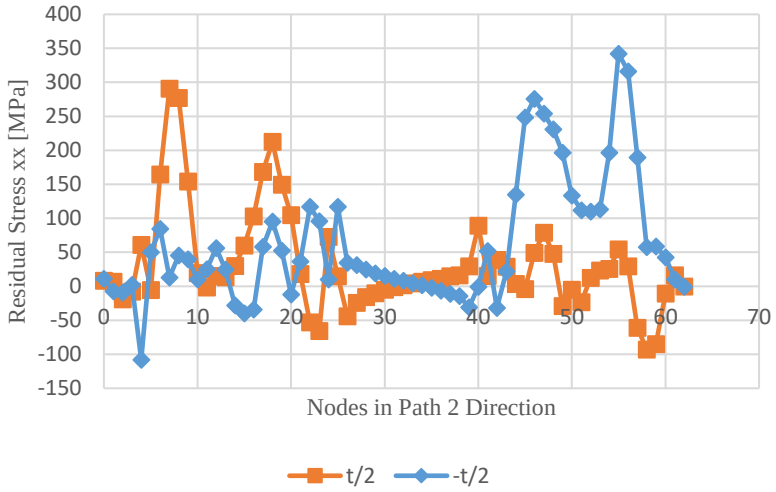

Figure 10.3 – Comparison of transverse residual stresses [MPa] along the xx direction between the top (t/2) and the bottom (-t/2) surface for path 2 of the Z-section profile.

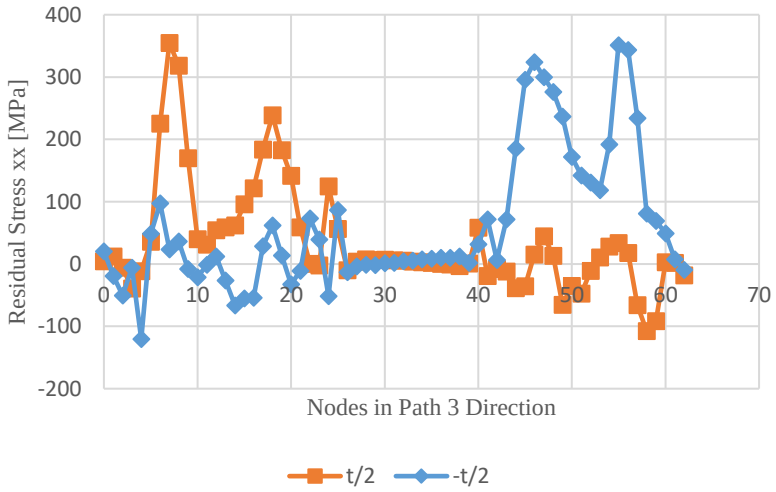

Figure 10.4 – Comparison of transverse residual stresses [MPa] along the xx direction between the top (t/2) and the bottom (-t/2) surface for path 3 of the Z-section profile.

Appendix 11

Stresses along the xx direction for the inner and outer corner of the profile after cyclic loads – Z-section profile

Table 11.1 – Stresses [MPa] along the xx direction of the element coordinate system for the inner corner of the profile with a load applied in the top surface. Comparison between the initial state and results (in step 26 and 76) after application of 2 kN, 4,5 kN and 9 kN.

		Inner corner_Step26			**Inner corner_Step76**		
Load	**Initial state**	**2 kN**	**4,5 kN**	**9 kN**	**2kN**	**4,5 kN**	**9 kN**
	170,95	-139,10	-126,23	54,41	-139,10	-125,61	55,07
	191,35	-140,10	-124,93	54,40	-140,10	-124,29	55,08
path x	203,56	-142,17	-124,27	54,68	-142,17	-123,60	55,36
	201,46	-139,19	-123,36	55,03	-139,19	-122,69	55,70
	206,77	-140,57	-125,19	55,55	-140,57	-124,52	56,21
	211,10	84,72	133,70	292,52	84,69	133,54	292,83
	234,56	83,80	134,78	293,43	83,76	134,63	293,75
path y	252,74	86,12	137,27	294,69	86,08	137,11	295,00
	249,48	88,93	139,27	296,12	88,88	139,11	296,43
	261,28	87,40	139,29	297,78	87,37	139,14	298,07
	166,85	310,71	410,87	536,70	310,69	409,78	536,84
	178,49	317,69	411,93	537,22	317,65	410,82	537,36
path z	197,78	326,65	412,71	537,67	326,61	411,60	537,81
	204,36	329,30	413,60	537,93	329,26	412,49	538,08
	214,82	331,03	413,42	538,35	330,92	412,31	538,49
	129,01	381,41	511,40	631,48	381,39	509,86	631,41
	136,71	386,18	511,89	631,52	386,16	510,34	631,42
path w	154,07	398,32	512,10	631,41	398,30	510,54	631,30
	166,62	405,52	513,06	631,46	405,50	511,52	631,31
	172,33	406,27	513,35	631,39	406,20	511,81	631,16

Table 11.2 – Stresses [MPa] along the xx direction of the element coordinate system for the inner corner of the profile with a load applied in the top surface. Comparison between the initial state and results (in step 51 and 100) after application of 2 kN, 4,5 kN and 9 kN.

		Inner corner_Step51			**Inner corner_Step100**		
Load	**Initial state**	**2 kN**	**4,5 kN**	**9 kN**	**2kN**	**4,5 kN**	**9kN**
	170,95	-128,19	-101,70	103,64	-128,15	-101,41	104,35
	191,35	-129,28	-100,65	103,33	-129,24	-100,34	104,04
path x	203,56	-131,49	-100,33	102,92	-131,45	-100,01	103,62
	201,46	-128,69	-99,83	102,42	-128,65	-99,51	103,12
	206,77	-130,27	-102,14	101,93	-130,23	-101,82	102,61
	211,10	-5,60	-71,82	-89,24	-5,98	-72,67	-89,91
	234,56	-7,48	-72,74	-91,51	-7,87	-73,59	-92,19
path y	252,74	-5,55	-71,03	-91,51	-5,94	-71,89	-92,20
	249,48	-2,65	-68,78	-89,77	-3,05	-69,63	-90,47
	261,28	-3,63	-67,41	-86,14	-4,02	-68,25	-86,85
	166,85	113,89	-36,51	-293,82	113,12	-38,61	-295,75
	178,49	119,55	-38,21	-298,16	118,76	-40,33	-300,11
path z	197,78	128,10	-38,17	-299,02	127,31	-40,29	-300,97
	204,36	131,19	-36,19	-296,87	130,42	-38,31	-298,82
	214,82	134,16	-33,57	-291,59	133,32	-35,67	-293,52
	129,01	143,63	-27,37	-358,19	142,70	-29,93	-360,68
	136,71	147,32	-29,08	-362,50	146,39	-31,66	-365,02
path w	154,07	159,20	-29,45	-363,84	158,26	-32,04	-366,35
	166,62	166,75	-27,63	-362,32	165,82	-30,22	-364,82
	172,33	168,82	-24,44	-357,13	167,85	-27,02	-359,60

Table 11.3 – Stresses [MPa] along the xx direction of the element coordinate system for the outer corner of the profile with a load applied in the bottom surface. Comparison between the initial state and results (in step 26 and 76) after application of 2 kN, 4,5 kN and 9 kN.

		Outer corner_Step26			**Outer corner_Step76**		
Load	**Initial state**	**2 kN**	**4,5 kN**	**9 kN**	**2 kN**	**4,5 kN**	**9 kN**
	56,30	129,93	124,56	93,92	129,93	124,58	90,74
	42,01	130,69	125,36	94,97	130,69	125,39	91,80
path x	37,25	129,70	124,47	94,51	129,70	124,49	91,34
	34,04	130,29	125,11	93,93	130,29	125,13	90,76
	34,88	130,50	125,39	93,97	130,50	125,41	90,81
	86,72	178,11	269,77	258,75	178,10	269,77	257,84
	72,18	173,33	265,49	258,44	173,32	265,49	257,53
path y	64,06	170,94	263,48	258,86	170,93	263,48	257,95
	57,67	170,48	263,66	260,91	170,47	263,67	260,00
	55,14	166,59	260,31	261,87	166,59	260,32	260,97
	74,81	226,57	415,06	473,55	226,55	414,83	474,99
	66,74	225,16	414,75	472,66	225,15	414,52	474,08
path z	58,82	222,26	413,86	472,23	222,24	413,65	473,64
	52,10	219,19	414,97	472,96	219,18	414,70	474,35
	46,23	214,19	412,65	473,85	214,17	412,32	475,23
	-6,99	181,38	435,04	591,77	181,36	434,51	594,60
	-3,00	189,88	442,14	591,50	189,86	441,62	594,33
path w	-9,75	187,11	438,49	590,99	187,09	437,98	593,81
	-20,63	179,14	432,31	590,75	179,13	431,98	593,55
	-21,99	179,90	435,42	591,67	179,88	435,21	594,39

Table 11.4 – Stresses [MPa] along the xx direction of the element coordinate system for the outer corner of the profile with a load applied in the bottom surface. Comparison between the initial state and results (in step 51 and 100) after application of 2 kN, 4,5 kN and 9 kN.

		Outer corner_Step51			**Outer corner_Step100**		
Load	**Initial state**	**2 kN**	**4,5 kN**	**9 kN**	**2 kN**	**4,5 kN**	**9 kN**
	56,30	135,09	136,20	102,34	181,36	136,29	102,34
	42,01	135,80	136,87	103,09	189,86	136,96	103,09
path x	37,25	134,72	135,78	102,31	187,09	135,87	102,31
	34,04	135,19	136,13	101,37	179,13	136,22	101,37
	34,88	135,23	136,02	101,00	179,88	136,11	101,00
	86,72	102,53	96,29	3,19	102,24	95,69	3,80
	72,18	97,08	90,47	1,07	96,79	89,86	1,68
path y	64,06	94,30	87,55	0,58	94,00	86,94	1,20
	57,67	93,81	87,67	2,80	93,51	87,05	3,43
	55,14	90,37	85,35	5,42	90,07	84,73	6,06
	74,81	60,69	36,12	-72,49	60,05	34,63	-71,21
	66,74	58,18	33,22	-76,30	57,53	31,72	-75,02
path z	58,82	54,84	31,33	-77,59	54,19	29,83	-76,31
	52,10	51,98	33,04	-75,77	51,32	31,54	-74,50
	46,23	47,89	33,03	-71,56	47,24	31,54	-70,28
	-6,99	-33,53	-53,57	-114,00	-34,39	-55,45	-112,29
	-3,00	-26,20	-49,18	-116,48	-27,07	-51,09	-114,75
path w	-9,75	-29,36	-53,79	-117,33	-30,23	-55,72	-115,59
	-20,63	-36,83	-59,19	-115,61	-37,70	-61,12	-113,86
	-21,99	-34,92	-53,83	-111,03	-35,78	-55,75	-109,23